

Carrier-envelope Phase (CEP)-dependent Strong-field Ionization at Infrared (IR) Wavelengths

Dissertation

for the acquisition of the academic title
Doktor Rerum Naturalium (Dr. rer. nat.)



submitted to
the Council of the Faculty of Physics and Astronomy
of the Friedrich-Schiller-Universität Jena

by M.Sc. Yinyu Zhang
born on 25.04.1991 in Lanzhou, China

Reviewers:

1. Prof. Dr. rer. nat. habil. Gerhard G. Paulus, Friedrich-Schiller-Universität Jena
2. Prof. Dr. rer. nat. habil. Thomas Fennel, Universität Rostock
3. Dr. rer. nat. habil. Markus Zeiler, Technische Universität Wien

Date of the Disputation: 02.02.2023

Contents

Abstract	i
Kurzfassung	vi
1 Introduction	1
1.1 Motivation	1
1.2 Main Concepts of the Thesis	4
1.2.1 CEP-measurement Towards SWIR and MIR Range	4
1.2.2 Phase-volume Effect in Few-cycle Light-matter Interactions	5
1.2.3 High-order CEP-dependence in the Asymmetry Map of Cs	6
1.3 Structure of the Thesis	7
2 Theoretical Background	9
2.1 Strong-field Ionization (SFI)	10
2.1.1 Multiphoton Ionization (MPI)	10
2.1.2 Tunnelling Ionization (TI)	12
2.2 The Strong-field Phenomena and the Three-step Model	15
2.2.1 Direct Electrons	16
2.2.2 Returning Electrons	17
2.2.3 Rescattered Electrons	18
2.2.4 Strong-field Phenomena Induced by Few-cycle Pulses	20
3 Simulation Methods	24
3.1 Semi-classical Model (Classical Trajectory Monte-Carlo Simulations)	24
3.1.1 Depletion in Ionizations	25
3.1.2 Perpendicular Momentum for Direct Electrons	26

3.2	Time-dependent Schrödinger Equation (TDSE) Model	26
4	Laser Systems and Experimental Setup	30
4.1	Laser Systems	30
4.1.1	IR and SWIR Laser System	30
4.1.2	MIR Laser System	33
4.2	Carrier-envelope Phasemeter (CEPM)	35
5	CEP Measurements at 1.8 μm and Simulation Results	40
5.1	Scaling Strong-field Interactions with Wavelengths	40
5.2	CEP Measurements at 1.8 μm	42
5.3	Simulation Results and Comparison to Experimental Results	48
5.4	Discussions	51
5.4.1	Single-shot Requirement	51
5.4.2	Intensity Impact	53
6	Phase-volume Effect in Few-cycle Light-matter Interactions	55
6.1	The Gaussian Beam and the Gouy Phase	56
6.2	The Pulsed Beam and the Focal Phase	58
6.3	Phase-volume Effects in Few-cycle Light-matter Interactions	62
6.4	The Phase-volume Effect at 1.8 μm	66
6.5	The Phase-volume Effect at 0.8 μm	71
6.6	Further Discussion	73
6.6.1	Other Effects on the Phase Distribution	73
6.6.2	Confinement of the Interaction Volume	74
6.6.3	Phase-volume Effect on Phenomena with Different Nonlinearities	75
7	CEP-dependent Laser-matter Interactions in MIR Range	77
7.1	Strong-Field Ionization of Xe at 3.2 μm	78
7.2	Strong-field Ionization of Cs at 3.2 μm	81
7.3	Discussions	88
8	Summary and Outlook	91
	Reference	106

Publications	107
Acknowledgement	108
Erklärung	110

Abstract

Intense laser-matter interactions are generally determined by the instantaneous electric field of the laser pulse. When the laser pulse consists of only a few of optical cycles (few-cycle pulse), the so-called carrier-envelope phase (CEP) plays a critical role in light-matter interactions as the temporal variation of the electric field depends on the phase of the carrier oscillation with respect to the pulse's envelope [1]. This has a profound impact on many applications. Examples are the manipulation of the spectrum of high-harmonic generation (HHG) [2–4], control of the the emission of terahertz (THz) radiation [5–7], or isolated attosecond pulse generation [8–10] to mention just a few. More importantly, this temporal property of few-cycle pulses sculpted by the CEP provides an additional degree of freedom to control field-driven processes in atomic [11–17], molecular [18–24], and solid-state systems [25–28].

One advanced method for measuring the CEP, namely the carrier-envelope phasemeter (CEPM), which is based on the stereographic measurement of above-threshold ionization (ATI) spectra, specifically in the plateau region [29], has proven to be a robust, precise, real-time, and single-shot CEP measurement technique [30–33]. It is particularly useful in the so-called phase-tagging scheme [33], where CEP dependencies of laser-matter interactions are measured with laser pulses having randomly varying CEP by correlating the events of interest with the CEP measurement from a CEPM.

Increasing the driving laser wavelength has many advantages from multiple perspectives, such as new X-ray sources [34–39] due to the higher HHG cutoff, shorter attosecond pulses due to larger bandwidth [10, 40, 41], discovery of new phenomena such as the low-energy structure (LES) [42–47], and the investigation of electron or molecular dynamics [48–50]. To date, however, the CEPM technique has largely been confined to wavelengths close to 1 μm due to the underlying physics of above-threshold ionization [48], in particular the low yield of plateau photoelectron emission which is required for the phase

measurement.

In this thesis, we will demonstrate the development and implementation of a CEP-M based on stereo-ATI in xenon and operating at short-wave infrared (SWIR) wavelengths around $1.8\ \mu\text{m}$ at 1 kHz repetition rate. An independent high-resolution time-of-flight (TOF) photoelectron spectrometer is used to measure the CEP-dependent ATI spectra of xenon at $1.8\ \mu\text{m}$ to validate the ability of phase-tagging experiments with a CEP-M. Simultaneously to the phase measurement, by analysing the measurements from a CEP-M, the pulse length of few-cycle pulses at $1.8\ \mu\text{m}$ are also characterized. In order to verify our measurements, the experimental results are compared to simulations with two different theoretical models. Further, we will discuss the perspectives and requirements for a single-shot CEP-M operating at different wavelengths.

In the analysis of CEP-dependent light-matter interaction, we found a significant phase-averaging effect due to the spatial distribution of the CEP in focused few-cycle pulsed beams, which is much more complex than the well-known Gouy phase of monochromatic beams. In the second part of this thesis, we will demonstrate the significance of the focal phase effect, i.e. the reduction of the CEP-dependence due to averaging the CEP in the focus. By comparing the measurements and simulations of the CEP-dependent photoelectron emission in opposing directions in xenon with various laser wavelengths, we illustrate and quantify this phase-volume effect in different experimental configurations. Next, building upon this knowledge, we formulate a more general description of the impact of the focal phase for laser-matter interactions of different nonlinear orders to answer the general question: if, when, and how much should one be concerned about the phase-volume effect?

Further extension of the driven laser wavelength up to mid-infrared (MIR) range for light-matter interactions is engaging due to the characteristics of long wavelengths. Nevertheless, relevant experiments performed with MIR few-cycle pulses are still relatively rare, mainly because of the low prevalence of few-cycle MIR laser systems due to their limited pulse energy and low repetition rates. In the last part of the thesis, strong-field ionization of xenon using $3.2\text{-}\mu\text{m}$ few-cycle pulses as a benchmark will be studied and its CEP-dependence will be analyzed. Next, by averaging large numbers of laser shots, the prospects of a xenon-based CEP-M operating at this wavelengths was tested and the first CEP measurements will be presented. In order to find an alternative target for a single-

shot CEPM at MIR wavelengths, strong-field ionization of an alkali atom, namely caesium, will be investigated. The CEP-dependent photoelectron spectra of caesium using 3.2 μm few-cycle pulses will be presented and compared with the simulations. We observed an anomalous energy-dependence and CEP-dependence in Cs, particularly at high intensities. The analysis based on a quantum orbit theory suggests that this unusual CEP-effect can be interpreted as the interference of two backscattered quantum orbits from adjacent optical cycles. In addition, the pulse length-dependent and intensity-dependent analysis of both species, Xe and Cs, at different wavelengths validate this explanation and proves that this effect is a universal effect independent of the type of atoms or wavelengths. This analysis provides a general condition for observing this effect.

Viewed from a higher perspective, this thesis demonstrates a precise characterization of the CEP of few-cycle pulses and an accurate analysis of phase-dependent light-matter interaction from the NIR, via the SWIR to the MIR range.

Kurzfassung

Die Laser-Materie-Wechselwirkung bei hohen Intensitäten wird durch das instantane elektrische Feld des Laserpulses bestimmt. Wenn der Laserpuls nur aus wenigen optischen Zyklen besteht (Few-Cycle-Pulse), hängt die zeitliche Variation des elektrischen Feldes stark von der Phase der Trägerwelle relativ zur Einhüllenden, der sogenannten Carrier-Envelope-Phase (CEP), ab. Da die CEP die zeitliche Variation des Laserfelds bestimmt, spielt sie eine entscheidende Rolle in der Wechselwirkung von Materie mit ultrakurzen Laserpulsen [1]. Die Messung oder gar Kontrolle der CEP von ultrakurzen Laserpulsen ist daher ein wichtiges Konzept für viele Anwendungen in der Starkfeldlaserphysik. Beispiele sind die Manipulation des Spektrums in der Erzeugung von hohen Harmonischen (HHG) [2–4], die Emission von Terahertz- (THz)-Strahlung [5–7] oder die Erzeugung isolierter Attosekundenpulse [8–10]. Noch wichtiger ist, dass die Kontrolle der Form von Few-Cycle-Pulsen durch die CEP einen zusätzlichen Freiheitsgrad zur Kontrolle der feldgetriebenen Prozessen in atomaren [11–17], molekularen [18–24] und Festkörpersystemen [25–28] bietet.

Eine sehr leistungsfähige Methode zur Messung der CEP stellt das Carrier-Envelope-Phasemeter (CEPM) dar. Es beruht auf der stereographischen Messung von Above-Threshold-Ionisation-Spektren (ATI), speziell im Plateaubereich [29], und hat sich als sehr robuste, präzise Echtzeit- und Einzelschuss-CEP-Messtechnik erwiesen [30–33]. Sie ermöglicht somit das sogenannte Phase-Tagging-Verfahren [33], bei dem die detektierten Ereignisse einer CEP-abhängigen Laser-Materie-Wechselwirkung, die von Laserpulsen mit zufällig variierender CEP erzeugt werden, mit den Ergebnissen der CEP-Messung der Laserpulse in einem CEPM korreliert werden.

Die weitere Erhöhung der Wellenlänge des treibenden Lasers hat viele Vorteile aus mehreren Perspektiven. Es ermöglicht neue Röntgenquellen aufgrund einer höheren HHG-Grenze [34–39], kürzere Attosekundenpulse aufgrund einer größeren spektralen Bandbreite

[10,40,41], die Entdeckung neuer Phänomene wie der Niedrigenergiestruktur (LES) [42–47] und die Untersuchung der Elektronen- oder Molekül-dynamik im MIR-Bereich [48–50]. Die Nutzung des CEPM war bisher jedoch weitgehend auf Wellenlängen im Bereich von $1\ \mu\text{m}$ beschränkt. Dies kann mit den physikalischen Gesetzmäßigkeiten, die der ATI zugrunde liegen [48], erklärt werden. Der Grund ist vor allem die für längere Laserwellenlängen verringerte Ausbeute an Photoelektronen im Plateaubereich, die für die Phasenmessung benötigt werden.

In der ersten Hälfte dieser Arbeit werden wir die Entwicklung und Implementierung eines CEPM demonstrieren, das auf Stereo-ATI in Xenon basiert und im kurzwelligen Infrarot (SWIR) bei Wellenlängen um $1,8\ \mu\text{m}$ und $1\ \text{kHz}$ Puls wiederholrate arbeitet. Ein hochauflösendes TOF-Photoelektronenspektrometer wird verwendet, um die CEP-abhängigen ATI-Spektren von Xenon bei $1,8\ \mu\text{m}$ zu messen, und damit die Eignung des CEPM für Phase-Tagging-Experimente zu validieren. Um unsere Messungen zu verifizieren, werden die experimentellen Ergebnisse mit den Simulationen aus zwei verschiedenen theoretischen Modellen verglichen. Weiterhin werden wir durch diesen Vergleich auf die Perspektiven von und Anforderungen an ein CEPM diskutieren, das bei verschiedenen Wellenlängen arbeitet.

Bei der Analyse der CEP-abhängigen Licht-Materie-Wechselwirkung fanden wir einen signifikanten Phasenmittelungseffekt aufgrund der räumlichen Phasenverteilung in fokussierten Few-Cycle-Pulsen. Diese Phasenverteilung ist wesentlich komplexer als die der bekannten Gouy-Phase monochromatischer Strahlen. Im zweiten Teil dieser Arbeit werden wir die Bedeutung des fokalen Phaseneffekts, d. h. die Verringerung der CEP-Abhängigkeit aufgrund der Mittelung der CEP im Fokus, untersuchen. Durch den Vergleich von Messungen und Simulationen der CEP-abhängigen Photoelektronenemission in entgegengesetzte Richtungen in Xenon mit verschiedenen Laserwellenlängen veranschaulichen und quantifizieren wir diesen Phasenvolumeneffekt in verschiedenen experimentellen Konfigurationen. Darauf aufbauend formulieren wir eine allgemeinere Beschreibung des Einflusses der fokalen Phase für Laser-Materie-Wechselwirkungen mit unterschiedlichen nichtlinearen Intensitätsabhängigkeiten, um die allgemeinere Frage zu beantworten: Ob, wann und wie muss der Phasenvolumeneffekt beachtet werden?

Die weitere Ausdehnung der angetriebenen Laserwellenlänge bis in den mittleren Infrarotbereich (MIR) für Licht-Materie-Wechselwirkungen ist aufgrund der Eigenschaften

langer Wellenlängen sehr interessant. Dennoch sind relevante Experimente mit MIR-Pulsen mit wenigen Zyklen immer noch relativ selten, hauptsächlich wegen der geringen Verbreitung von MIR-Lasersystemen mit Pulsdauern von wenigen Zyklen, ihrer begrenzten Pulsenergie und ihren niedrigen Repetitionsraten. Im letzten Teil der Arbeit wird die Starkfeldionisation von Xenon unter Verwendung von 3,2 μm -pulsen mit wenigen Zyklen als Benchmark untersucht und ihre CEP-Abhängigkeit analysiert. Als nächstes wurden durch Mittelung einer großen Anzahl von Laserschüssen die Erfolgsaussichten eines Xenon-basierten CEPM getestet, das bei diesen Wellenlängen arbeitet, und die ersten CEP-Messungen werden präsentiert. Um ein alternatives Target für ein CEPM mit der Fähigkeit zur Messung einzelner Laserpulse für MIR-Wellenlängen zu finden, wird die Starkfeldionisation eines Alkaliatoms, nämlich Cäsium, untersucht. Die CEP-abhängigen Photoelektronenspektren von Cäsium unter Verwendung von 3.2 μm Pulsen mit wenigen Zyklen werden präsentiert und mit den Simulationen verglichen. Wir beobachteten eine außergewöhnliche Energie- und CEP-Abhängigkeit in Cs, insbesondere bei hohen Intensitäten. Die auf einer Quantenbahntheorie basierende Analyse legt nahe, dass der beobachtete CEP-Effekt als Interferenz zweier rückgestreuter Quantenbahnen benachbarter optischer Zyklen interpretiert werden kann. Darüber hinaus bestätigt die pulslängenabhängige und intensitätsabhängige Analyse beider Spezies, Xe und Cs, bei unterschiedlichen Wellenlängen diese Erklärung und beweist, dass dieser Effekt ein universeller Effekt ist, unabhängig von der Art der Atome oder Wellenlängen. Diese Analyse liefert eine allgemeine Bedingung für die Beobachtung dieses Effekts.

Aus einer höheren Perspektive betrachtet, demonstriert diese Arbeit die präzise Charakterisierung des CEP von Pulsen mit wenigen Zyklen und eine genaue Analyse der phasenabhängigen Licht-Materie-Wechselwirkung vom NIR- über den SWIR- bis zum MIR-Bereich.

Chapter 1

Introduction

1.1 Motivation

“Faster, higher and stronger,” these three simple words beautifully describes not only the spirit of Olympics, but also the direction of the progress of science and technology. From the exploration of the universe as far out as possible to the discovery the smallest fundamental elements that constitute this world, any approach requiring the power, like rockets, accelerators, lasers and among others follows this spirit. In a generalised sense, the development of science definitely requires a “power” – a power of faster detection or faster calculation, a power of reaching a higher resolution or a higher dimension, a power with stronger capability of understanding and changing the world. In this thesis, we are looking for a stronger power which allows us for precise characterization of the phase of few-cycle laser pulses and accurate analysis of phase-dependent light-matter interactions from the near-infrared (NIR), via the short-wave infrared (SWIR) to the mid-infrared (MIR) range¹.

The laser systems that we are specifically interested in follow a trend of more power, faster in pulse length, higher data acquisition by higher repetition rate and more different wavelengths [51–56]. They play a crucial role in numerous fields, from scientific research to industry, and from physics to medicine [1, 57–60]. In particular, by taking advantage of extremely short pulse durations, we are able to investigate transient light-matter interactions occurring on a time scale of femtoseconds (fs²) or even below. In addition, as the

¹NIR: 0.75 - 1.4 μm ; SWIR: 1.4 - 3 μm ; MIR: 3 - 8 μm .

²Quantity denotation: atto~ (a~): 10^{-18} ; femto~ (f~): 10^{-15} ; pico~ (p~): 10^{-12} ; nano~ (n~): 10^{-9} ; micro~ (μ ~): 10^{-6} ; milli~ (m~): 10^{-3} ; kilo~ (k~): 10^3 ; Mega~ (M~): 10^6 ; Giga~ (G~): 10^9 ;

energy of the pulse is automatically concentrated within an extremely small time window due to the short pulse length, a high peak intensity of the field can easily be achieved, which allows us to investigate many phenomena requiring a high external field strength.

In this thesis, we are interested in a situation where the laser field strength is sufficiently high and in fact, comparable to the Coulomb force binding the electrons. In this case, the atoms or molecules can be ionized even when the photon energy is much smaller than the energy required for ionization, a situation to which we refer to as the “strong-field ionization” (SFI). In this regime, many highly nonlinear laser-induced ultrafast phenomena will appear, e.g., i) above-threshold ionization (ATI) [61–64], an ionization process where the electrons absorb more photons than necessary for ionization from the field, and may even interact again with the ion core after acceleration by the field; ii) high-harmonic generation (HHG) [65–68], a process where after the ionization, the electrons recombine with the parent ion and emit high energy photons. As a consequence of HHG, attosecond (as) pulse can be obtained at short wavelengths [68–70]; iii) non-sequential double ionization (NDSI) [71–73], i.e., the emission of a second electron as a consequence of the repeated interaction of the electron with its parent ion. These interesting phenomena mentioned above and a few others constitute the field of strong-field physics [64] and attosecond physics [68].

In particular, this thesis is devoted to ATI driven by a specific type of laser pulse that only consists of a few optical cycles ($\lesssim 3$ optical cycles), the so-called few-cycle pulses. Few-cycle pulses have several intriguing properties. First, as its pulse duration is even shorter, few-cycle pulses allow for higher temporal resolution as probe light [74]. Meanwhile, few-cycle pulses have a broader spectral bandwidth, which can be utilized as a new spectral light source [75]. A very specific characteristic of few-cycle pulses is that the waveform of the pulse is sculpted by the phase between the maxima of the envelope and the maxima of the oscillating field, which is known as the “absolute phase” or the “carrier-envelope phase” (CEP). This property provides an additional degree of freedom to control laser field-driven processes and results in many applications, e.g., manipulation of the spectrum of HHG [4, 76, 77], isolated attosecond pulse generation [8–10, 38] and selection of the spectrum of terahertz (THz) radiation [5, 6]. More importantly, for those light-matter interactions depending on the instantaneous electric field, the phase-

Tera~ (T~): 10^{12} ; Peta~ (P~): 10^{15} ;

dependent phenomena become observable when interacting with few-cycle pulses. Thus, by controlling the CEP, we are able to manipulate the general dynamics of light-matter interactions in atomic [12–17, 78], molecular [19–24, 79] and solid-state systems [25, 80–83].

In order to control phase-dependent laser-matter interactions, one needs to know the CEP. In this thesis, we will introduce and discuss an advanced technique for measuring the CEP based on the measurement of high-order photoelectron emission: the so-called carrier-envelope phasemeter (CEPM) [30–33, 84, 85]. Besides its capability of robust, precise, real-time, single-shot phase measurement, this technique has several more advantages compared to conventional optical methods, e.g., the $f - 2f$ interferometer [86, 87]. Simultaneously to the phase measurement, the CEPM is able to characterize the pulse duration of few-cycle pulses [31, 32, 84, 85], which is also a challenging task based on the optical approach due to the limited spectral bandwidth of optics. In addition, as the CEPM measures the emitted photoelectrons from atoms or molecules induced by the laser field, the phasemeter can be regarded as a simple time-of-flight (TOF) spectrometer providing us some direct and intuitive insights of phase-dependent light-matter interactions.

In general, without further phase controlling measures, laser oscillators deliver pulse trains with essentially randomly fluctuating CEPs from pulse to pulse which are caused by the phase difference between the group velocity and the phase velocity accumulated in dispersive materials inside the laser cavity. In addition, as the stretcher-compressor based chirped pulse amplification (CPA) system introduces inevitable large CEP jitters [88–90], the output CEP of large scale laser systems is commonly random. Therefore, techniques for stabilizing the CEP for oscillators and amplifiers have been invented and developed [87, 88, 91–97]. However, maintaining the CEP for high-power laser systems with very small fluctuations and allowing for long-term operation has remained challenges.

An alternative approach that does not require CEP-stabilization of laser systems is to measure the CEP for each single laser pulse, which is another crucial capability of the CEPM. With synchronization of single-shot phase measurement to the observation of light-matter interactions, the desired phase-dependent information can be extracted. This is known as the “phase-tagging” scheme [33]. The single-shot scheme requires the measurement and the data acquisition to be completed within the time between two subsequent pulses. The CEPM readily satisfies this requirement and has become a standard method for phase-tagging experiments at 1 kHz repetition rate [31, 32, 85]. Recently, with

development of fast electronics and detectors, the CEPM became able to operate at a repetition rate of 100 kHz [98].

So far, due to the technical conveniences, most scientific works on strong-field light-matter interaction have been realized using high-power near-infrared lasers, e.g., Titanium-Sapphire (Ti:Sa) lasers (around 0.8 μm) [52, 99] and Ytterbium lasers (around 1 μm) [53]. Increasing the driving laser wavelengths in strong-field physics is interesting from multiple perspectives. An important application is that long wavelengths will increase the energy cutoff of HHG due to a larger ponderomotive energy³ [100, 101], which brings us new extreme ultraviolet (XUV) and X-ray sources [35, 37, 38, 102]. As a consequence of increased photon energy and bandwidth in the extreme ultraviolet, shorter attosecond pulses can be obtained [41, 100]. Another phenomenon, the so-called low-energy structures (LES) in the ATI spectrum, becomes interesting as this structure is more prominent when probing with longer wavelength pulses [42–47]. In addition, long wavelength is also interesting for investigation molecular dynamics, e.g., dissociation and electron localization due to low photon energy and its special spectral range, which covers typical resonances of vibrational states of molecules [103–105]. Recently, the realization of high-power few-cycle lasers in the SWIR and the MIR range [54, 106–109] has provided even more opportunities for the investigation of few-cycle light-matter interactions using long-wavelength pulses.

Therefore, there is a serious demand for the precise characterization of the CEP at long wavelengths. The goal of this thesis is to extend our capabilities of precise characterization of the CEP from the NIR range to the SWIR range and the MIR range, and investigate CEP-dependent light-matter interactions with long-wavelength few-cycle pulses.

1.2 Main Concepts of the Thesis

1.2.1 CEP-measurement Towards SWIR and MIR Range

Although increasing driving laser wavelengths will bring researchers many benefits, the CEPM has so far largely been confined to the NIR range due to the extremely low yield of the high-order photoelectron emission at long wavelengths [48, 85]. We will demonstrate

³Ponderomotive energy: the cycle-averaged quiver energy of a free electron in an electromagnetic field.

the development and implementation of a CEPM based on stereo-ATI⁴ in xenon (Xe) and operating at SWIR wavelength (around 1.8 μm) at 1-kHz repetition rate. Simultaneously with the phase measurement, the pulse duration of few-cycle pulses is also characterized based on the measurements from the CEPM. An independent high-resolution TOF photoelectron spectrometer is used to measure CEP-dependent ATI spectra of xenon at 1.8 μm to validate the ability of phase-tagging experiments with a CEPM.

In addition, simulated results from two theoretical models are presented, which verify our phase and pulse length measurements. In the analysis, we will discuss the possibility and requirements for a single-shot CEPM operating at different wavelengths. Further, we will present first CEP measurements with a xenon-CEPM at 3.2 μm and measurements of CEP-dependent ATI spectra of caesium (Cs) at 3.2 μm , which lay a foundation for developing a CEPM with an alkali target for MIR wavelengths.

1.2.2 Phase-volume Effect in Few-cycle Light-matter Interactions

In the process of analyzing CEP measurements, we found a discrepancy between simulated results and measurements, i.e., the simulations consistently predicted a larger phase-dependence than observed in the measurements. The main reason is that, the spatial phase distribution in a focused beam is neglected in the theoretical analysis. Even if it is taken into account, the common consideration of this phase distribution is its first-order approximation, namely, the phase distribution of a monochromatic beam, known as the “Gouy phase”. However, the phase behaviour of focused broadband pulsed beams, to which we refer as the “focal phase”, is substantially different and significantly more complex than the Gouy phase. Thus, one should expect that there are profound consequences for all broad-band laser-induced dynamics, in particular in cases where the interaction volume is comparable to the focal size, as is inevitable for isolated attosecond pulse generation, HHG, THz emission or any light-matter interactions with a focused beam. Despite its importance, this has never been demonstrated and let alone carefully analyzed.

In this thesis, we demonstrate the importance of this non-Gouy “phase-volume ef-

⁴Stereo-ATI means using two opposing time-of-flight spectrometers such that photoelectron spectra for CEPs differing by 180° are simultaneously recorded.

fect” on light-matter interactions, i.e., the effect that complex spatial distributions of the carrier-envelope phase (CEP) of few-cycle laser pulses, have on measuring and interpreting CEP-dependent dynamics. First, we compare the quantitative difference between the Gouy phase and the focal phase in strong-field ionization of xenon and we prove that only considering the Gouy phase is insufficient, as the majority of CEP-dependent effects become observable only when the pulse duration consists of a few optical cycles, which implies an extremely broad frequency bandwidth.

Therefore, for a precise characterization of the CEP-dependence, one needs to consider a more realistic focal phase in the analysis. We apply an improved model of describing the phase distribution of a broadband pulse derived by M. A. Porrás [110–112]. Once we include the complex phase distribution close to the experimental conditions, a better agreement has been achieved between the measurements and the simulations. Moreover, building upon the knowledge of the phase-volume effect that we analyzed from the strong-field ionization of xenon, we formulate a more general description of the impact of the focal phase on laser-matter interactions with different nonlinear intensity-dependencies to answer the general question: if, when, and how much should one be concerned about the phase-volume effect? This allows us a more accurate modelling and interpretation of CEP-dependent phenomena, as well as a more precise determination of the phase of laser pulses.

1.2.3 High-order CEP-dependence in the Asymmetry Map of Cs

In the investigation of CEP-dependent strong-field ionization of Cs with MIR few-cycle pulses, we observed an unusual CEP-dependence in the asymmetry⁵ map. In previous experiments, the CEP-dependent asymmetry at a certain photoelectron energy oscillates as fast as the variation of the CEP. However, we found that at high laser intensities, the asymmetry in the typical plateau region for rescattered electrons oscillates three times as fast as the variation of the CEP. By applying the improved strong-field approximation method, the high-order CEP-dependent effect is interpreted as the interference of two quantum orbits initiated in subsequent laser cycles.

⁵The asymmetry means the normalized difference in differential electron yield for pulses with a phase difference of π .

In addition, the numerical calculations by solving the time-dependent Schrödinger Equation (TDSE) further help us understanding the conditions for observing this effect. By analyzing the calculated intensity- and pulse length-dependent asymmetry maps for different species, two general questions will be answered: why was this effect only observed at high intensities and why was this effect rarely found in previous experiments? At last, the TDSE analysis by switching the regime between the multiphoton ionization and tunnelling ionization by shifting the wavelength and changing the potential of the atom, provides a solid proof that this high-order CEP-effect is an universal effect in the sense that it is independent of the atom species and the wavelength of the driven laser field.

1.3 Structure of the Thesis

In the previous sections, we introduced the motivation and main concepts of this thesis. In Chapter 2, a short review of the theoretical background of strong-field physics will be presented. First, different ionization mechanisms will be briefly discussed. Next, a semi-classical description of strong-field laser-matter interaction, known as the “three-step model”, is introduced and explained. The model provides an intuitive picture of strong-field processes. In the last section of Chapter 2, strong-field processes induced by few-cycle pulses will be shortly analyzed to demonstrate the impact of the CEP.

In Chapter 3, two theoretical models used in this thesis for simulating the strong-field processes are introduced. One is a semi-classic model based on the three-step description discussed in Chapter 2. The other one is a numerical calculation based on a quantum description by solving the one-dimensional time-dependent Schrödinger equation [64].

In Chapter 4, the laser systems with which we performed our experiments, the experimental setups and the working principle of the core technical instrument for measuring the CEP, the carrier-envelope phasemeter, will be discussed in detail.

The experimental results of single-shot CEP measurement as well as the pulse duration measurement at 1.8 μm with a CEPM will be presented in Chapter 5. The measurements are further compared with simulated results from two models that were mentioned in Chapter 3. In the discussion section of Chapter 5, we will analyze the prospects and requirements for single-shot CEP measurements with a CEPM. This provides us with a general scaling insight for implementing a single-shot CEP-measurement based on the

measurement of stereo-ATI at different wavelengths.

In Chapter 6, the spatial phase distribution of a focused broadband beam is introduced and compared to the Gouy phase of a focused monochromatic beam. Due to the complex phase distribution of a focused broadband beam, a significant phase-averaging effect is observed in few-cycle light-matter interactions. It is referred to as the “phase-volume effect”. By using strong-field ionization of xenon at different wavelengths as a baseline, we further generalize this effect in laser-matter interactions with different nonlinear intensity dependencies, which allows us more accurate modelling and interpretation of various CEP-dependent few-cycle laser-induced processes.

In the next chapter (Chapter 7), the CEP-dependent ATI spectra of xenon measured at 3.2 μm will be presented as a benchmark and first CEP-measurements with a xenon-based CEP-M at MIR wavelength will be presented. This lays a foundation of developing the CEP-M and future researches on CEP-dependent strong-field phenomenon in MIR range.

We further investigate strong-field ionization of caesium and, in parallel, test its potential for replacing xenon as a target in a CEP-M that can be operated at long wavelengths. Worth to emphasize that we observed an unusual high-order CEP-dependence in the asymmetry map of Cs at high-intensities, e.g., $> 2 \text{ TW/cm}^2$. By using an improved strong-field approximation model, this effect is interpreted as the interference between different quantum orbits initiated in subsequent laser cycles. In addition, numerical solutions from the TDSE confirms the existence of this effect. By analysing the intensity- and pulse length-dependent asymmetry of two species of atom, at different wavelengths, we find out some rough conditions for observing the high-order CEP-effect.

In the last chapter, we will summarize this thesis and an outlook related to this work will be given and briefly discussed.

Chapter 2

Theoretical Background

It is well-known that in 1905, a figure no less than Albert Einstein proposed that matter absorbs light in quanta. It is much less known that he also considered that if the light intensity is sufficiently high, more than one energy quantum from the incident light can be simultaneously transferred to a photoelectron [113]. Like many of his other tremendous predictions, he was right again. This energy quanta of the light later became known as “photons” [114] and multiphoton processes indeed occur when the intensity of the light is high enough. In 1931, Maria Goeppert Mayer¹, the second female winner of a Nobel Prize in physics, calculated the cross-section of two-photon absorption by atoms in her dissertation [115]. Because of too low field strength at that moment, first experimental observations of two-photon absorption were achieved nearly 30 years later [116, 117] until the invention of the laser [118, 119] around 1960. Since then, an uncounted number of experimental observations of multiphoton ionization (MPI) have been demonstrated [120–123].

With the invention and development of laser technologies, e.g., chirped-pulse amplification (CPA) [124], the strength of the light field can easily reach the level of the atomic Coulomb field, i.e., $E_a = e/4\pi\epsilon_0 a_0^2 \simeq 5.1 \times 10^9$ V/cm, where e is the absolute value of the electron charge, ϵ_0 is the permittivity of free space and a_0 is the first Bohr radius of atomic hydrogen. The corresponding intensity of the field is $I_a = \frac{1}{2}\epsilon_0 c E_a^2 \simeq 3.5 \times 10^{16}$ W/cm². Nowadays, much higher intensity beyond 10^{20} W/cm² can be realized with a terawatt (TW) or petawatt (PW) laser [125–127] and of course, researchers are still making great

¹Maria Goeppert Mayer won the Nobel Prize in physics for proposing the nuclear shell model. The cross-section of two-photon absorption of atoms is named after her: 1 GM = 10^{-50} cm⁴s/photon.

efforts to bring the field intensity to a higher level. Actually, multiphoton processes with visible photons may occur at an intensity around 10^8 W/cm^2 , usually with small probabilities though. At low intensities, the multiphoton process can be analyzed using perturbation theory. In this thesis, we focus on the typical strong-field regime that the intensity with 1-3 orders lower than the I_a where the general multiphoton phenomena beyond the perturbation regime become highly evidently and dominant but are still in the non-relativistic regime. In this chapter, we will provide the theoretical background of the strong-field phenomena that are relevant to the central themes of this thesis.

2.1 Strong-field Ionization (SFI)

2.1.1 Multiphoton Ionization (MPI)

For single ionization, the MPI process can be described as

$$A^q + n\hbar\omega = A^{q+1} + e^-, \quad (2.1)$$

where q is the charge of a target atomic system A , ω is the frequency of the light, and n is the number of photons absorbed. For not too high intensities, the rate of a n -photon process is proportional to I^n , which is in agreement with the description of lowest-order perturbation theory [64]. In 1979, Agostini [61] discovered that under high-intensity conditions, the ionized electron can absorb more photons than the minimum number that is required for ionization. This phenomenon was given the name ‘‘above-threshold ionization’’ (ATI). The typical photoelectron spectrum consists of several peaks separated by the one photon energy $\hbar\omega$ and the energy of these peaks satisfies

$$E_n = (n_0 + n)\hbar\omega - I_P, \quad (2.2)$$

where n_0 is the minimum number of photons required for ionization, I_P is the ionization potential of the atom and $n = 0, 1, 2 \dots$, is the number of photons absorbed by the atom exceeding the minimum number for exceeding the ionization potential. At rather low intensities, the ionization rate for an (n_0+n) -process is proportional to I^{n_0+n} following the lowest-order perturbation theory. The schematic of the mechanism of the ATI spectrum [64] and typical measured ATI spectra at rather low intensities are shown in Fig. 2.1.

As the intensity of the external field is increased, the Rydberg and continuum states of the atoms are shifted to higher energy levels, which is known as the AC-Stark effect

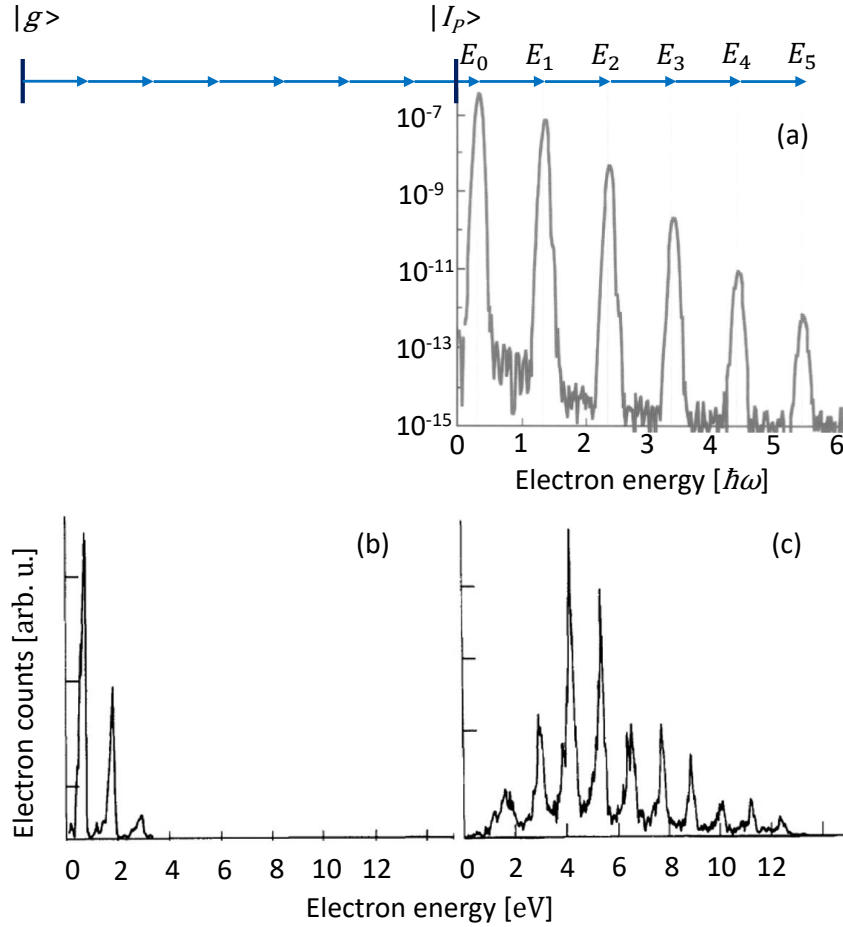


Figure 2.1: Schematic of the mechanism of the above-threshold ionization spectrum. (a) Numeric solution from the time-dependent Schrödinger equation [64]. (b), (c) One example of measured ATI of xenon with a 1064-nm, 130-ps laser at intensity around $2.2 \times 10^{12} \text{ W/cm}^2$ and $1.1 \times 10^{13} \text{ W/cm}^2$ [128].

[129, 130]. The energy shift is given by the ponderomotive energy U_p , which is the cycle-averaged kinetic energy of a quivering electron in a laser field:

$$U_p = \frac{e^2 E_0^2}{4m\omega^2} \sim \frac{I}{\omega^2} \sim I \cdot \lambda^2, \quad (2.3)$$

where E_0 is the electric field strength, m is the electron mass, I is the intensity of the field, and λ the wavelength of the field. Thus, the required energy for ionization is also shifted and the photoelectron energies are given by

$$E_N = (n_0 + n)\hbar\omega - (I_p + U_p). \quad (2.4)$$

A simple schematic for the AC-Stark shift of the ATI peaks is presented in Fig. 2.2 and

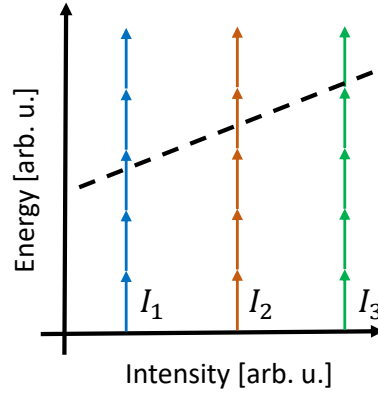


Figure 2.2: Schematic of the mechanics of the AC-Stark shift. The dashed line presents the ionization energy. For example, 3, 4 and 5 photons are required for ionization at intensities I_1 , I_2 , and I_3 , respectively.

the effect of the suppression in lower orders of the ATI peaks due to the Stark shift can be also seen in the measurements, see Fig. 2.1(c).

2.1.2 Tunnelling Ionization (TI)

When the field strength is sufficiently large, the Coulomb potential of bound electrons is modulated by the instantaneous laser field and forms a potential barrier. In this case, the electron can “tunnel” through the barrier at low laser frequencies and becomes free. Accordingly, this transient process is called tunnelling ionization (TI), shown in Fig. 2.3(b). Experiments have presented evidence that photoelectrons generated by the TI process can acquire energies of more than dozens of photon energies [63, 131, 132]. More importantly, the intensity of high-order peaks in the ATI spectra does not decay exponentially. Instead, a plateau-like annex in the photoelectron kinetic energy spectra appears.

In 1965, L. V. Keldysh first categorized MPI and TI mathematically [133]. By comparing the ratio between the required tunnelling time and the oscillation period of the laser field, he introduced a dimensionless adiabaticity parameter γ to for classification of two ionization mechanisms, today referred to as the “Keldysh parameter”:

$$\gamma = \frac{\omega\sqrt{2m_e I_P}}{eE} = \sqrt{\frac{I_P}{2U_p}}. \quad (2.5)$$

For $\gamma \gg 1$, the intensity of the field is rather low or the frequency of the laser field is high, which corresponds to the multiphoton regime. In contrast, for the same I_P , $\gamma \ll 1$

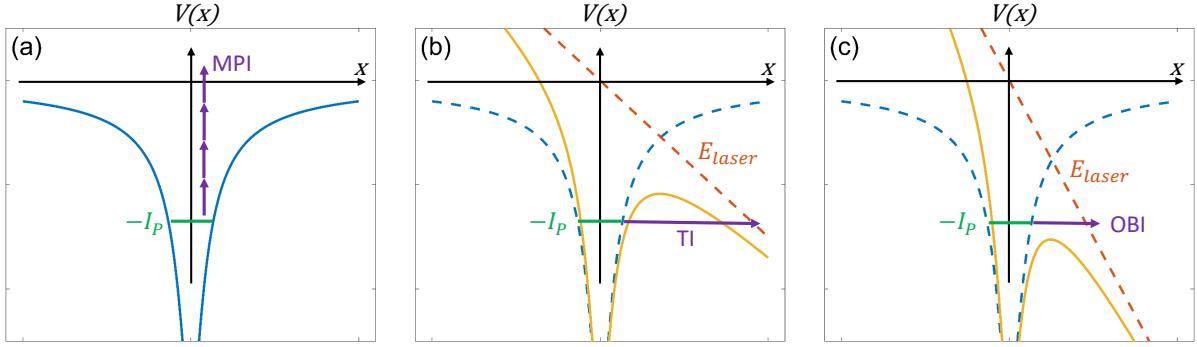


Figure 2.3: Schematics of the mechanics of strong-field ionization. Blue lines are for the Coulomb potential, red dashed lines are for the laser field and the yellow lines are for the effective potential with the laser field. I_P is the ionization potential.

corresponds to the situation where the transient potential barrier is sufficiently small and exists sufficiently long to allow tunnelling with appreciable probability. This is the tunnelling regime. The existence of these mechanisms has been observed and predicted both experimentally and theoretically [122, 134, 135].

From the Keldysh theory, A. M. Perelomov, V. S. Popov and M. V. Terent'ev derived an analytical formula for calculation of the ionization rate of a state bound by a short-range potential for an arbitrary γ parameter, known as the ‘‘PPT-rate’’ [136, 137]. Based on this rate, M. V. Ammosov, N. B. Delone and V. P. Krainov further improved this model with quasiclassical approximation for $\gamma \ll 1$, which is known as the ‘‘ADK-rate’’ [138]. Due to their similarities, in many literatures, both models are categorized as the ADK-theory [139].

The ADK ionization rate for tunnelling ionization in oscillating fields is:

$$\Gamma(t) = \frac{|C_{nl}|^2 Q^2(l, m)}{(2\kappa)^{|m|} |m|!} \cdot \left(\frac{2\kappa^2}{|E(t)|} \right)^{\frac{2Z}{\kappa} - |m| - 1} \cdot \exp\left(-\frac{2\kappa^3}{3|E(t)|}\right), \quad (2.6)$$

where $\kappa = \sqrt{2I_P}$, $n^* = Z/\kappa$ is the effective principle quantum number, Z is the atomic charge, l is the angular quantum number, and m is the magnetic quantum number. The coefficient $Q(l, m)$ is given by:

$$Q(l, m) = (-1)^{(|m|-m)/2} \sqrt{\frac{(2l+1)(l+|m|)!}{2(l-|m|)!}}, \quad (2.7)$$

and the coefficient C_{nl} is an atomic species dependent parameter, for which different atoms can be found in Refs. [140–142].

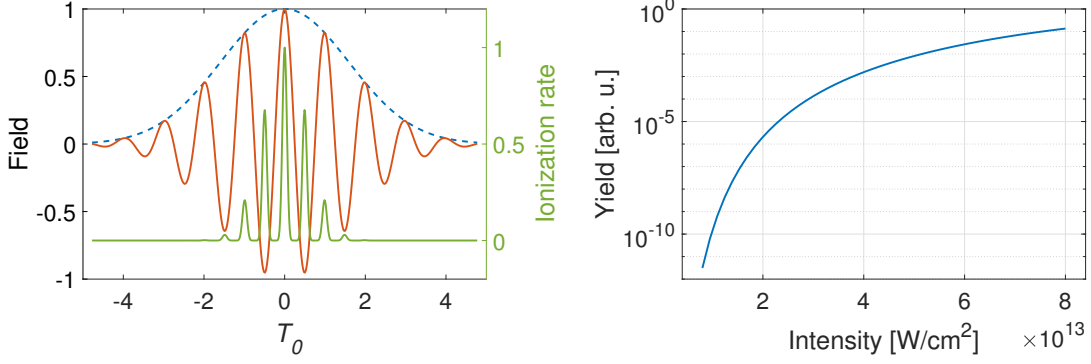


Figure 2.4: One example of the ionization rate calculated using the ADK-rate for xenon atoms. (a) Field-dependent yield at peak intensity of $8 \times 10^{13} \text{ W/cm}^2$. (b) Intensity-dependent ionization rate of xenon.

The ADK-rate, which is a cycle-averaged ionization rate, is well suitable for $\gamma \ll 1$ [122]. In our case, e.g., ionization of xenon atoms at $0.8 \mu\text{m}$ with a peak intensity around $0.8 \times 10^{14} \text{ W/cm}^2$, the γ is close to 1, which is a situation that the multiphoton ionization also plays a important role. In addition, we are investigating the strong-field ionization with few-cycle pulses where the sub-cycle dynamics is important. Thus, we apply a modified ionization rate [143] suitable for both situations, i.e., $\gamma \sim 1$ and interacting with few-cycle pulses:

$$\Gamma(t) = \frac{|C_{nl}|^2 Q^2(l, m)}{(2\kappa)^{|m|} |m|!} \cdot \left(\frac{2\kappa^2}{|E(t)|} \right)^{\frac{2Z}{\kappa} - |m| - 1} \cdot C_\gamma \cdot \sqrt{\frac{3\kappa_\gamma}{\gamma_t}} \cdot \exp \left[-\frac{E_0^2 E_{nv}^2(t)}{\omega^3} F(\gamma_t, \phi_t) \right], \quad (2.8)$$

where C_γ is the Coulomb preexponential factor (see in Ref. [136]), $E_{nv}(t_i^k)$ is the normalized envelope of the pulse, $\gamma_t = \gamma/E_{nv}(t_i^k)$, and $\kappa_\gamma = \ln(\gamma_t + \sqrt{\gamma_t^2 + 1} - \frac{\gamma_t}{\sqrt{\gamma_t^2 + 1}})$. The term of $F(\gamma_t, \phi_t)$ in Eq. 2.8 is a γ_t - (γ with respect to the envelope) and phase-dependent function:

$$F(\gamma_t, \phi_t) = (\gamma_t + \sin^2 \phi_t + \frac{1}{2}) \ln c^* - \frac{3\sqrt{b^* - a^*}}{2\sqrt{2}} \sin |\phi_t| - \frac{\sqrt{b^* + a^*}}{2\sqrt{2}}, \quad (2.9)$$

with

$$\begin{cases} a^* = 1 + \gamma_t^2 - \sin^2 \phi_t; \\ b^* = \sqrt{a^{*2} + 4\gamma_t^2 \sin^2 \phi_t}; \\ c^* = \left[\left(\sqrt{\frac{b^* + a^*}{2}} + \gamma_t \right)^2 + \left(\sqrt{\frac{b^* - a^*}{2}} + \sin |\phi_t| \right)^2 \right]^{\frac{1}{2}} \end{cases} \quad (2.10)$$

where $\phi_t = \omega t + \phi$ is the phase of the pulse. The simulated results in Chapter 5, 6 and 7 calculated from the semi-classic three-step model is obtained using this ionization rate.

Note that there is another ionization mechanism, called over-the-barrier ionization (OBI), or barrier-suppression ionization, when the laser field is so intense that the barrier of the potential is suppressed below the ground state level as shown in Fig. 2.3(c). In this case, the approximations based on TI are no longer valid. Commonly, the intensity, at which the maxima of the effective potential barrier are equal to ionization potential of bound electrons, is defined as the barrier-suppression intensity (BSI). For instance, the BSI is $\sim 0.8 \times 10^{14}$ W/cm² for xenon atoms. Improved ionization rates for the BSI can be found in Refs. [139, 144].

2.2 The Strong-field Phenomena and the Three-step Model

In 1993, P. B. Corkum introduced a semi-classical model [145], the so-called the three-step model, which beautifully describes strong-field phenomena such as the high-order ATI spectrum, HHG and NSDI. This model well explains strong-field light-matter interactions and provides an intuitive physical picture of the dynamics.

The three-step model proceeds as follows: 1) The bound electrons are ionized to the continuum through one of the ionization processes mentioned in the previous section. 2) After ionization, the free electrons are assumed of interacting with the laser field only. The dynamics of free electrons driven by the field can largely be treated classically. Depending on the ionization time, electrons driven by the field may directly fly away from the parent ion for good or they may travel back to the parent ion. Those electrons that never come back are called direct electrons. 3) Electrons that are driven back to their parent ions will further interact with the ion potential. There are mainly three interaction mechanisms: i) electrons may get recaptured by the ions and become bound electrons again, resulting in the emission of high-energy photons, which is the well-known HHG. The photon energy is the sum of the kinetic energy that was acquired from the laser field after the ionization and the ionization energy of the atom; ii) Instead of recombination to the parent ion, electrons may experience the potential of the ion and scatter. If the electrons scatters inelastically, the energy can be transferred to the bound electrons leading to the emission of a second electron. This process is known as the NSDI; iii) If the electrons scatter at the ions elastically, they will be accelerated by the field again. These rescattered

electrons can have energies beyond 10 times of ponderomotive energy depending on their scattering momentum determined by the ionization time and the scattering angle. This is the mechanism of high-order ATI, on which we mainly focus in this thesis.

2.2.1 Direct Electrons

In this thesis, we mainly discuss laser fields with linear polarization. Assume a monochromatic plane wave:

$$\mathbf{E}(t) = E_0 \cos(\omega t + \varphi) \mathbf{e}_z. \quad (2.11)$$

where \mathbf{e}_z is the polarization direction. Next, we define the vector potential of the field:

$$\mathbf{A}(t) = - \int E(t) dt = - \frac{E_0}{\omega} \sin(\omega t + \varphi) \mathbf{e}_z. \quad (2.12)$$

We neglect the Coulomb potential after the ionization, as the quiver amplitude $\alpha_q = E_0^2/\omega$ of emitted electrons is much larger than the atomic radius, e.g., $\alpha_q \approx 16.5$ a.u.² for $0.8 \mu\text{m}$ at intensity of $1 \times 10^{14} \text{ W/cm}^2$. The electron in the field can be described simply by the equation of motion (in atomic units):

$$\ddot{\mathbf{z}}(t) = -\mathbf{E}(t). \quad (2.13)$$

Integration over the time yields the electron velocity

$$\dot{\mathbf{z}}(t) = \mathbf{v}(t, t_i) = - \int_{t_i}^t \mathbf{E}(t') dt' + \mathbf{v}_0 = \mathbf{A}(t) - \mathbf{A}(t_i) + \mathbf{v}_0, \quad (2.14)$$

where t_i is the time at which ionization had occurred. Further integration over time yields the trajectory of the emitted electron in the laser field.

$$\mathbf{z}(t, t_i) = [\dot{\mathbf{z}}(t_i) - \mathbf{A}(t_i)] \times (t - t_i) + \int_{t_i}^t \mathbf{A}(t') dt' + \mathbf{z}_0, \quad (2.15)$$

where \mathbf{v}_0 and \mathbf{z}_0 are the initial velocity and the initial position of the electron immediately after the ionization. Assuming that the initial velocity $\mathbf{v}_0 = 0$ and $\mathbf{A}(-\infty) = \mathbf{A}(\infty) = 0$ for $t \rightarrow \infty$, the final momentum of emitted electrons can be written as

$$\mathbf{p}_f = \mathbf{v}(t = \infty, t_i) = -\mathbf{A}(t_i). \quad (2.16)$$

As we can see, the final momentum of the electron is directly linked to the vector potential at the initial ionization time, t_i . The corresponding final electron energy is

$$\mathcal{E}_f = \frac{v^2(t = \infty, t_i)}{2} = \frac{A^2(t_i)}{2} = \frac{E_0^2}{2\omega^2} \sin^2(\omega t + \varphi) = 2U_p \sin^2(\omega t + \varphi). \quad (2.17)$$

²a.u. – atomic unit.

Thus, for direct electrons, which never return back to the parent ions, the maximum of energy they can acquire from the laser field is twice of the ponderomotive energy. Under suitable conditions, this limit can be recognized in the ATI spectra and is known as the $2U_p$ -cutoff.

2.2.2 Returning Electrons

For electrons that return to the parent ion, the electron position z at return time t_r equals zero. With the approximation that the initial position z_0 and the initial velocity v_0 are both 0, Eq. 2.15 can be written as

$$F(t_r) = F(t_i) + F'(t_i)(t_r - t_i), \quad (2.18)$$

with $F(t) = \int A(t')dt'$. Eq. 2.18 has a graphical interpretation that yields the connection between the ionization time, t_i , and the return time, t_r . t_r is found as the intersection of the tangent at $E(t)$ at t_i with $E(t)$ [146], see Fig. 2.5(a). Some returning electrons may pass by the core upon their first return but are driven by the field such that they return to the core a second, third or even more times to the ion at subsequent crossing points indicated in Fig. 2.5(a).

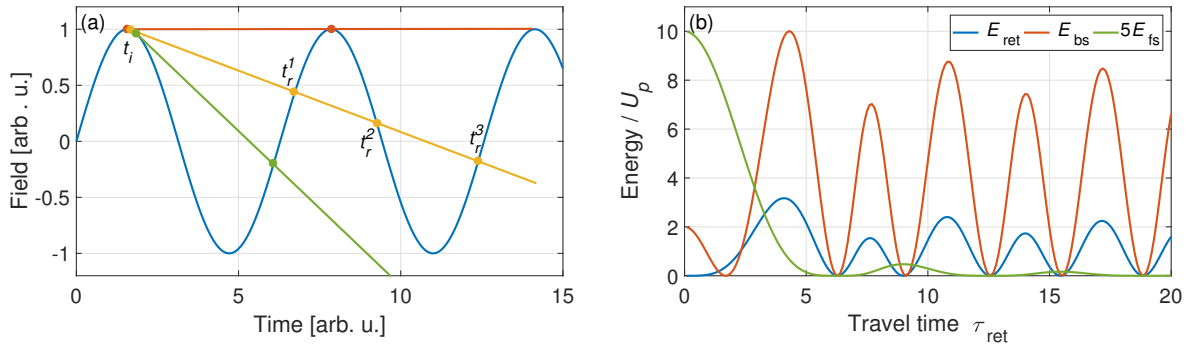


Figure 2.5: (a) Schematic description of the return time corresponding to various ionization time. t_r^1 , t_r^2 and t_r^3 indicate the first, second and third return time, respectively. (b) Final kinetic energy of return electrons, forward scattering electrons and backward scattering electrons with respect to the travel time, reproduced from Ref. [147].

The return energy can be calculated from the Eq. 2.12

$$\mathcal{E}_{ret} = \frac{[A(t_r) - A(t_i)]^2}{2}. \quad (2.19)$$

By introducing a parameter called the travel time $\tau_{\text{tr}} = \omega(t_r - t_i)$, (c.f. Ref. [147, 148]), the return energy is given by

$$\mathcal{E}_{\text{ret}} = 2U_p \frac{(2 - 2 \cos \tau_{\text{tr}} - \tau_{\text{tr}} \sin \tau_{\text{tr}})^2}{f(\tau_{\text{tr}})}, \quad (2.20)$$

with $f(\tau_{\text{tr}}) = 2 + \tau_{\text{tr}}^2 - 2 \cos \tau_{\text{tr}} - 2\tau_{\text{tr}} \sin \tau_{\text{tr}}$. The numerical solution of this equation by finding the proper travel time results in a maximum return energy of $\sim 3.17U_p$. This property reveals the physical origin of the HHG cutoff at $3.17U_p + I_P$ [66, 100]. The kinetic energy of returning electrons depending on the travel time is shown in Fig. 2.5(b). Note that the maximum return energy can be achieved only for the first return.

2.2.3 Rescattered Electrons

Alternatively, when the electrons are driven back to the parent ions, they may interact with the Coulomb potential again and rescatter elastically or inelastically. In this thesis, we mainly focus on the high-energy ATI spectrum owing to elastic scattering. If the electron rescatters with a scattering angle θ_{res} with respect to its incoming momentum, its velocities along and perpendicular to the polarization direction after the rescattering are [149]

$$\mathbf{v}_z(t) = [\mathbf{A}(t) - \mathbf{A}(t_r)] + \cos \theta_{\text{res}} \cdot [\mathbf{A}(t_r) - \mathbf{A}(t_i)]; \quad (2.21)$$

$$\mathbf{v}_x(t) = \sin \theta_{\text{res}} \cdot [\mathbf{A}(t_r) - \mathbf{A}(t_i)]. \quad (2.22)$$

The angle of the electron finally measured by the detector θ_f is given by

$$\cot(\theta_f) = \frac{\mathbf{v}_z}{\mathbf{v}_x} = \cot \theta_{\text{res}} - \frac{\mathbf{A}(t_r)}{\sin \theta_{\text{res}} \cdot [\mathbf{A}(t_r) - \mathbf{A}(t_i)]} \quad (2.23)$$

Similar to Eq. 2.20, the electron energy for two extreme characteristic cases: $\theta_{\text{res}} = 0$ (forward scattering) and $\theta_{\text{res}} = \pi$ (backward scattering) where the maximum energy can be reached, are given by [147]

$$\mathcal{E}_{\text{fs}} = 2U_p \frac{(1 - \cos \tau_{\text{tr}})^2}{f(\tau_{\text{tr}})}; \quad (2.24)$$

$$\mathcal{E}_{\text{bs}} = 2U_p \frac{(3 - 3 \cos \tau_{\text{tr}} - 2\tau_{\text{tr}} \sin \tau_{\text{tr}})^2}{f(\tau_{\text{tr}})}. \quad (2.25)$$

For this two cases, the maximum kinetic energy acquired from the laser field can be reached, e.g., $2U_p$ for forward scattering and $10.007U_p$ for backward scattering. $10U_p$ is known as the cutoff of the ATI plateau [149, 150]. The final energy for rescattered

electrons with respect to the travel time is shown in Fig. 2.5(b). The maximum energy for back-scattered electrons can only be achieved for the first return to the ions. Note that for forward scattering, the energy range is $\leq 2U_p$, which is overlapping with the direct electron distribution. These two process commonly compete with each other. If the potential is rather short-ranged, the direct electrons dominate, but the yield of forward scattering can be large for long-range potentials.

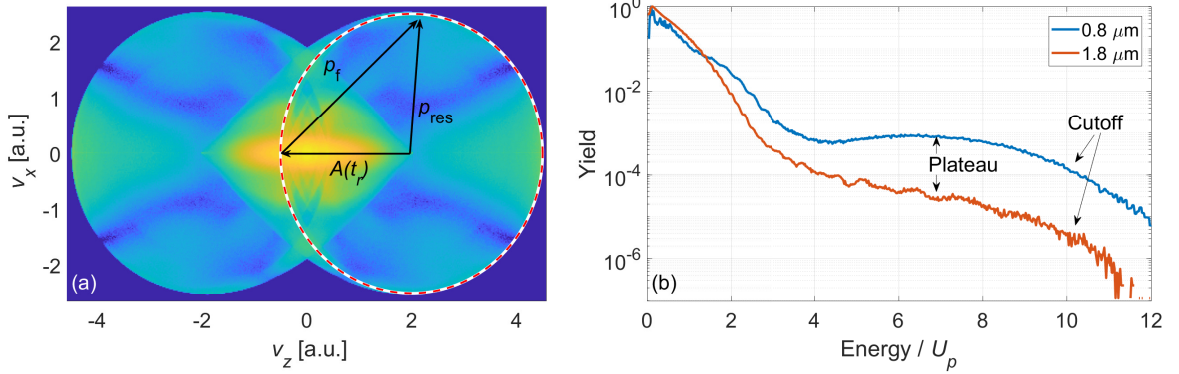


Figure 2.6: (a) An example of CEP-averaged photoelectron momentum distribution (PEMD) of xenon calculated by a semi-classic simulation with 1.8 μm - few-cycle pulses at a peak intensity of $0.8 \times 10^{14} \text{ W/cm}^2$. $A(t_r)$ is the vector potential at the return time t_r , p_{res} is the rescattered momentum and p_t is the transferred momentum. (b) An example of measured CEP-averaged ATI spectra of xenon ionized by 0.8 μm - and 1.8- μm few-cycle pulses at a peak intensity of $\sim 0.8 \times 10^{14} \text{ W/cm}^2$.

In general, the final kinetic energy for rescattering for an arbitrary angle can be calculated by

$$\mathcal{E}_{res}(\theta_{res}) = \mathbf{A}(t_r)[\mathbf{A}(t_r) - \mathbf{A}(t_i)](1 - \cos \theta_{res}) + \frac{\mathbf{A}(t_0)^2}{2}. \quad (2.26)$$

Fig. 2.6(a) shows an example of the photoelectron momentum distribution (PEMD) of xenon for 0.8- μm pulses at a peak intensity of $0.8 \times 10^{14} \text{ W/cm}^2$. $A(t_r)$ is the vector potential at the return time t_r , p_{res} is the rescattered momentum and p_f is the transferred momentum. This two dimensional momentum distribution of photoelectrons can directly be measured by velocity map imaging (VMI) techniques [151–153], which allows for investigating the angular distributions of light-matter interactions and results in many applications [154–158, 158].

Stereo-ATI is measured with two opposing TOF spectrometers aligned parallel to the polarization axis, which corresponds to the integration of the PEMD within a cone

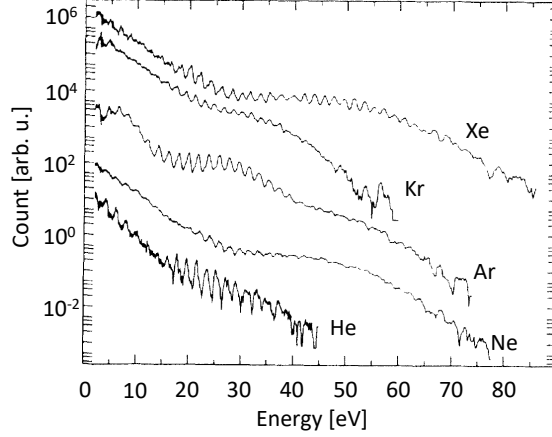


Figure 2.7: ATI spectra of rare gases with multi-cycle pulses, from Ref. [29]. The peak intensity was $3 \times 10^{14} \text{ W/cm}^2$ for He and $2 \times 10^{14} \text{ W/cm}^2$ for others.

angle according to the detector geometry along the polarization axis. Fig. 2.6(b) shows examples of measured CEP-averaged ATI spectral of xenon ionized by 0.8- μm and 1.8- μm few-cycle pulses at a peak intensity of $\sim 0.8 \times 10^{14} \text{ W/cm}^2$. The energy range up to $2U_p$ corresponds to direct electrons and forward scattered electrons. Starting from $2U_p$, there is the plateau region up to the $10U_p$ -cutoff. Note that as the ATI spectra presented in Fig. 2.6(b) are measured with few-cycle pulses, there are hardly any interference from the photoelectrons generated in different optical cycles, i.e., no ATI peaks. Thus, the spectra are rather smooth. Typical ATI spectra produced by multi-cycle pulses with ATI peaks separated by one photon energy can be seen in Fig. 2.7 [29].

2.2.4 Strong-field Phenomena Induced by Few-cycle Pulses

A Gaussian-shaped pulse in time domain is commonly described as

$$E(t) = E_0 e^{-2\ln 2(t/\tau)^2} e^{-i(\omega_0 t + \phi)}. \quad (2.27)$$

where ϕ is the phase shift between the maxima of the envelope and peak of the oscillation, which is the so-called “absolute phase” or the “carrier-envelope phase” (CEP). It originates from the phase difference between the group velocity and the phase velocity while pulses propagate through dispersive materials. When the pulses have multiple optical cycles, phase-dependent phenomena can not obviously be observed because the laser field is symmetric with respect to the polarization axis. However, when the pulses consist one

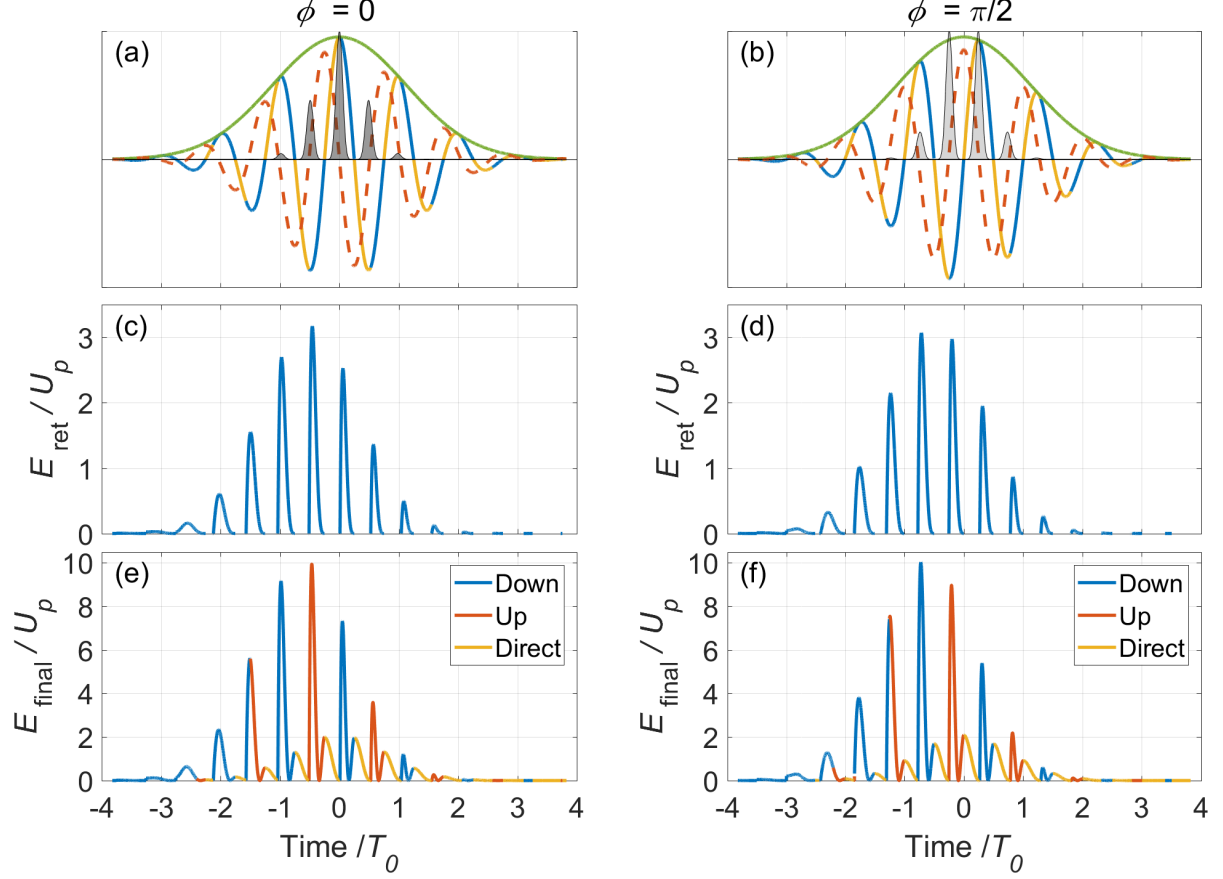


Figure 2.8: (a), (b) Illustration of asymmetry effects in strong-field photoionization by few-cycle pulses with CEPs equal to 0 and $\pi/2$, respectively. The green line is the envelope of the pulse. Yellow lines are the electric field where the ionized electrons cannot return to the parent ions and blue lines are the electric field where recombination and rescattering may occur. The red dashed line is the vector potential of the field. Gray shadow presents the instantaneous intensity-dependent ionization yield. (c), (d) The return energy of electrons for $\phi = 0$, and $\pi/2$, respectively. (e), (f) Final kinetic energy of on-axis electrons with $\phi = 0$, and $\pi/2$, respectively. The blue and red lines are for electrons emitted in opposite directions, i.e., downwards and upwards according to the direction of the vector potential. The yellow lines are for the direct electrons.

or a few optical cycles only, the CEP plays a critical role in light-matter interactions as the electron dynamics is dictated by the electric field rather than the pulses' envelope.

Fig. 2.8(a) and (b) show few-cycle pulses with different CEPs. Laser fields with different phases lead to different energy spectra, as evident from, e.g., the phase-dependent return energy of electrons, see Fig. 2.8(c) and (d). In addition, the intensity-dependent ionization yield [gray shadow in (a) and (b)], will lead to additional variance of the photoelectron spectrum. Research on few-cycle laser-matter interactions now can proceed in two directions: The phase-dependence can be investigated, or inversely, the CEP of the pulses can also be characterized based on analysis of the measurement of CEP-dependent phenomena.

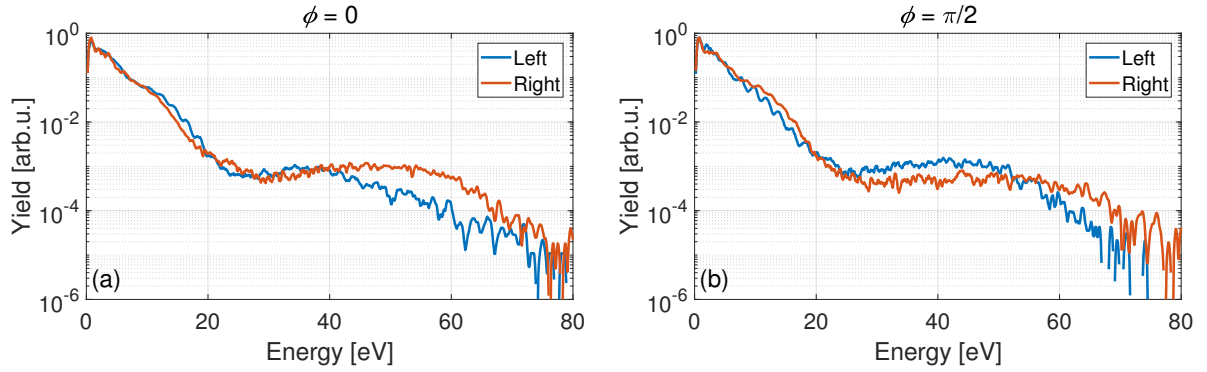


Figure 2.9: (a),(b) CEP-dependent ATI spectra of xenon for $\phi = 0$, and $\pi/2$, respectively. The laser pulses with 5-fs pulse duration and 8×10^{14} -W/cm² peak intensity at 0.8 μ m.

For the CEP measurement, two detectors are located in opposing directions along the polarization axis of the laser field. The idea is the following: For few-cycle pulses, the upward and downward field cannot not be approximated as symmetric. The same holds of course for vector potentials [dashed lines in Fig. 2.8(a) and (b)]. Thus, due to the asymmetric property of the field, if one measures the emitted photoelectron spectrum along the laser polarization axis in opposing directions, the CEP can be extracted by analysing the normalized difference in photoelectron spectra measured in two directions. This suggests a CEP-measurement technology, which will be detailed in the next chapters.

Fig. 2.8(e) and (f) show the final kinetic energy of on-axis emitted electrons for pulses with different CEPs. The blue lines are for electrons emitted downwards according to the direction of the vector potential and the red lines are for electrons emitted upwards. Following the convention in the literature, in the rest of this thesis, “up” and “down”

will be replaced by “left” and “right”, i.e., horizontal polarization will be implied. The rescattered electrons with up to $10U_p$ energy are generated where the waveform of the field is plotted in blue colors, see Fig. 2.8(a) and (b). Conversely, the direct electrons are generated in the yellow-line region. There the photoelectron energy is limited to $2U_p$, see Fig. 2.8(e) and (f). A few of examples of CEP-dependent ATI spectra of xenon measured in opposing directions are shown in Fig. 2.9. It can be seen that there is a big difference in the ATI spectra (in the logarithmic scale) measured by two detectors.

Chapter 3

Simulation Methods

In this chapter, we will introduce two theoretical methods we are using for the simulation. One is semi-classic model based on the three-step model we have discussed in the previous chapter. The other one is a numerical approach by solving the time-dependent Schrödinger equation.

3.1 Semi-classical Model (Classical Trajectory Monte-Carlo Simulations)

We first applied a so-called Monte-Carlo method in the semi-classic simulation based on the three-step model that we discussed in the previous chapter. The simulation process is as follows:

i) We calculate the ionization rate for all time of the field, $W_{ion}(t_i^k)$, and different trajectories, k , for electrons released from the ion at time, t_i^k .

ii) Using the momentum of returned electrons for all trajectories, $\mathbf{p}_r^{k,j}$:

$$\mathbf{p}_r^{k,j} = \mathbf{A}(t_r^{k,j}) - \mathbf{A}(t_i^k), \quad (3.1)$$

the momentum of rescattered electrons, $\mathbf{p}_{sc}(t_i^k, t_r^{k,j})$, can be obtained:

$$\mathbf{p}_{sc}(t_i^k, t_r^{k,j}) = -\mathbf{A}(t_r^{k,j}) + |\mathbf{p}_r^{k,j}|(\mathbf{e}_z \cos \theta_{res} + \mathbf{e}_y \sin \theta_{res}). \quad (3.2)$$

with the rescattering angle, θ_{res} .

iii) We apply the elastic differential scattering cross-section (DCS)¹, $\frac{d\sigma}{d\Omega}(\mathbf{p}_r, \theta_{res})$, to quantitatively describe the angle-dependent rescattering process. Many forms of poten-

¹Understanding of the DCS allows for extracting the structure information or imaging the electron

tials for calculating the DCS targeting different atoms or molecules can be found in Ref. [163–167]. We applied a widely-used atomic potential proposed by X.M. Tong and C.D. Lin [139], which has been proved to be a great model for rare gases [168–170].

$$V(r) = -\frac{Z}{r} - \frac{a_1 e^{-a_2 r} + a_3 r e^{-a_4 r}}{r}. \quad (3.3)$$

Fitting parameters a_1 to a_4 for different atoms can be found in Ref. [168, 171, 172].

iv) In order to obtain proper total scattering probability, one important effect, the wave packet spreading in space, needs to be considered. Here, we introduce a travel-time-dependent weight, W_{wps} , to further adjust the scattering probability:

$$W_{\text{wps}}(t_i^k, t_r^{k,j}) = (t_r^j - t_i^k)^{-\xi} \quad (3.4)$$

where ξ is a parameter describing how fast the wave packet spreads. We set $\xi = -3/2$. The reason is that the wave-packet starts spreading at ionization time, t_i^k , to return time, $t_r^{k,j}$, in three dimensions, which yields the number of 3. The Coulomb focusing effect due to the attraction force from the ion that contracts the wave-packet contributes the nominator number of 2 [173, 174].

By summing over all the results mentioned above, a two-dimensional photoelectron momentum distribution (PEMD) for rescattered electrons with a cylindrical symmetry around the linear laser polarization can be obtained:

$$W_{\text{sc}}(\mathbf{p}_{\text{sc}}) = \sum_{j,k} W_{\text{ion}}(t_i^k) \cdot \frac{d\sigma}{d\Omega}(\mathbf{p}_r, \theta_{\text{res}}) \cdot W_{\text{wps}}(t_i^k, t_r^{k,j}). \quad (3.5)$$

In order to obtain a better PEMD, there are a few other things need to be considered in the simulation, which will be discussed in the following sections.

3.1.1 Depletion in Ionizations

We can take the depletion of the ground state electrons into account, by solving the rate equation

$$dP(t)/dt = -\Gamma(t)P(t), \quad (3.6)$$

dynamics of atoms or molecules, which is known as the laser-induced electron diffraction (LIED) [49, 159–162].

where $P(t)$ is the population of the ground state electrons. With combining the ionization rate calculated using Eq. 2.8, the new ionization rate can be written as

$$W_{ion}(t_i^k) = \Gamma(t_i^k) \exp \left[- \int_{-\infty}^{t_i^k} \Gamma(t) dt \right]. \quad (3.7)$$

3.1.2 Perpendicular Momentum for Direct Electrons

So far, we assume that the initial momentum that parallel to the laser polarization after the tunnelling ionization is zero under the strong-field approximation. Considering a more realistic electron wavepacket distribution after the ionization process, we introduce an addition initial momentum term, p_{\perp} , which is perpendicular the polarization. The final momentum of direct electrons is given by

$$\mathbf{p}_{dir}(t_i, p_{\perp}) = -\mathbf{A}(t_i) + \mathbf{p}_{\perp}. \quad (3.8)$$

The perpendicular momentum distribution is assumed to simply follow by a Gaussian dependence [175], which has been proved to be a reasonable prediction [176, 177]

$$W_{per}(p_{\perp}^k) = \frac{4\pi\kappa}{|E(t_i^k)|} \exp \left(- \frac{\kappa \mathbf{p}_{\perp}^2}{|E(t_i^k)|} \right). \quad (3.9)$$

With considering this distribution, the final contribution of direct electrons is

$$W_{dir} = \sum_k W_{ion}(t_i^k) W_{per}(\mathbf{p}_{\perp}^k), \quad (3.10)$$

where all trajectories that lead to the same final momentum needs to be summed up.

At last, by adding the contribution of the direct electrons (Eq. 3.10) and rescattered electrons (Eq. 3.5), the final PEMD will be obtained [see Fig. 2.6(a) as an example]:

$$W_{PEMD} = W_{dir} + W_{sc}(\mathbf{p}_{sc}). \quad (3.11)$$

3.2 Time-dependent Schrödinger Equation (TDSE) Model

Solving the time-dependent Schrödinger equation (TDSE) is an effective approach to model the bound state dynamics, evolution of the electronic wave packet in the continuum and interactions with the Coulomb potential [16, 164, 178, 179], which allows us for direct

verification of experiments and prediction of new phenomena. In this section, we will briefly introduce the one-dimensional TDSE model that we applied.

The non-relativistic dynamics of an electron, which is bound by the Coulomb potential can be described by the time-dependent Schrödinger equation

$$i\frac{\partial}{\partial t}\Psi(x,t) = \hat{H}\Psi(x,t) = \left[-\frac{1}{2}\frac{\partial^2}{\partial x^2} + V(x)\right]\Psi(x,t) \quad (3.12)$$

where \hat{H} is the time-independent Hamiltonian, $\Psi(x,t)$ is the wave function of the electron and $V(x)$ is the binding potential.

A widely used form of describing the Coulomb potential in 1D is called the soft-core potential, i.e.,

$$V(x) = -\left(\frac{Z}{\sqrt{x^2 + a^2}}\right), \quad (3.13)$$

where Z and a are two parameters to remove the singularity at the origin and adjust the depth of the potential. Two parameters are selected according to the energy level of the atom. As we assume that the main photoelectron contribution is mainly from the ground state, we select the parameters by the value of the ionization potential of an atom, I_P . One can change Z and a accordingly for a fixed I_P to manipulate the height of the ATI plateau for a certain atom according to the measurements. Fig. 3.1(a) shows various potentials with different combinations of Z and a in atomic units while keeping the same I_P and Fig. 3.1(b) shows the corresponding ATI spectra calculated from various potentials in (a).

From the Fig. 3.1, we can see that the narrower the potential, the larger the yield of rescattering electrons (the higher the ATI plateau). This can be simply understood from a classic point of view, for a steeper potential, the returning process will experience with a larger force. Thus, more likely the rescattering will occur.

We applied a new 1D-potential recently invented by S. Majorosi et.al. [180]:

$$V(x) = -\frac{\frac{1}{2}Z}{|x| + a} \quad (3.14)$$

where Z is the effective charge and a is a free parameter for adjusting the energy level of the ground state. We pick this new 1D-potential as it has been proved to have a better quantitative agreement with a three-dimensional potential [180–182]. Of course, one can also adjust parameters in the soft-core potential such that the potential profile is identical to this new potential, as well as the desired ATI spectrum.

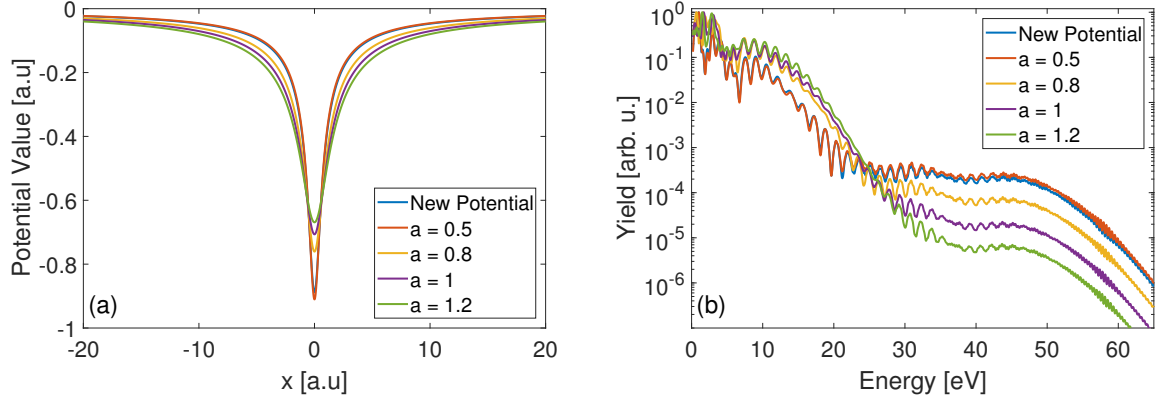


Figure 3.1: (a) Binding potentials with different combinations of Z and a but keeping the same ionization energy of ground state electrons in xenon (-12.13 eV). (b) CEP-averaged ATI spectra calculated from different potentials in (a) using 5-fs, $0.8\text{-}\mu\text{m}$ pulses at peak intensity of 0.8×10^{14} W/cm².

In order to calculate the interaction with the laser field, the external laser field needs to be included in the TDSE. With the dipole approximation, the new TDSE can be written as

$$i \frac{\partial}{\partial t} \Psi(x, t) = \left[-\frac{1}{2} \frac{\partial^2}{\partial x^2} + V(x) + V_{\text{ext}}(x, t) \right] \Psi(x, t), \quad (3.15)$$

with the laser field potential $V_{\text{ext}}(x, t) = x \cdot E(t)$. In our case, we apply a electric field with a Gaussian temporal profile:

$$E(t) = E_0 \exp \left\{ -2 \ln 2 \left(\frac{t}{\tau} \right)^2 \times [-i(\omega t + \phi)] \right\}, \quad (3.16)$$

where τ is the pulse duration, ω is the center frequency of the laser field and ϕ is the CEP of the pulse.

At the beginning of the calculation, we first substitute Δt by $-i\Delta t$. This is so-called imaginary time propagation [183]. After a few steps of imaginary time propagation, as the excited states damps faster than the ground states, the wavefunction converges to the ground states. Then, the real-time propagation of the wavepacket with the laser field begins. The evolution of the wavefunction is achieved by applying the split-step method [184], which split one time propagation step into two domains, a Cartesian space and a momentum space, to solve the Schrödinger equation easier in the program. After interacting with the laser field, the solution of the TDSE gives the new distribution of the

electron wave packet. Finally, by filtering out or projecting out contributions from the bound states [185], the photoelectron spectra can be obtained, examples see Fig. 3.1(b). More details about TDSE solver in Matlab can be found in Ref. [186, 187].

In general, the semi-classical model provides a good qualitative explanation and intuitive physical picture for describing the dynamics. Commonly it requires many approximations and simplifications. In contrast, the numerical solution of the TDSE can provide good modelling also of bound state dynamics of atoms or molecules, as well as the evolution of electron wave packet in the continuum.

The main challenge for TDSE calculations of light-matter interactions at long wavelength is computing power. As U_p increases with increasing laser wavelength, electrons acquire larger energy from the field. This leads to a larger wave packet distribution in both real space and momentum space. We used a split-step method that requires the wave function propagating in both domains. As the grid size in space is determined by the maxima value in momentum space due to underlying of the Fourier transform, not only a larger calculation range, but also a smaller sampling grid is required for both domains. In addition, long-wavelength pulses have longer pulse duration for the same number of optical cycles, requiring a longer propagation time with the field in the simulation. Thus, considering all these aspects, solving the TDSE for long wavelengths is quite demanding due to limited numerical power even for one dimension. Nevertheless, in this thesis, we present one-dimensional TDSE calculations for the comparison with experiments up to 3 μm wavelength.

Chapter 4

Laser Systems and Experimental Setup

The laser systems and the experimental setups, which were employed for this thesis will be presented and discussed in this chapter. The experiments using 0.8- μm and 1.8- μm laser pulses were performed in the laboratory of the chair of Nonlinear Optics at the Institute of Optics and Quantum Electronics of Friedrich-Schiller University Jena, Germany. The experiments using 3.2- μm pulses were performed with the MIR laser system of the ELI Attosecond Light Pulse Source (ELI-ALPS), Szeged, Hungary. Both systems and experimental setups will be introduced in the first half of this chapter. The rest of this chapter will discuss the core apparatus of this thesis for the measurement of the CEP, namely, the carrier-envelope phasemeter.

4.1 Laser Systems

4.1.1 IR and SWIR Laser System

The schematic of IR experiential setup is shown in Fig. 4.1. The laser system is based on a commercial mode-locked Ti:Sa laser oscillator (Femtopower Compact Pro HP/HR), which delivers sub-10 fs pulses at 77.9 MHz repetition rate with pulse energies in the nJ range. The pulses are then stretched in time to the ps level by passing them through a glass bock, amplified with a 9-pass amplifier and further compressed back to fs duration with a grating compressor. The process of pulse stretching, amplification, and re-compression is known as the chirped pulse amplification (CPA). During amplification, the repetition

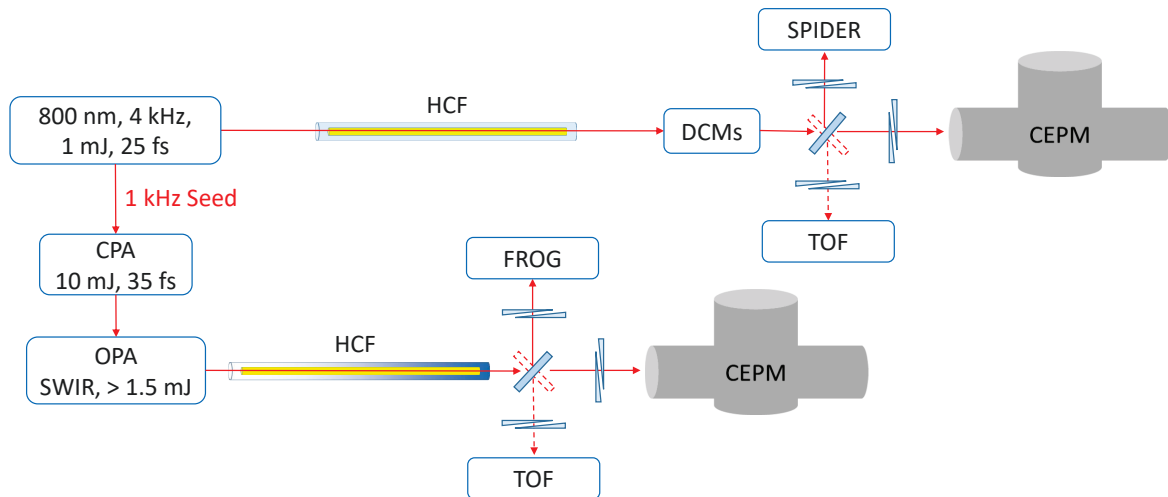


Figure 4.1: Schematic of the experimental setup. HCF: Hollow-core fiber. DCMs: Double-angle chirped mirrors. TOF: Time-of-flight spectrometer. FROG: Frequency-resolved optical gating. SPIDER: Spectral phase interferometry for direct electric-field reconstruction.

rate is reduced to 4 kHz by a Pockels cell. A commercial acousto-optic programmable dispersive filter system (DAZZLER, Fastlite) is applied to optimize the spectral phase. After the CPA system, the pulses have ≈ 1 -mJ energy and 25-fs duration. The center wavelength is around 780 nm. As few-cycle pulses cannot directly be generated by CPA because of spectral gain narrowing effect [188], additional post-compression is required.

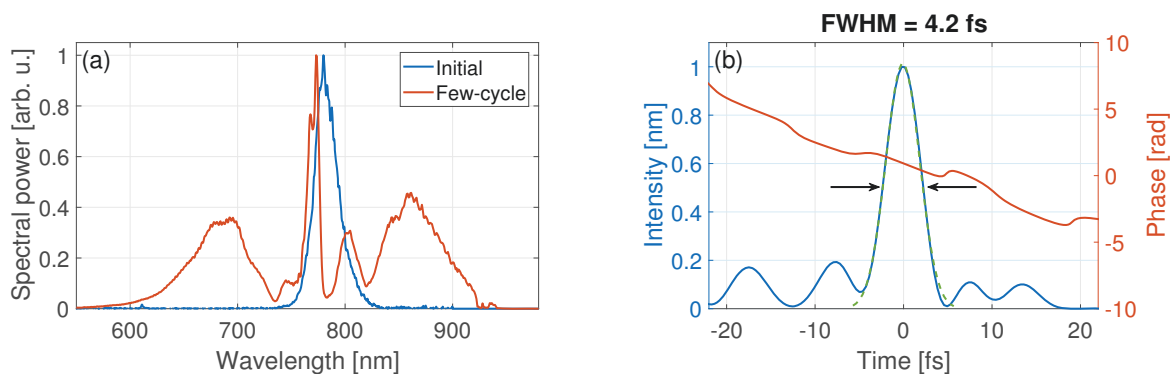


Figure 4.2: (a) Spectrum before and after the spectral broadening process. (b) One example of pulse duration measurement with a SPIDER device. The green curve is the Gaussian fit for the the main pulse.

In our case, 90% of the pulse energy are sent to a 1-m long argon-filled hollow-core fiber (HCF). The spectral bandwidth is broadened inside the fiber by self-phase modulation (SPM). After the fiber, double-angle chirped mirrors (DCMs) [189, 190] are applied to

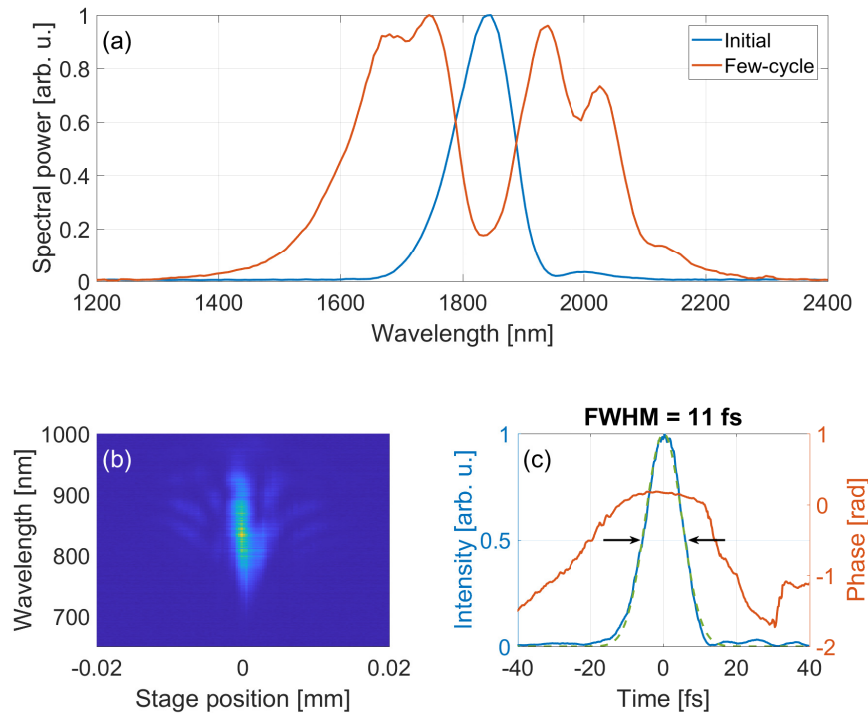


Figure 4.3: (a) Spectrum before and after the spectral broadening process. (b) One example of a FROG trace of few-cycle pulses at $1.8\ \mu\text{m}$. (c) The temporal pulse shape after a FROG phase retrieval process. The green dashed curve is the Gaussian fit.

compensate the positive group delay dispersion (GDD) caused by SPM and propagation through optics and air. In the literature, this post-compression technique is known as hollow-core fiber compressor (HFC) and currently the most common approach for pulse compression [191–193]. Fig. 4.2(a) shows the spectrum before and after the HCF. A pair of fused silica wedges is used to fine-tune the dispersion in order to get the shortest pulses, i.e., pulses close to the Fourier-transform limit (FTL), Pulses with duration of $< 5\ \text{fs}$ can be generated. The pulse length and the spectral phase of few-cycle pulses around $0.8\ \mu\text{m}$ are characterized by a commercial SPIDER (Spectral Phase Interferometry for Direct Electric-field Reconstruction) device [194–196]. Fig. 4.2(b) shows the temporal profile and the spectral phase of the shortest pulse we obtained – $4.2\ \text{fs}$ corresponding to 1.5 optical cycles at this wavelength.

In order to obtain multi-mJ pulses at $0.8\ \mu\text{m}$ or mJ-level SWIR pulses, the other 10% of the pulse energy are used to seed another CPA system (Thales company), which includes a 4-pass pre-amplifier and a 3-pass main amplifier. Again, a Pockels cell is used to reduce the repetition rate, in this case to $1\ \text{kHz}$, and another DAZZLER is applied to optimize

the spectral phase. The pulses, amplified to up to 10 mJ with a pulse duration of ~ 35 fs pump a commercial optical parametric amplifier (OPA) (HE-TOPAS, Light Conversion) to produce > 1 -mJ idler pulses in the range of $1.1 \mu\text{m}$ to $1.6 \mu\text{m}$ and > 1.5 -mJ signal pulses in the range of $1.7 \mu\text{m}$ to $2.2 \mu\text{m}$. A differentially pumped HCF is used to compress the SWIR pulses (e.g. $1.8 \mu\text{m}$) to the few-cycle regime.

Fig. 4.3(a) shows the spectra before and after the spectral broadening for $1.8 \mu\text{m}$ pulses. In the SWIR range, common optical materials like fused silica and air provide negative GDD, which can be used to compensate the positive GDD introduced by the SPM process. Thus, additional chirped mirrors are not required. A home-made FROG (Frequency-Resolved Optical Gating) device [197–199] is used to characterize the pulse length and the spectral phase of the SWIR few-cycle pulses. The FROG autocorrelation trace and the temporal profile of an 11-fs pulse (1.8 cycles) at $1.8 \mu\text{m}$ are shown in Figs. 4.3(b) and (c).

4.1.2 MIR Laser System

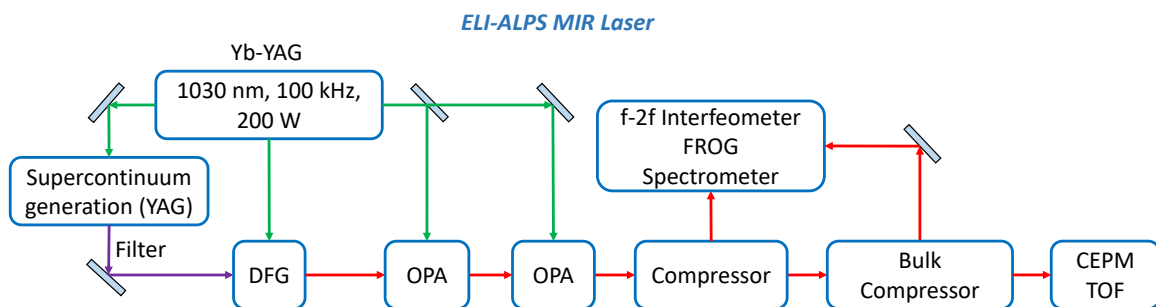


Figure 4.4: Schematic of the MIR laser system at ELI-ALPS, Szeged, Hungary and the experimental setup.

The experiments on few-cycle laser-matter interaction with MIR pulses were performed with the MIR laser facility at ELI-ALPS [200–202], Szeged, Hungary. It is a newly built and developed CEP-stable MIR laser system operating at 100-kHz repetition rate and can deliver 150- μJ , 40-fs MIR pulses and few-cycle pulses with up to 80 μJ . The schematic of the MIR laser system and the experimental setup are shown in Fig 4.4. The optical-parametric chirped-pulse amplification (OPCPA) system is pumped by a commercial Yb-YAG thin-disk regenerative amplifier laser system (Dira-200, Trumpf) which delivers 2-mJ, 100-kHz pulse trains at 1030 nm. A small fraction from the pump is focused into a

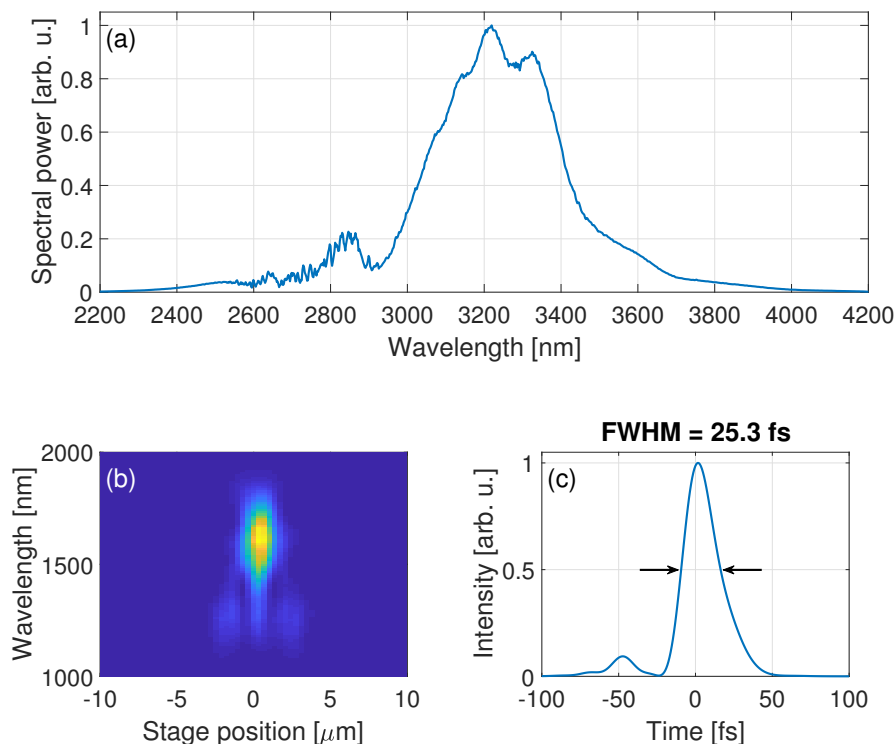


Figure 4.5: (a) Spectrum after the spectral broadening process. (b) FROG trace of 25.3-fs pulses at 3.2 μm . (c) The retrieved temporal pulse profile. The FWHM of the pulse duration is about 25.3 fs.

YAG crystal for supercontinuum generation. A DAZZLER is applied for spectral selection of the seed into the difference frequency generation (DFG) stage. The seed beam is mixed with a part of the pump beam in a nonlinear crystal thus generating the MIR idler beam at 3.2 μm . The MIR pulses are further amplified with two additional OPA systems. As the laser wavelength is in the MIR range, silicon with positive group velocity dispersion (GVD) and CaF_2 with negative GVD are used to tune the dispersion. The output power after the bulk compressor is ~ 15 W with a pulse duration of 40 fs. The pulse duration is measured by a commercial FROG (Fastlite) device. An f - $2f$ interferometer provides the feedback for stabilizing the CEP.

The 100-kHz OPCPA system delivers 50-fs compressed pulses, the FTL being 43 fs [20]. For post-compression / spectral broadening, instead of a gas-filled HFC, bulk crystals [109, 202, 203] are used as medium for spectral broadening due to the absorption in noble gases at MIR wavelengths. In our case, an average power of 11 W was focused into an uncoated 2-mm thick YAG crystal at Brewster's angle by a $f = 500$ -mm spherical mirror.

Material	GVD [fs ² /mm]	TOD [fs ³ /mm]
YAG	-466.39	2972.3
Si	485.17	866.76
CaF ₂	-133.23	763.79
BaF ₂	-64.07	399.95

Table 4.1: Table of the group velocity dispersion (GVD) and the third-order dispersion(TOD) of different materials.

As YAG has a negative GVD at 3.2 μm , no further optical elements are required for compensating the positive GDD. This is known as “self-compression”. After the bulk compression stage, CaF₂ and BaF₂ plates with negative GVD and Si plates with positive GVD are used for fine tuning the dispersion in order to have the shortest pulses inside the vacuum chamber where light-matter interaction takes place.

Many strategies for dispersion compensation have been tested and a pair of BaF₂ wedges with a total thickness up to 10 mm were inserted in the beam path for further fine-tuning the dispersion. One disadvantage of Si is its low transmission at this wavelength. However, materials with positive GVD and high transmission are rare in the MIR. Table 4.1 shows the dispersion of materials we used for the compression of MIR pulses to the few-cycle regime. As all materials that were available during the beam time have positive third-order dispersion, a compression close to the FTL was challenging. Recently, scientists in ELI-ALPS have improved the post-compression system such that pulses below 20 fs can be obtained around 3.1 μm wavelength [204, 205].

The broadened spectrum after post-compression is shown in Fig. 4.5(a). The pulse length of compressed pulses is characterized by a commercial FROG device. Fig. 4.5(b) displays the SHG-FROG trace of the shortest pulses (~ 25 fs) we achieved during the beam time. The corresponding retrieved temporal profile of the pulses is shown in Fig. 4.5(c).

4.2 Carrier-envelope Phasemeter (CEPM)

For few-cycle pulses, the envelope of the pulse varies almost as fast as the electromagnetic field. As laser-matter interactions depend on the time variation of the field, the CEP is a crucial parameter for analyzing field-dependent phenomena. Thus, the detection

or control of the phase becomes a crucial point for virtually all applications of few-cycle pulses. In this thesis, we will present a robust technique of CEP measurement based on the measurement of photoelectron emission in opposing directions along the laser polarization axis, the carrier-envelope phasemeter (CEPM).

The first CEP-dependent ATI spectra of xenon were measured in 2003 [206]. Based on these measurements, the CEPM was invented. The instrument uses only the high-energy plateau electrons because of their pronounced asymmetric distribution and eventually reached single-shot operation [30]. Further improvements of the control of the TOF spectrometer, electronics, and algorithms enabled the CEPM to measure the CEP in real-time with high-resolution for each single laser shot at kilo-Hertz repetition rates [31].

The schematic of the CEPM is shown in Fig. 4.6(a). Few-cycle pulses are focused into the high-vacuum chamber and ionize the target atoms injected from a nozzle. Two micro-channel plate (MCP) detectors mounted on two sides along the laser polarization axis detect generated photoelectrons from the target and their arriving time to the detector. Thus, each detector is a time-of-flight (TOF) spectrometer. A static repelling voltage is applied in front of the MCPs to block the low-energy (slow) electrons which are only weakly CEP-dependent. Thus, only strongly CEP-dependent high-energy photoelectrons are detected. Using the knowledge of the phasemeter geometry, one can convert the time-dependent photoelectron current into an energy-dependent yield. An example of measured single-shot photoelectron spectra $S_{\text{left}}(E)$ and $S_{\text{right}}(E)$ from both detectors of a CEPM is given in Fig. 4.6(b).

The energy- and CEP-dependence of the ATI spectra is commonly quantified by defining their (energy-dependent) asymmetry A :

$$A(E) = [S_{\text{left}}(E) - S_{\text{right}}(E)] / [S_{\text{left}}(E) + S_{\text{right}}(E)]. \quad (4.1)$$

For the CEPM, in order to extract the CEP information from the single-shot ATI spectra $S_{\text{left}}(E)$ and $S_{\text{right}}(E)$, two energy regions are chosen, the low-energy and the high-energy part of the ATI plateau, see Fig. 4.6(b). Integration of $S_{\text{left}}(E)$ and $S_{\text{right}}(E)$ over the low- and high-energy interval yields four quantities:

$$Y_{\text{left,low}} = \int_{G_1}^{G_2} S_{\text{left}}(E) dE, \quad Y_{\text{left,high}} = \int_{G_3}^{G_4} S_{\text{left}}(E) dE, \quad (4.2)$$

$$Y_{\text{right,low}} = \int_{G_1}^{G_2} S_{\text{right}}(E) dE, \quad Y_{\text{right,high}} = \int_{G_3}^{G_4} S_{\text{right}}(E) dE, \quad (4.3)$$

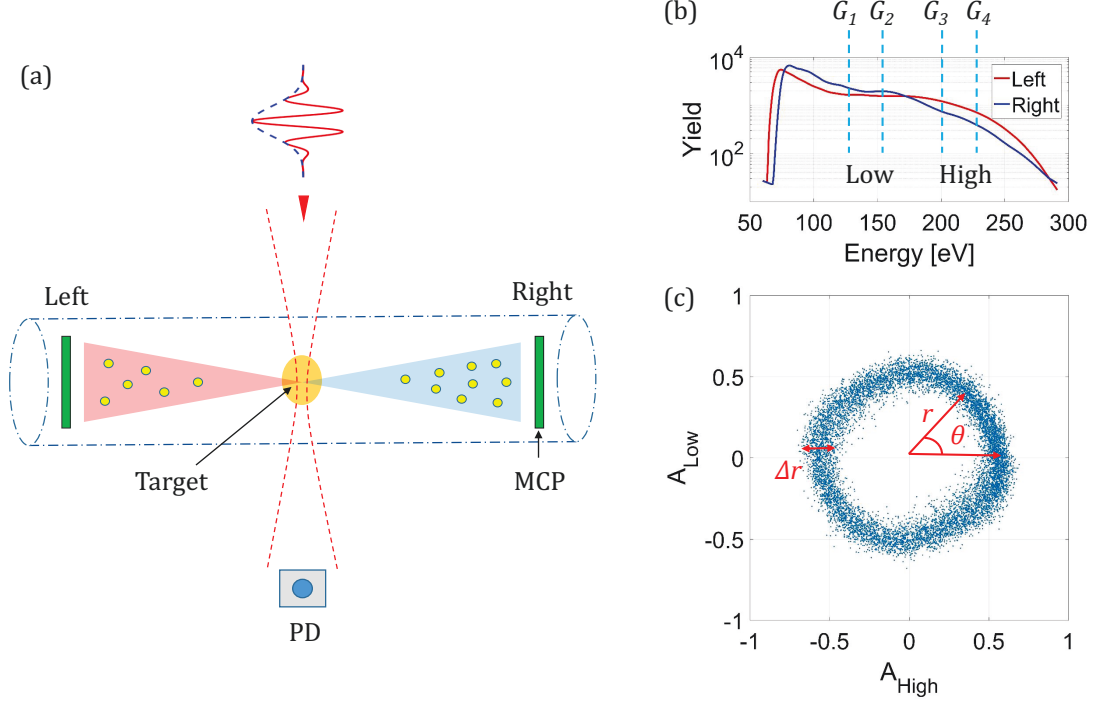


Figure 4.6: Schematic of the working principle of the CEPM. (a) Schematic of a CEPM. The photoelectron current is measured by micro-channel plate (MCP) detectors. The photodiode (PD) detector provides the trigger signal for the measurement of the time-dependent photoelectron current. A pair of slits is mounted to confine the interaction volume such that the electrons created outside the laser focus are blocked. (b) An example of high-energy photoelectron spectra measured by both sides of the MCP for one laser shot. (c) An example of the parametric asymmetry plot (PAP) obtained from the ATI spectra for 20 000 consecutive laser shots.

where G_1 , G_2 , G_3 , and G_4 denote the energy boundaries of the selected regions.

Next, we define the asymmetry parameters for the two energy regions in the same way as in Eq. 4.1, i.e. by taking the normalized difference between the left yield and the right yield:

$$A_{\text{low}} = \frac{Y_{\text{left,low}} - Y_{\text{right,low}}}{Y_{\text{left,low}} + Y_{\text{right,low}}}, \quad A_{\text{high}} = \frac{Y_{\text{left,high}} - Y_{\text{right,high}}}{Y_{\text{left,high}} + Y_{\text{right,high}}}. \quad (4.4)$$

These two CEP-dependent asymmetries parameters can approximately be regarded as a sinusoidal function of the CEP,

$$A_{\text{low}} \approx A_0 \sin(\phi + \phi_0), \quad A_{\text{high}} \approx A'_0 \sin(\phi + \phi_0 + \phi_i), \quad (4.5)$$

where A_0 and A'_0 are the asymmetry amplitudes for two energy regions, ϕ is the CEP, ϕ_0 is an arbitrary but fixed offset phase, and ϕ_i is the relative phase between two energy regions.

A so-called parametric asymmetry plot (PAP) is obtained by plotting the two asymmetries, A_{high} and A_{low} , as x - and y -coordinates for every single laser shot. Each point of the PAP corresponds to one laser shot. Its polar angle, θ , in the PAP has a one-to-one correspondence to the CEP, ϕ . An example of the PAP for 13-fs (2.1 cycles) pulses at $1.8\ \mu\text{m}$ with 20 thousand of consecutive laser shots is shown in Fig. 4.6(c).

When the PAP is a circle, the distribution is uniform in θ with a constant radius r . In this case, θ has a linear relation with ϕ and the precision of the CEP measurement is independent of θ . In order to obtain a circle in the PAP, the two energy regions need to be selected such that the two sinusoidal functions A_{low} and A_{high} have a phase shift of $\pi/2$. The boundaries, G_1 , G_2 , G_3 , and G_4 , are further optimized to minimize the standard deviation Δr divided by the radius r , as the precision of the CEP measurement, $\Delta\phi$, is dominated by the statistical error in the measurement. It can approximately be determined by $\Delta\phi \approx \Delta\theta \approx \Delta r/r$ [31]. This can be verified by inserting statistical jitters in the simulation based on a Monte-Carlo algorithm (details see in Section 5.4).

When the pulse length is close to a single cycle, the current on one detector may vanish, while the current on the other MCP is at its maximum. Then, the asymmetries $A(\phi)$ can no longer be approximated by a sine function, but develop a top-hat profile. Accordingly, the circular distribution in the PAP turns into a square. In this case, the CEP should be evaluated by adding a density weight parameter for a general distribution, ξ :

$$\Delta\phi = \frac{\rho(\theta)}{\bar{\rho}} \Delta\theta = \xi(\theta) \Delta\theta, \quad (4.6)$$

where ρ is the angle-dependent density of laser shots. The relation between ϕ and θ is obtained by integration over the angle:

$$\phi(\theta) = \phi_0 + \int_0^\theta \xi(\theta') d\theta'. \quad (4.7)$$

One specific quality of the CEPM is its ability to characterize the pulse duration of few-cycle pulses simultaneously with the phase measurement. In the PAP, the radius of the distribution, r , in Fig. 4.6(c), corresponds to the asymmetry amplitude, A_0 and A'_0 , see Eq. 4.5. As the pulse length τ is decreased, the CEP-dependence in the ATI spectra increases and so does the asymmetry and thus the radius of the PAP ($r \approx A_0$). Although

this measurement cannot directly provide spectral phase information on few-cycle pulses, a general phase behaviour can roughly be estimated by finding the largest PAP radius, r , while optimizing the dispersion.

This is supported by the following observation: When a fused silica wedge pair is used to fine-tune the spectral phase, often more than one local maximum of the PAP radius can be observed. This indicates that different higher orders of dispersion are balanced at different wedge positions. One example of multiple maxima of the PAP when the dispersion is not well balanced is shown in Fig. 4.7. When the dispersion is well compensated and the pulse duration is very close to the FTL, only one maximum of the PAP can be observed. Thus, one can indeed use the PAP distribution to optimize the spectral phase in a general way. In summary, the shorter the pulse, the larger the radius. Therefore, simultaneously with the CEP measurement, the CEPM also allows for an accurate pulse duration characterization of few-cycle pulses, which is rather difficult to be accurately measured by conventional means, especially under single-shot operation.

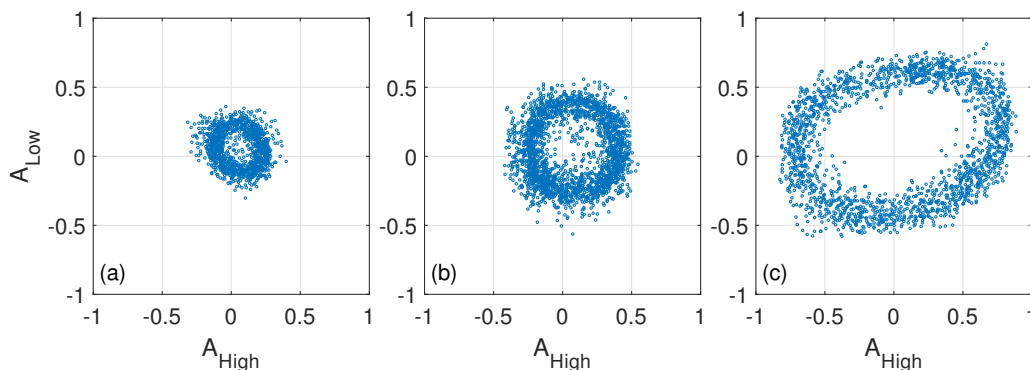


Figure 4.7: Examples of multiple localized maxima of the PAP at different wedge positions when the dispersion is not well balanced, e.g., three maxima of the PAP displayed in (a), (b) and (c).

Chapter 5

CEP Measurements at 1.8 μm and Simulation Results

In this chapter, the single-shot measurement of the CEP at 1.8 μm will be presented and compared with simulations. By analysing the simulated results and the comparisons, the requirements for a single-shot CEPM and the precision of the CEP measurement will be discussed.

5.1 Scaling Strong-field Interactions with Wavelengths

Increasing the driving laser wavelength is interesting in attosecond physics and strong-field physics in several respects. The direct consequence of increasing the wavelength is that the ponderomotive energy, U_p , will grow with wavelength, $U_p \sim I\lambda^2$, where I is the laser intensity and λ is the center wavelength of the laser field. One important consequence for applications is the increase of the cut-off energy of high-harmonic spectrum, $I_P + 3.17U_p$ [145], where I_P is the ionization potential. Besides higher photon energy also the bandwidth in the extreme ultraviolet increases. Thus, shorter attosecond pulses can be obtained [36]. Similarly, pulses with longer wavelengths and thus higher U_p lead to photoelectron momentum distributions (PEMD) extending over a larger range of momenta. Therefore, structures in the PEMDs are enlarged. In a certain sense, longer wavelengths work as a magnifying glass for the investigation of electronic and molecular dynamics, spatially and temporally. Examples are the holographic structure [156–158], the low-energy structure (LES) [42, 43], imaging with electrons [49], molecular dynamics [207], and the

study of strong-field fragmentation of molecules or ions [208, 209].

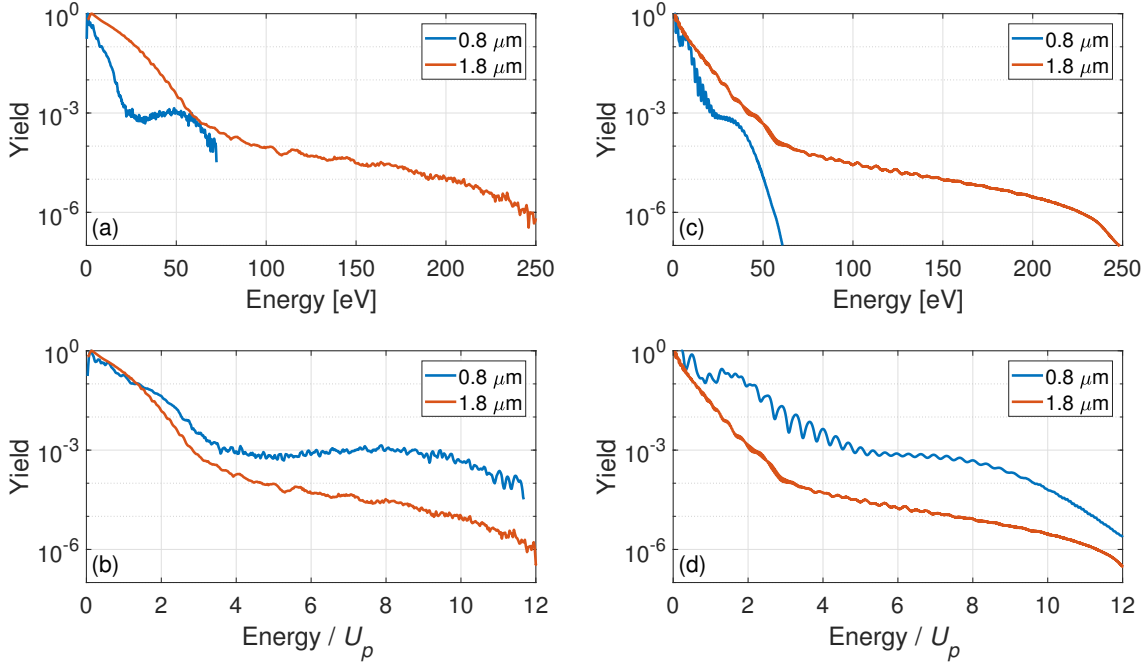


Figure 5.1: (a), (b) Measured CEP-averaged ATI spectra of xenon at 0.8 μm and 1.8 μm with peak intensities of $\sim 0.8 \times 10^{14} \text{ W/cm}^2$ in units of the absolute energy and the ponderomotive energy, U_p , respectively. (c), (d) Simulated CEP-averaged ATI spectra of xenon at 0.8 μm and 1.8 μm calculated from the TDSE simulation with a peak intensity of $0.8 \times 10^{14} \text{ W/cm}^2$ in units of the absolute energy and U_p , respectively.

Although the CEPM technique has been developed for more than a decade since its invention [206], it has largely remained confined to wavelengths below 1 μm for the reason that the CEPM becomes challenging for longer wavelengths because of a dramatic reduction in the yield of high-energy ATI plateau electrons that are utilized for the CEP measurement. There are several reasons for this effect. The first one is that longer travel times due to longer wavelengths lead to stronger wave packet spreading, which reduces the return current density [12, 64]. As the ATI spectrum is measured along the laser polarization axis, the rescattering probability scales as $\sim \lambda^{-2}$ due to the spreading effect in transverse dimension. Second, larger kinetic energies E_{kin} of the photoelectrons due to the increased ponderomotive energy U_p cause a reduction in rescattering probability. The classic differential cross-section for rescattering is approximately proportional to E_{kin}^{-2} . If we look at the total rescattering yield which requires an integration over the energy axis, therefore, the total rescattering yield is proportional to $E_{\text{kin}} \sim U_p \sim \lambda^2$. Together with

the wave packet spreading effect, the total rescattering probability scales as λ^{-4} .

If one looks at the ATI yield plotted against an absolute energy scale (rather than measured in units of U_p), one finds that the total decrease of rescattering probability scales as λ^{-4} [48]. In this case, one factor of λ^{-2} is still from wave packet spreading. The other factor of λ^{-2} is due to the electron yield being distributed over a larger energy region because the electron energy scales with U_p . This is how scaling of HHG or ATI are usually discussed in the literature [48, 210]. However, this should be criticized because the birth time and return time of electrons that end up with the same energy are both different when the laser wavelengths is changed. Accordingly, in this thesis, the discussion of the scaling will always assume U_p as the energy scale.

Fig. 5.1(a) shows the CEP-averaged ATI spectra of xenon at 1.8 μm and 0.8 μm wavelength, measured by a high-resolution time-of-flight (TOF) photoelectron spectrometer. The ratio of the integrated yield in the plateau region for 0.8 μm and 1.8 μm is about 0.04, which roughly agrees with our estimation of scaling. The numerical solution of the time-dependent Schrödinger equation (TDSE) also shows that the rescattering yield scales as $\sim \lambda^{-5 \pm 0.5}$. An example is shown in Fig. 5.1(b) and (d).

5.2 CEP Measurements at 1.8 μm

The experimental setup is shown in Fig. 4.1. In order to obtain few-cycle pulses around 1.8 μm center wavelength, 1.5-mJ, 60-fs idler pulses from the OPA system are focused into a 1-m long Argon-filled differentially pumped hollow-core fiber for nonlinear spectral broadening. By changing the gas pressure inside the fiber, the bandwidth of the pulses was tuned. Together with adjusting the thickness of the glass wedges in the beam path accordingly, nearly Fourier transform-limited pulses of different pulse lengths were generated. Independent pairs of fused silica wedges were used to adjust the shortest and thus approximately the same pulse length in the FROG device and the CEPM. For the CEP measurement, few-cycle pulses were focused by a $f = 200$ mm lens into the CEPM. The pulse energy in the CEPM was ~ 300 μJ , corresponding to a peak intensity of $(0.8 \pm 0.1) \times 10^{14}$ W/cm^2 , as estimated by the highest energy of electrons measured by the detector.

Fig. 5.2(a) shows pulse duration (FWHM) for few-cycle laser pulses at 1.8 μm mea-

sured by the FROG instrument at different pressures together with the corresponding mean radius of the PAP measured by the CEP. The pulse length measurement (red dots) is compared to the FTL of the pulse length (green dots), which is calculated from the measured spectra. Examples of the PAPs for different pulse lengths are shown in Fig. 5.2(b). As we can see, the asymmetry amplitude for the high-energy region is slightly larger than the one for the low-energy region, as the high-energy part of the ATI plateau is more sensitive to the CEP. Thus, the PAPs are stretched a little bit horizontally. When the pulse is shorter than 2 cycles, the asymmetry increases for all electron energies and the round shape of the PAPs turns into a square shape. For pulses with only one optical cycle, the PAP will adapt to the four edges of the graph, since $A = 1$ is the maximum asymmetry.

At low pressures (< 0.4 bar), the pulses cannot be compressed to the Fourier transform-limit (FTL) because the pulses have a large negative group delay dispersion (GDD) after the OPA and fused silica also has negative GDD around 1.8 μm . Accordingly, the CEP measurement is not possible in this pressure range due to the long pulse durations. Starting from 0.4 bar, there is enough positive GDD from self-phase modulation and the pulses can be compressed to the few-cycle regime. The pulse lengths are actually close to the FTL. For higher pressures, the GDD can still approximately be compensated with the wedges. At pressures larger than 1.2 bar, due to the introduction of additional higher-order dispersion terms from the nonlinear interaction and ionization, the spectral phase cannot be compensated by transmission through the wedges only. Thus, the pulses have a larger deviation from the FTL and impede a reasonable measurement by our home-made FROG. However, as strong-field ionization is a highly nonlinear phenomenon that strongly depends on the field strength, the pre- or post-pulses due to unbalanced dispersion or fluctuations have much less impact in the CEP than in the FROG. Thus, a larger mean radius of the PAP can still be measured, which indicates a shorter pulse duration of the main pulse. In our case, the shortest pulses obtained were close to 10 fs (< 2 optical cycles at 1.8 μm).

In Fig. 5.2(c), the blue square dots show the mean radius of the PAP at 1.1 bar Argon pressure in the fiber with different thicknesses of the wedges in the beam path. Here, the thickness of the wedges is defined as 0 for the shortest pulse, i.e., the largest radius of the PAP. Negative thickness of wedges means less glass in the beam path leading to

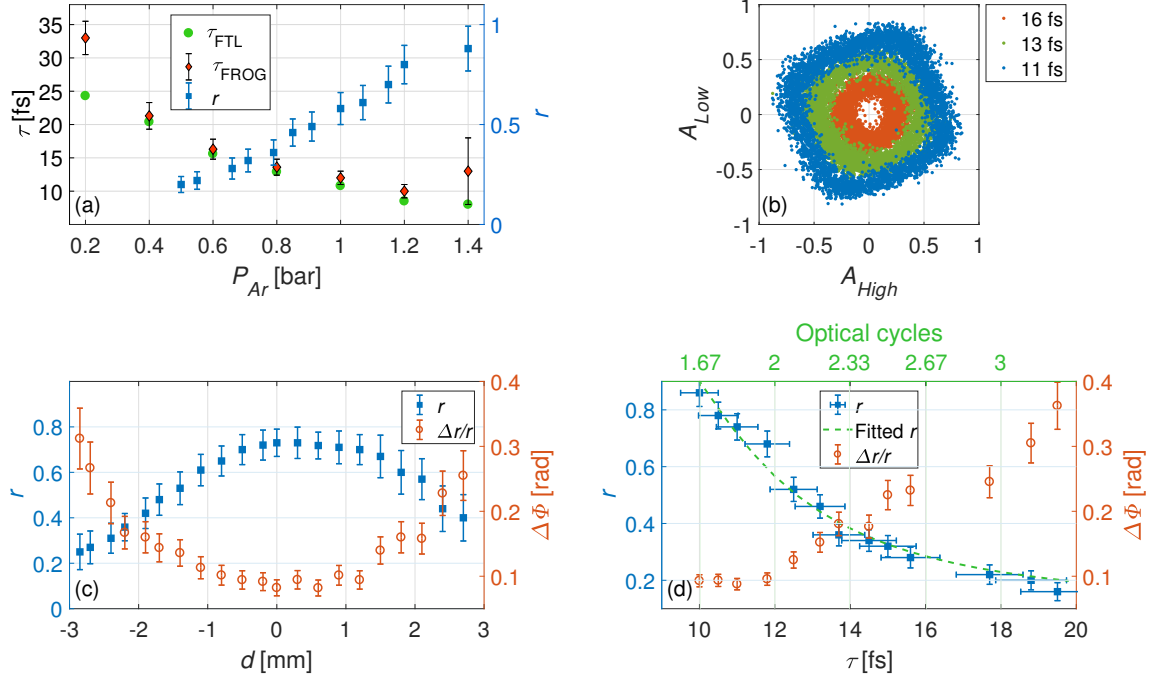


Figure 5.2: (a) The pulse length, τ , measurement by a FROG device, the FTL of the pulse length calculated from the spectrum, and corresponding PAP radius obtained from a CEPM, r , at different pressures in the fiber. (b) PAPs at pressures of 0.65, 0.90, and 1.20 bar, corresponding to 16 ± 0.5 , 13 ± 0.5 , and 10 ± 0.5 -fs pulses at $1.8 \mu\text{m}$, respectively. For each pressure, 5000 consecutive laser shots are plotted here. (c) The PAP measurement with 11-fs pulses at different thicknesses of the wedges in the beam path. The mean radius of the PAP (blue squares) and the corresponding precision of the CEP measurement (red dots). (d) The mean radius of the PAP and the corresponding precisions of the CEP measurement, $\Delta\phi \sim \Delta r/r$, for different pulse lengths. The relation between the radius, r , and the number of optical cycles, N_T , is fitted with the function $r = 1.14 - \exp[-\alpha/(N_T - \beta)^2]$, with fitting parameters $\alpha = 0.6532$, and $\beta = 1.006$ (dashed curve).

positively chirped pulses and vice versa. As we can see, due to the chirp introduced by the more or less glass in the beam, the pulse lengths increase. During the scan of glass thickness, there is only one maximum for the radius, which indicates that the spectral phase at this gas pressure is well-balanced. Otherwise, multiple local smaller maxima of the radius would be observed, see Fig. 4.7. For each CEP measurement at different gas pressure, the pulse length is optimized as outlined above.

As discussed in Section 4.2, one specific quality of the CEPM is that the pulse length can be determined by the radius of the PAP distributions. The mean radii of the PAP at different pulse lengths are shown in Fig. 5.2(d) and characteristic instants of the PAP distribution at three pulse lengths are shown in Fig. 5.2(b).

Although the ionization yield can be quite different for different ionization processes, the left-right asymmetry amplitude mainly depends on the asymmetry of the electric field which can be represented by the number of optical cycles. Thus, we apply a simple fitting function to describe the mean radius of the PAP, r , as a function of the number of optical cycles, N_T , such that one can roughly characterize the pulse duration at any wavelengths:

$$r = 1.14 - \exp\left[-\frac{\alpha}{(N_T - \beta)^2}\right], \quad (5.1)$$

where α and β are two fitting parameters.

The explanation of this function is as follows: as the ionization yield is mainly coming from the peak of the field for each half optical cycle, the asymmetry is mainly caused by the difference of the peak value of the field for the next half cycle. For a cosine pulse with a Gaussian envelope, if the value of the peak of the field is $E(t = 0) = E_0$, the field at next half cycle is

$$E(t = T_0/2) = E_0 \exp\left[-\left(\frac{T_0/2}{\tau}\right)^2\right] = E_0 \exp\left[-\left(\frac{T_0/2}{N_T T_0}\right)^2\right] = E_0 \exp\left[-\left(\frac{0.5}{N_T}\right)^2\right], \quad (5.2)$$

where T_0 is one optical cycle and τ is the pulse duration. If we assume that the asymmetry depends on the peak value of the electric field to some power, the asymmetry is approximated to follow as $1 - \exp(-\frac{\alpha}{N_T^2})$.

Additionally, for a better fit to the data, we modified two things in the function: i) an offset β is introduced in the denominator. β can be considered as the minimum pulse length required to produce rescattering electrons in full energy range. From another point of view, this quantity indicates the condition for achieving the maximum PAP. According

to the measurements, $\beta = 1.006$, reflects the limiting case that the pulses has only one optical cycle, which fulfils our estimation of this parameter; ii) The constant term (the maximum value) of this function is modified from 1 to 1.14. It is because when the pulses are shorter than 2 cycles, the round PAP becomes square. The limiting case is when the pulse is extremely short such that the PAP distributions adapts to the four edges of the PAP square. In this case, the maximum of the mean radius is reached. For a square with a side length of 2, the mean radius is 1.14.

Although the CEP can vary from shot to shot, the pulse duration remains more or less constant. Thus, the mean radius of the PAP distribution can indeed afford a highly robust pulse duration measurement for few-cycle pulses at any wavelengths.

In addition to the pulse duration, also the precision of the CEP measurement can be retrieved from the PAP. The general relationship between the PAP distribution and the variation of the CEP is given in Eq. 4.7. As discussed in Section 4.2, the precision is dominated by the statistics, i.e., $\Delta\phi \sim \Delta\theta \sim \Delta r/r$. Thus, by dividing the standard deviation in the PAP [see Fig. 4.6(c)], Δr , by the mean radius of the PAP, r , one can determine the precision of the CEP measurement, see red dots in Fig. 5.2(c) and (d). The shorter the pulse, the larger the PAP and the higher the precision. Taking the 11-fs pulse as an example, the standard deviation Δr is ~ 0.07 while the mean radius r is ~ 0.55 . Thus, the precision of the CEP is ~ 120 mrad ($\sim 8^\circ$).

Single-shot capability for measuring the CEP allows for the measurement of CEP-dependent phenomena in any other experiment, even if the CEP varies randomly from shot to shot. To this end, each event of the phenomenon under investigation is labelled (“tagged”) with the CEP measured by a CEP-M. The CEP-tagging measurement serves as a strong proof of the validity of our CEP measurement with a CEP-M.

In the following, this is demonstrated on ATI itself. An independent high-resolution TOF photoelectron spectrometer was used to measure the CEP dependence of the photoelectron emission of xenon. The experimental setup is shown in Fig. 4.1. The few-cycle pulses were split by a 50/50 beam splitter. Half of the beam was sent to the CEP-M and the other half of the beam was sent to the TOF spectrometer. Both, the high-resolution spectrometer and the CEP-M, measure the same thing. However, the former has a five times longer flight tube and a four times higher temporal resolution. In addition, the target gas pressure is 3 orders of magnitude smaller as compared to the situation in

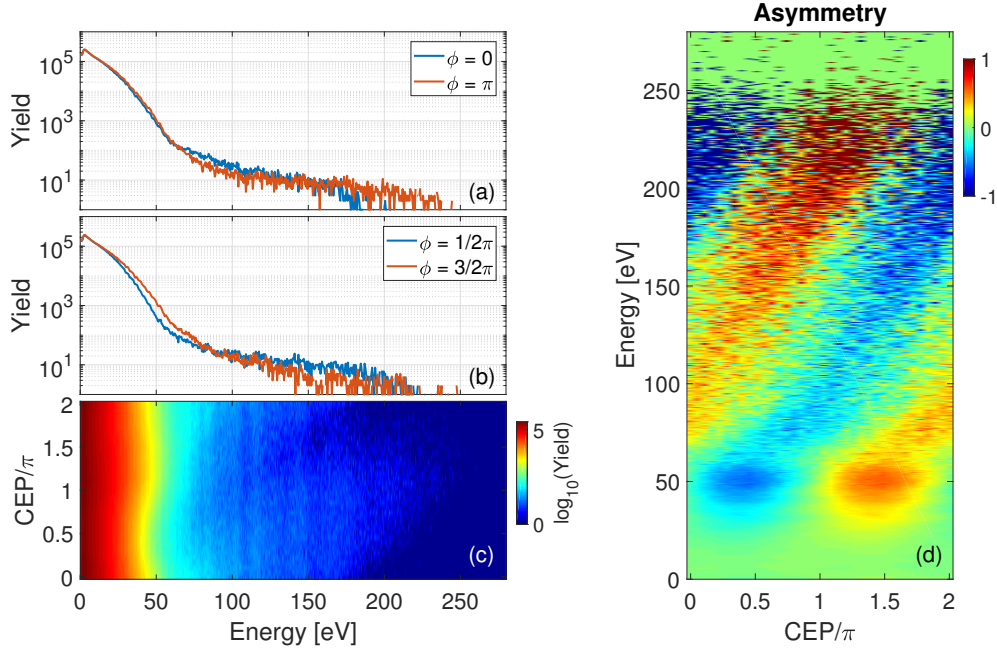


Figure 5.3: (a), (b) ATI spectra of xenon at 1.8 μm with different CEPs measured by a high-resolution TOF photoelectron spectrometer. (c) False-color plot of the CEP- and energy-dependent ATI yield. (d) False-color plot of the CEP- and energy-dependent asymmetry measured by CEP-tagging. The pulse duration in this measurement was 13 ± 0.5 fs and the peak intensity $\sim (0.8 \pm 0.1) \times 10^{14}$ W/cm².

the CEPM. Therefore, this spectrometer is well-suited for high-resolution photoelectron spectroscopy, but obviously not for single-shot phase measurement.

Figs. 5.3(a) and (b) show examples of the ATI spectra of xenon with different CEPs measured by the TOF spectrometer and the corresponding CEP-dependent yield is shown in Figs. 5.3(c). By numerically shifting the measured spectra by a phase of π , the left-right asymmetry can be calculated, see Fig. 5.3(d). The $10U_p$ cutoff of the ATI spectra is around 225 eV, corresponding to a peak intensity 0.75×10^{14} W/cm². A strong CEP-dependence of the spectra starts to appear near the $2U_p$ cutoff for direct electrons around 50 eV. It reflects the phase-dependence of the $2U_p$ cutoff [211].

5.3 Simulation Results and Comparison to Experimental Results

In this section, the simulation results from a semi-classic model and 1D-TDSE calculations are presented and compared to the measurements. The agreement validate the CEP measurements at $1.8 \mu\text{m}$ and our theoretical interpretation.

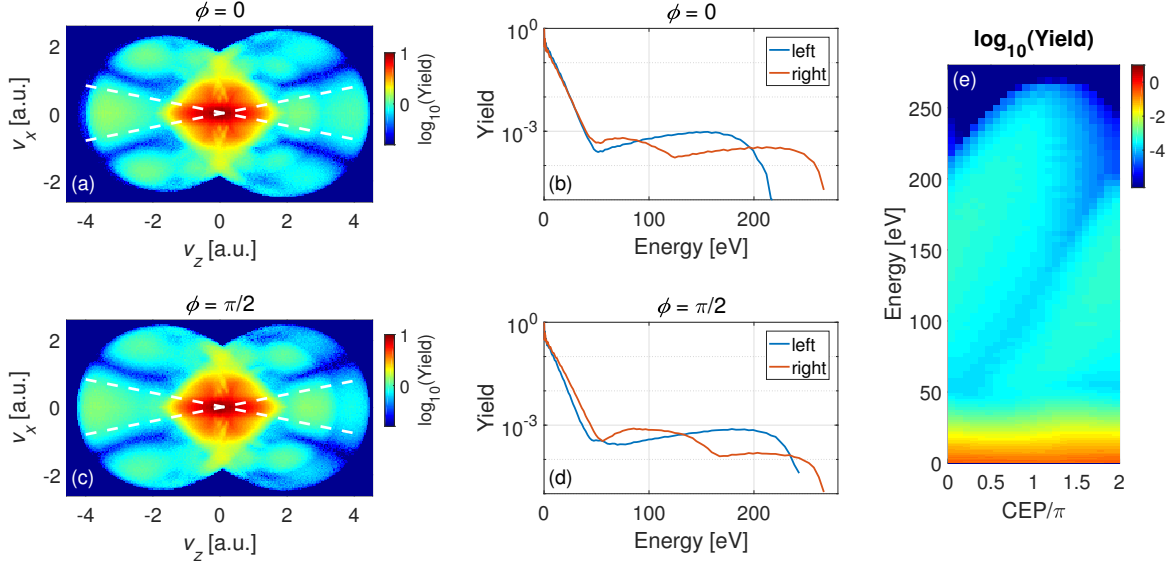


Figure 5.4: (a), (c) Photoelectron momentum distribution (PEMD) parallel to the polarization axis of the laser with different CEPs calculated from the semi-classic model. The pulse duration used here is 13 fs and the peak intensity is $0.8 \times 10^{14} \text{ W/cm}^2$. (b), (d) The ATI spectra obtained from the PEMD (a) and (c) by integration of the yield within a region with a cone angle of 5° , which corresponds to the emission angle to the detector. (e) CEP- and energy-dependent yield in logarithmical scale for the left side.

Based on the three-step model discussed in Section. 3.1, we first compute the two-dimensional photoelectron momentum distributions (PEMDs) with cylindrical symmetry around the polarization axis. Figs. 5.4(a) and (c) show the PEMDs for different CEPs of 13-fs pulses at a peak intensity of $0.8 \times 10^{14} \text{ W/cm}^2$. The intensity-volume effect, namely the fact, that the target atoms experience different intensities in the interaction volume of a focused laser beam, has been included here. More details will follow in the next chapter. For the TOF spectrometer, only the electron emission within a small cone around the laser polarization axis can reach to the detector. Thus, in order to obtain ATI spectra similar to the experimental conditions, the yield within a 5° cone of the PEMD

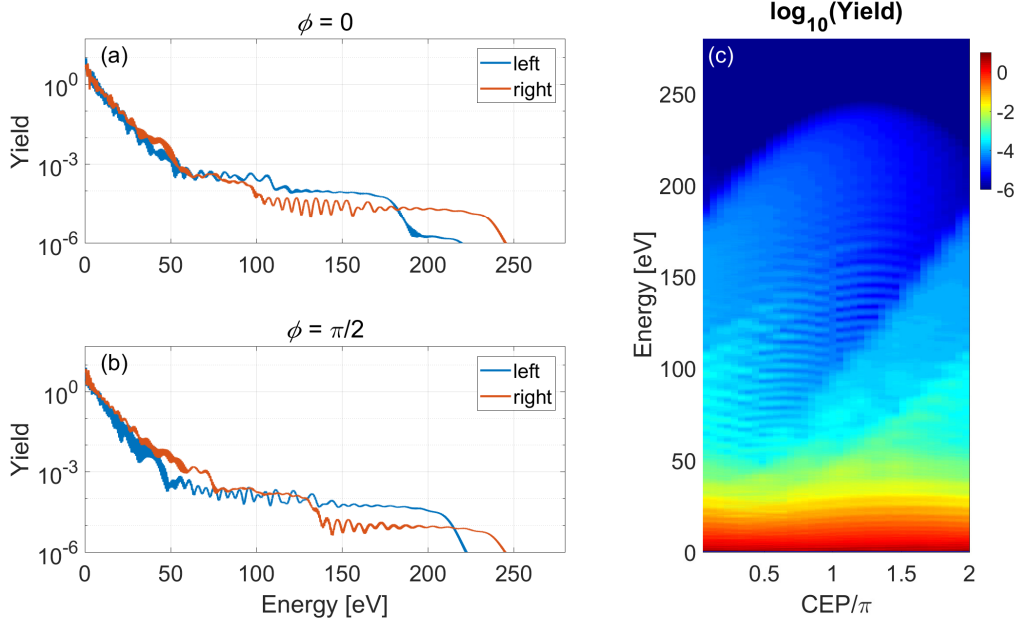


Figure 5.5: (a), (b) ATI spectra of xenon at $1.8\ \mu\text{m}$ with different CEPs obtained from the 1D TDSE calculation. The peak intensity is $0.8 \times 10^{14}\ \text{W}/\text{cm}^2$ and the pulse duration is 13 fs. (c) CEP- and energy-dependent yield in false colors for the left-hand detector (logarithmic color map).

is integrated and converted into energy spectra, see Figs. 5.4(b) and (d). The negative and positive momentum parts in the PEMD correspond to the left- and right-hand ATI spectra, respectively. For one side, the CEP- and energy-dependent yield for the left side is shown in Fig. 5.4(e). Additionally, the ATI spectra of xenon at the same conditions calculated from the 1D-TDSE are shown in Fig. 5.5(a) and (b). The corresponding energy- and CEP-dependent yield in false colors is shown in Fig. 5.5(c).

Next, we compare the simulated asymmetry map and the corresponding PAPs with the measurements, shown in Fig. 5.6. Two energy regions are selected and integrated, analogous to the procedure for the CEPM, e.g., the regions within the dashed and solid lines in Fig. 5.6(a). The asymmetries for both energy regions and the corresponding PAPs obtained from these two regions are compared in Figs. 5.6(b), (e) and (h) and Figs. 5.6(c), (f) and (i), respectively. The criteria for selecting energy regions for the experiments can be found in Section 4.2. The energy regions in the simulations are chosen to be same as the experiments.

From Figs. 5.6(b), (e), and (h), it can be seen that the asymmetry amplitude for high-

energy regions is slightly larger than that for low energy regions, resulting in a small ellipticity in the PAP distribution. It is because for high-energy electrons, particularly those near the cutoff, correspond mainly to ionization close to the center peak of the pulse. Thus, they are more sensitive to the asymmetry of the field. In general, despite some details in the simulated ATI spectra differing from the measurements due to the approximations or simplifications applied in the models, the trend of the energy-dependence and the-CEP dependence in the simulated asymmetry agree very well with the measurements.

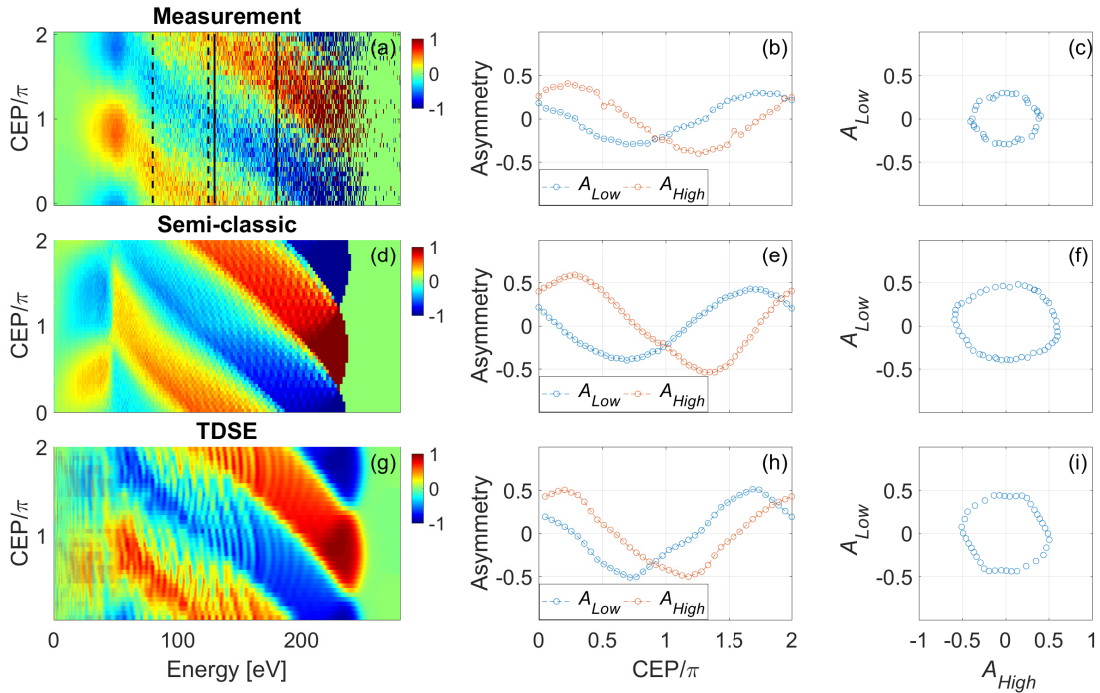


Figure 5.6: (a) Measured CEP- and energy-dependent asymmetry for 13 ± 0.5 -fs pulses with peak intensity of $(0.9 \pm 0.1) \times 10^{14}$ W/cm². (b), (c) CEP-dependent asymmetries of two energy regions for plotting the PAP from (a) and the corresponding PAP. (d) CEP- and energy-dependent asymmetry calculated from the semi-classic model with 13-fs pulses and peak intensity of 0.8×10^{14} W/cm². (e), (f) CEP-dependent asymmetries of two energy regions for plotting the PAP from (d) and the corresponding PAP. (g) CEP- and energy-dependent asymmetry calculated from the TDSE with 13-fs pulses and peak intensity of 0.8×10^{14} W/cm². (h), (i) CEP-dependent asymmetries of two energy regions for plotting the PAP from (g) and the corresponding PAP.

However, there is also noticeable disagreement: No matter which energy region is considered, the calculated asymmetry amplitude is always larger than the measured one

resulting in larger PAPs than the measured one, shown in Fig. 5.6. In other words, the simulations always predict larger CEP-dependence or shorter pulses than in reality. This could cause misinterpretations of measured data, in particular with respect of their use for estimating the pulse duration. It turns out that the discrepancy roots in the spatial phase distribution in a focused beam, which has not been considered in the theoretical analysis so far. The spatial phase distribution leads to an averaging effect for the CEP-dependence of the ATI spectra, which we refer to as the “focal-phase effect” and will discuss it in detail in the next chapter.

5.4 Discussions

5.4.1 Single-shot Requirement

In order to achieve the single-shot CEP measurement with a CEPM, the key question is how many electrons need to be detected per laser shot. A Monte-carlo algorithm was applied in the simulation to address this question. Specifically, a certain amount of random numbers which simulates limited amount of electrons arriving at the detector, are generated in the simulation. These random numbers follows the distribution of the ATI spectrum. By applying this method on the ATI spectrum from pulse to pulse virtually, we investigate the statistical condition for the single-shot CEP-measurement.

Figs. 5.7(a) - (d) represents the ATI spectra particularly in the plateau region for one pulse constructed by 10 000, 2 000, 500 and 200 random numbers which can be assumed as the number of electrons detected by a CEPM per laser shot. The corresponding asymmetry maps and the PAP distributions are shown in Figs. 5.7(e) - (h) and Figs. 5.7(i) - (l), respectively. It can be seen that the more virtual electrons in the plateau region, the better the statistics and the better the analysis.

From the single-shot PAP trace [Figs. 5.7(i) - (l)], the precision of the CEP measurement can be calculated, e.g., 50 mrad, 150 mrad, 250 mrad, and 500 mrad for 10 000, 2 000, 500 and 200 electrons in the ATI plateau region, respectively. When the number of plateau electrons is less than 200, the excessive statistical noise impedes generating a reasonable PAP. With 500 electrons in the plateau region, a reasonable PAP can be obtained but still with a rather low precision. A relatively high precision of the CEP measurement, e.g., ~ 150 mrad, which is similar to our experimental result, demands 2000 plateau electrons.

And of course, the more electrons in the ATI spectra, the better the statistics, and the thinner the PAP distribution and the higher the precision of the CEP measurement. If one further increases this number to extremely large, the ATI spectra will converge to the theoretical outcome and the PAP will converge to a single line of an approximate circle as in Fig. 5.6.

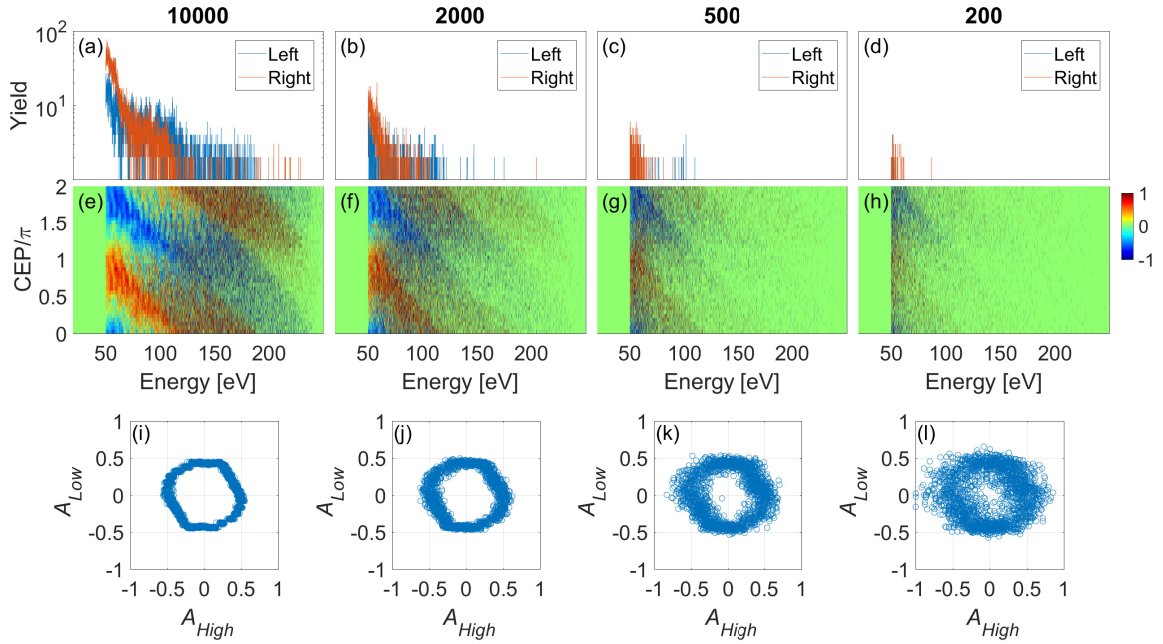


Figure 5.7: Simulation of the statistics in the ATI spectra. (a) - (d) Single-shot ATI spectra with 10 000, 2 000, 500 and 200 virtual electrons in the plateau region. (e) - (h) The corresponding simulated asymmetry maps and (i) - (l) the corresponding PAP distributions with randomly CEPs.

As mentioned in the beginning of this chapter, the main challenge for the single-shot CEP measurement with a CEPM at long wavelengths is the low rescattering yield which approximately scales as $\sim \lambda^{-4}$. The most straightforward solution is to increase the pulse energy by a factor of λ^4 . However, the pulse energy in reality is commonly limited by the laser systems.

In our experiment, we applied $\sim 300\text{-}\mu\text{J}$, $1.8\text{-}\mu\text{m}$ pulses to the CEPM, which is more than 10 times larger energy than that at $0.8\text{ }\mu\text{m}$. This compensates the loss of the rescattering electrons to a great extent [approximately to a factor of $(\frac{1.8}{0.8})^3$]. The openings for the photoelectrons in the gas cell have been reduced in size in order to allow a higher target gas density at a given pump speed, which compensate at least another factor of

λ^1 . Note that this is important because too much pressure in the CEPM is a risk for the detectors. In addition, the total number of ionized electrons will be increased for longer wavelength pulses due to longer pulse durations. After several iterations, we have achieved a similar experimental condition and similar precision of the single-shot CEP measurement at SWIR wavelengths.

5.4.2 Intensity Impact

A common question for the CEPM is how the intensity affects the measurement. Normally, the CEPM is operated with a peak intensity below the barrier-suppression intensity of the target. If the intensity is too low, the ionization yield will dramatically decline such that not enough ionized electrons will be detected. If the intensity is too high, saturation occurs, namely, the electric field at the leading edge of the pulse is already strong enough for ionization and the electrons are depleted for the rest of the pulse. This will lead to an ambiguity in both phase and pulse length measurement. If the intensity is far beyond the BSI, high-order CEP effect may occur. This will be discussed in Chapter 7 in detail.

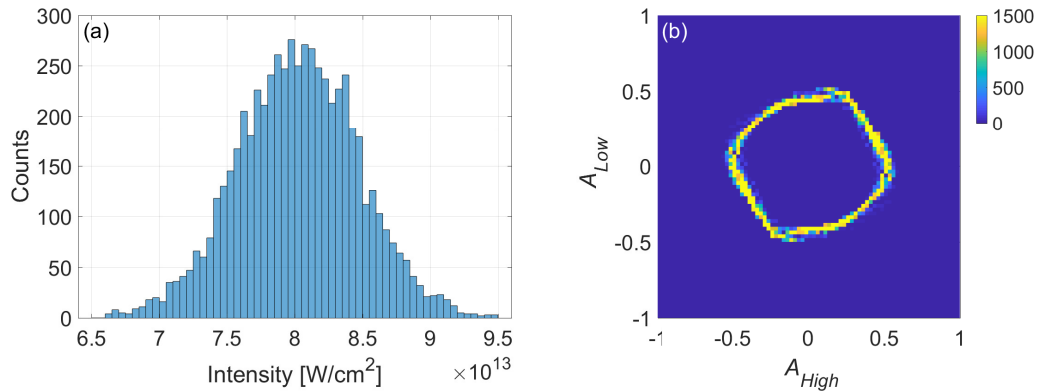


Figure 5.8: (a) Histogram of simulated intensity fluctuations with a Gaussian distribution. There are 10 000 laser shots and the coefficient of variation of the distribution is 10%. (b) The corresponding PAP distribution in a density map.

In order to investigate the intensity impact on the phase measurement, we apply similar strategy of analysis as above. We assume that the power fluctuation of a laser system follows approximately a Gaussian distribution and the center of the distribution is the intensity at which we performed our experiments. A certain number of laser shots with different energies is randomly distributed in a Gaussian function. Fig. 5.8(a) shows an

example of an intensity histogram with a coefficient of variation¹ of 10% and Fig. 5.8(b) shows the corresponding PAP distribution. For such an intensity distribution, the resulting standard deviation of the distribution in the PAP is only ~ 0.03 , which is much less than the impact from the statistical noise due to the limited number of detected electrons. Thus, the precision of the CEP measurement, as well as the pulse length measurement are not affected by the intensity fluctuations. However, the accuracy of the CEP measurement may reduce as the intensity fluctuations will cause a phase uncertainty [212]. In general, the better the stability of the laser system, more precise and more accurate characterization of the CEP can be realized. Typical commercial systems including ours have power fluctuations of less than 5%, so we assume that the intensity impact is rather small.

¹Coefficient of variation (CV): the ratio of the standard deviation to the mean.

Chapter 6

Phase-volume Effect in Few-cycle Light-matter Interactions

As shown in the previous chapter (see Fig. 5.6), the calculated asymmetry amplitude, which characterizes the CEP dependence, is consistently larger than found in experiments. The main reason is the phase shift in the focus, known as the Gouy phase, which leads to an equally large CEP shift. In the same way as a measured ATI spectrum has contributions from atoms “seeing” different intensities in the focus (the intensity-volume effect), the spectrum also has contributions from different CEPs. So far, this has not been considered in our theoretical analysis. As this spatially dependent phase distribution is coupled to the intensity distribution, the targets (e.g. atoms or molecules) inside the focal volume experience different laser intensities and CEPs, depending on their locations.

The intensity distribution in the focus leads to an averaging effect for intensity-dependent phenomena, the so-called “intensity-volume effect” [213], which has been considered in the previous chapters. Likewise, for phenomena induced by few-cycle pulses, the CEP-dependence will be partially averaged out due to the spatial phase distribution. We refer to this as “phase-volume effect”. In this chapter, we will demonstrate the significance of the phase-volume effect and quantify it for a broad range of few-cycle light-matter interactions.

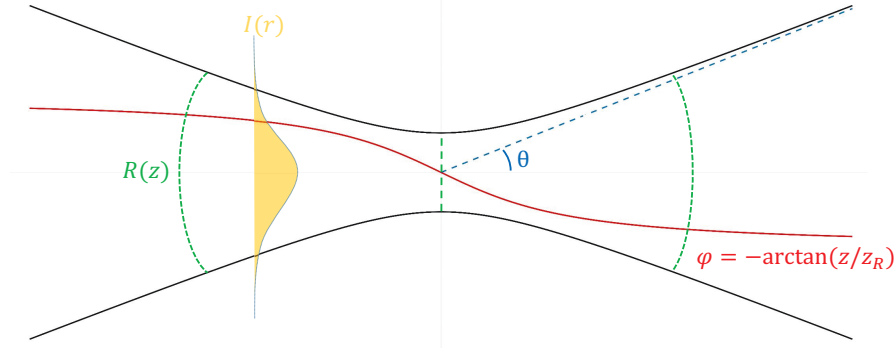


Figure 6.1: Schematic of a Gaussian beam

6.1 The Gaussian Beam and the Gouy Phase

In the following sections, we will mainly discuss the volume effect of a Gaussian beam. Using the Ansatz of the electric field, $E = E_0 u(x, y, z) e^{-ikz}$, with a envelope $u(x, y, z)$, in the wave equation, $\nabla^2 E + k^2 E = 0$, yields:

$$\partial_x^2 u + \partial_y^2 u + \partial_z^2 u - 2ik\partial_z u = 0. \quad (6.1)$$

Under the paraxial approximation [214], i.e., $\partial_z^2 u \gg \partial_z u$, the wave equation can be written as:

$$\partial_x^2 u + \partial_y^2 u - 2ik\partial_z u = 0. \quad (6.2)$$

and the solution of Eq. 6.2 is the well-known Gaussian beam:

$$E(x, y, z) = E_0 \frac{w_0}{w(z)} \cdot e^{-\frac{x^2+y^2}{w(z)^2}} \cdot e^{ik\frac{x^2+y^2}{2R(z)}} \cdot e^{i[kz - \arctan(z/z_R)]}, \quad (6.3)$$

where w_0 is the beam waist, $z_R = \pi w_0^2/\lambda$ is the Rayleigh range, $w(z) = w_0 \sqrt{1 + z^2/z_R^2}$ is the z -dependent beam size, $R(z) = z + z_R^2/z$ is the z -dependent radius of curvature of the wave fronts. The first two terms in Eq. 6.3 describe the evolution of the transverse field distribution. The corresponding transverse intensity distribution in radial coordinate is:

$$I(r, z) = \frac{c\varepsilon_0}{2} |E(r, z)|^2 = I_0 \cdot \left[\frac{w_0}{w(z)} \right]^2 \cdot e^{-2\frac{r^2}{w(z)^2}}, \quad (6.4)$$

with $I_0 = c\varepsilon_0 |E_0|^2/2$ being the peak intensity in the center of the focus. The divergence angle, which represents the characteristics of a Gaussian beam, can be estimated from the far-field

$$\vartheta \sim \frac{w(z)}{z} \sim \frac{w_0}{z_R} = \frac{\lambda}{\pi w_0}. \quad (6.5)$$

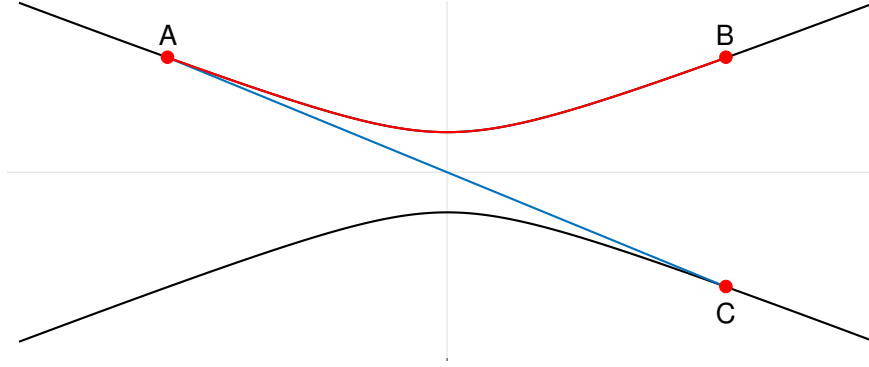


Figure 6.2: Schematic of an intuitive explanation of the Gouy phase.

The last two terms in Eq. 6.3 describe the spatial phase of a Gaussian beam. The term with $R(z)$ is the spherical phase of the wavefront and the last term, $\varphi = -\arctan(z/z_R)$, is the additional axial phase shift caused by focusing, the well-known Gouy phase. It was first observed and investigated by Gouy [215, 216] at the end of the 19th century. An intuitive physical explanation of the existence of the Gouy phase can be found in the geometrical properties of a Gaussian beam [217]. The off-axis rays of a focused beam propagate along a curved path because of diffraction. A characteristic example is the margin ray, \widehat{AB} in Fig. 6.2. The curved path \widehat{AB} is shorter than plane wave propagation along a straight line \overline{AC} . Thus, the accumulated phase variation from A to B should be smaller than from A to C . However, points B and C belong to the plane with the same phase front, which implies that the local phase velocity of a curved path is faster than the phase velocity of a plane wave. An alternative interpretation is a local increase of the wavelength in focus.

The physical origin of the Gouy phase can be interpreted as a consequence of the uncertainty principle [218]:

$$\Delta k_x \Delta x \geq \text{Constant}, \quad (6.6)$$

which states that a finite beam diameter Δx inevitably leads to diffraction, i.e. leads to a distribution for the transverse components of the wave vector, \vec{k} , with a width, Δk_x . Since $k = \sqrt{k_x^2 + k_y^2 + k_z^2}$ is constant along the beam, k_x and k_y increase at the expense of k_z – in contrast to an infinite plane wave where $k = k_z$. This leads to the same conclusion as in the preceding paragraph, namely a local increase of the wavelength in focus. With the definition of an effective axial propagation constant: $\bar{k}_z \equiv \frac{\langle k_z^2 \rangle}{k} = k - \frac{\langle k_x^2 \rangle}{k} - \frac{\langle k_y^2 \rangle}{k}$, the expectation values of the transverse momenta directly yield the evolution of the axial

phase shift of a focused beam – the Gouy phase, ϕ_G :

$$\phi_G = -\frac{1}{k} \int^z \langle k_x^2 \rangle + \langle k_y^2 \rangle dz = -\frac{2}{k} \int^z \frac{1}{w(z)} dz. \quad (6.7)$$

The Gouy phase shift leads to important consequences in many fields of optics. In laser physics, the Gouy phase affects the resonant frequencies of the cavity [219–221]. Due to the physical underlying of atomic response, it determines the phase matching conditions for nonlinear generation of radiation, in particular also high-order harmonic generation (HHG) [222, 223], quasi-phase matching in HHG [224, 225] and THz wave generation [226–228]. Based on the analysis of the phase shift, it can also be used to improve the imaging quality [229, 230]. The crucial point for us is that the phase shift is coupled to the CEP and thus affects phase-dependent light-matter interactions [111, 231, 232].

6.2 The Pulsed Beam and the Focal Phase

The aforementioned axial phase shift (Gouy phase) is derived for monochromatic beams. However, virtually all CEP-dependent effects become observable only when the pulse duration consists of a few optical cycles. From another perspective, the bandwidth of few-cycle pulse is so broad that only considering the monochromatic phase shift is insufficient. Considering a pulse with the Ansatz $E = E_0 u(x, y, z, t) \exp[i\omega_0(t - z/c)]$, where ω_0 is the carrier frequency and c is the speed of light, the wave equation can be written as:

$$\nabla^2 u - 2i \frac{\omega_0}{c} \frac{\partial u}{\partial z} - 2i \frac{\omega_0}{c^2} \frac{\partial u}{\partial t} - \frac{1}{c^2} \frac{\partial^2 u}{\partial t^2} = 0. \quad (6.8)$$

Introducing a variable, $t' = (t - z/c)/\tau$, Eq. 6.8 under the paraxial approximation can be written as:

$$\frac{\partial^2 u}{\partial x^2} + \frac{\partial^2 u}{\partial y^2} - 2ik_0 \frac{\partial u}{\partial z} - \frac{2}{c} \frac{\partial^2 u}{\partial z \partial t'} = 0. \quad (6.9)$$

In order to show the influence of the pulse length, a dimensionless variable, $\tau' = t'/T$ is introduced in Eq. 6.9 and yields

$$\frac{\partial^2 u}{\partial x^2} + \frac{\partial^2 u}{\partial y^2} - 2ik_0 \frac{\partial u}{\partial z} + \frac{k_0 T_0}{\pi T} \frac{\partial}{\partial z} \frac{\partial u}{\partial \tau'} = 0, \quad (6.10)$$

where T is the pulse duration and T_0 is one optical cycle. For $T_0/T \ll 1$, as the pulse duration is much longer than the oscillation period, the last term of Eq. 6.10 can be neglected. In this case, the beam is approximated as a monochromatic beam. Accordingly,

when the pulse duration is so short, e.g. few-cycle pulses, ($T_0/T \lesssim 1$), the mixed derivative term, $\frac{\partial}{\partial z} \frac{\partial u}{\partial \tau}$, cannot be neglected.

In order to obtain the solution of this spatial and temporal coupling of the short pulsed beam, the common way is to treat the pulse propagation in the frequency domain [233–235]. Thus, the temporal profile of the electric field can be obtained by the inverse Fourier transformation of the spectrum $E(r, z, \omega)$:

$$E(r, z, t) = \frac{1}{2\pi} \int E(r, z, \omega) e^{-i\omega t} d\omega, \quad (6.11)$$

For few-cycle pulsed beams, the temporal electric field for the center frequency can be written as

$$E(r, z, t) = A(r, z, t) e^{-i[\omega_0 t - \varphi_{\omega_0}(r, z) - \phi]}, \quad (6.12)$$

where $A(x, y, z, t)$ is the complex envelope and ϕ is the CEP. Thus, the spatially and temporally modulated envelope is [110]

$$A(r, z, t) = \frac{1}{2\pi} \int_{-\infty}^{\infty} A_{\omega}(x, y, z) e^{-i[(\omega - \omega_0)t - \varphi_{\omega}(r, z) + \varphi_{\omega_0}(r, z) + \phi]}. \quad (6.13)$$

Explicit analysis of the evolution of the amplitude and the phase can be realized by applying the Taylor expansion around the center frequency for both parameters:

$$A_{\omega}(r, z) \simeq A_{\omega_0}(r, z) + A'_{\omega_0}(r, z) + \frac{1}{2} A''_{\omega_0}(r, z) + \dots; \quad (6.14)$$

$$\varphi_{\omega}(r, z) \simeq \varphi_{\omega_0}(r, z) + \varphi'_{\omega_0}(r, z)(\omega - \omega_0) + \frac{1}{2} \varphi''_{\omega_0}(r, z)(\omega - \omega_0)^2 + \dots. \quad (6.15)$$

In Eq. 6.15, the first and second phase term on the right side link to the phase velocity $v_p(r, z) = \omega_0/|\nabla\varphi_{\omega_0}(r, z)|$ and the group velocity $v_g(r, z) = 1/|\nabla\varphi'_{\omega_0}(r, z)|$, respectively. If one insert Eq. 6.14 and 6.15 into Eq. 6.13, a general description for few-cycle beams can be obtained. M. A. Porras derived and analyzed the CEP shifts for different conditions with different orders of approximation of the phase and the amplitude [110].

As a characteristic example, consider a Gaussian few-cycle beam with a phase dominated by the first-order dispersion. In this situation, the first-order approximation of the phase would be taken into account, see Eq. 6.15. The terms, $\omega_0 t - \varphi_{\omega_0}(r)$, represent the phase front and the term, $\varphi'_{\omega_0}(r, z)$, represents the pulse front which can be regarded as the instant time at which the pulse arrives [216]. Thus, the CEP shift of a pulse is

$$\phi(r, z) = \phi + \varphi_{\omega_0}(r, z) + \omega_0 \varphi'_{\omega_0}(r, z). \quad (6.16)$$

Using the equation for the phase front of a Gaussian beam,

$$\omega_0 t - \frac{\omega_0}{c} z + \arctan \frac{z}{z_{R0}} - \frac{\omega_0 r^2}{2cR_{\omega_0}(z)}, \quad (6.17)$$

with, z_{R0} , the Rayleigh length for the center frequency, ω_0 , the first derivative of the phase at the ω_0 can be calculated:

$$\phi'_{\omega_0}(r, z) = \frac{z}{c} + \frac{z}{\omega_0 z_{R0}} \frac{w_0^2}{w_{\omega_0}^2(z)} + \frac{r^2}{2cR_{\omega_0}(z)} \left(z - \frac{z_{R0}}{z} \right). \quad (6.18)$$

where w_{ω_0} is beam waist for the center frequency ω_0 . Insert the phase front (Eq. 6.17) and the pulse front (Eq. 6.18) into Eq. 6.16, the CEP of a Gaussian can be obtained

$$\phi(r, z) = \phi - \arctan\left(\frac{z}{z_{R0}}\right) + \frac{1 - \frac{2r^2}{w_{\omega_0}(z)^2}}{\frac{z}{z_{R0}} + \frac{z_{R0}}{z}}. \quad (6.19)$$

Based on the propagation of the Gaussian beam using the q -parameter, M. A. Porras further improved this formulation of the CEP distribution by considering the frequency-dependent input beam waist [236]:

$$\phi(r, z) = \phi - \arctan\left(\frac{z}{z_{R0}}\right) + g_0 \frac{1 - \frac{2r^2}{w_{\omega_0}(z)^2}}{\frac{z}{z_{R0}} + \frac{z_{R0}}{z}}, \quad (6.20)$$

with a dimensionless factor g_0 , to which we refer as the ‘‘Porras factor’’:

$$g_0 = \left. \frac{dZ_R(\omega)}{d\omega} \right|_{\omega_0} \frac{\omega_0}{Z_R(\omega_0)}. \quad (6.21)$$

where $Z_R(\omega) = \omega W(\omega)^2/2c$ is the frequency-dependent Rayleigh range of the collimated input beam before the focussing optics and $W(\omega)$ is the frequency-dependent input waist¹.

The g_0 -factor represents the geometric characteristics of the input beam, i.e. the spectral diameter and the spectral divergence. When $g_0 = 0$, the last term in Eq. 6.20 is 0, which indicates that all frequencies have a constant Rayleigh length Z_R , corresponding to the monochromatic approximation (Gouy phase). For $g_0 = -1$, the input beam has a frequency-independent divergence resulting in a frequency-independent focal waist. For $g_0 = 1$, the input beam has a frequency-independent waist, leading to smaller focal waists for high-frequency components. For $g_0 < -1$, the input waists of short-wavelength components (‘‘blue’’) of the beam are smaller than those of long-wavelength components (‘‘red’’), resulting in a blue focus larger than the red one. Conversely, $g_0 > 1$ represents a larger

¹For clarity, Z_R , and, W , are the Rayleigh length and the beam waist for the input beam before focusing. z_R , and, w , are the Rayleigh length and the beam waist after focusing.

blue waist of the input beam and a smaller focus with respect to the red parts. Fig. 6.3 shows the spatial properties of Gaussian beams with five characteristic values of g_0 . The first column of panels in Fig. 6.3 presents the spectral waist and the spectral divergence of Gaussian beams before the focusing optics and the second column of panels shows the spatial and spectral properties in the focus. The corresponding phase distributions are shown in the third column of panels in Fig. 6.3.

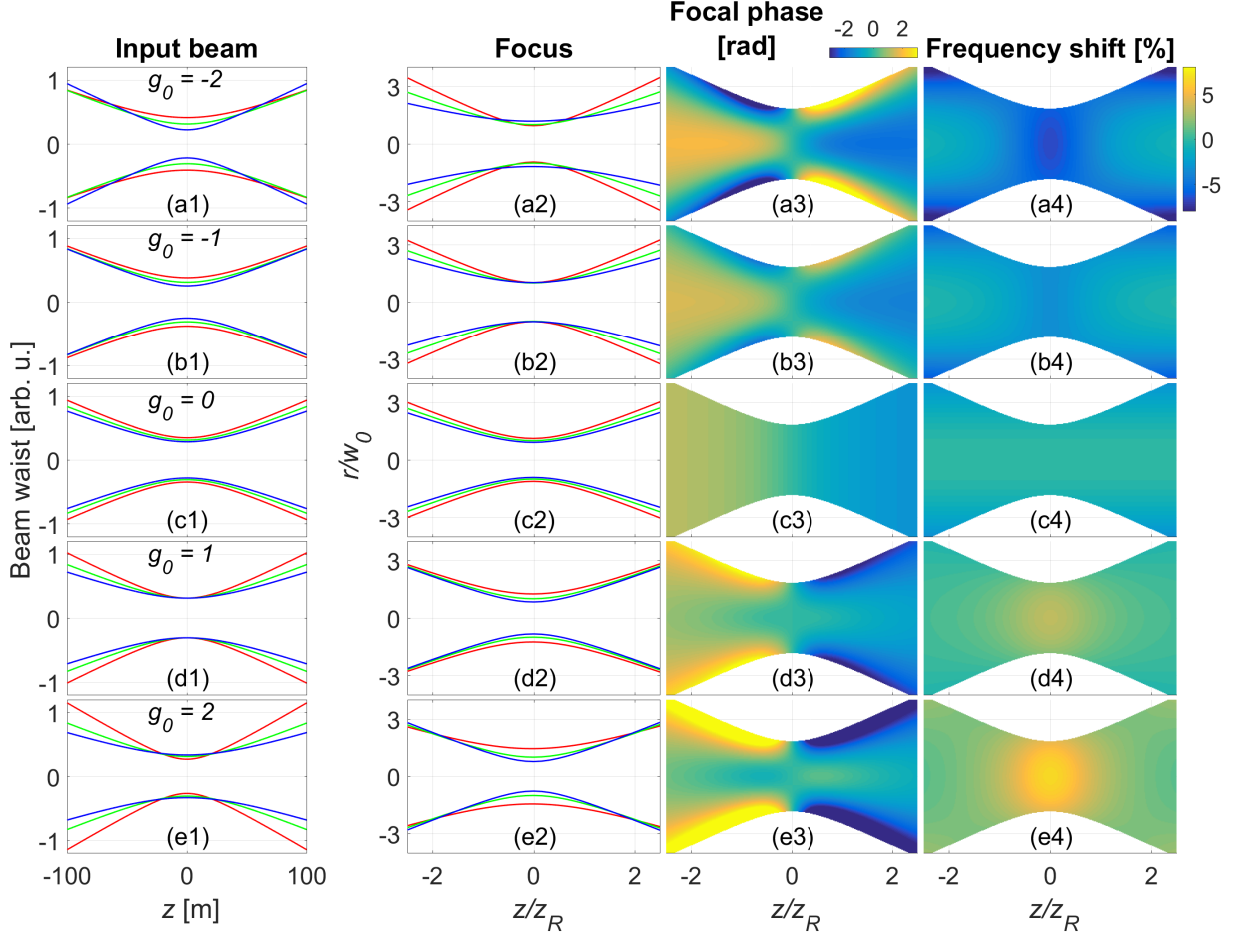


Figure 6.3: Spectral properties of Gaussian beams with different g_0 factors. (a1) - (e1) are the input beams before focusing optics. (a2) - (e2) are the beams near the focus. (a3) - (e3) The focal phase distribution near the focus. (a4) - (e4) The corresponding local frequency shifts.

Due to the different size of the spectral focus, also the effective frequency in the focus is shifted to some extent. Some previous works have reported this in the light-matter interactions under approximations either with frequency-independent width or frequency-independent divergence angle [237–240]. Similar to the analysis of the CEP shift mentioned above, using the same dimensionless factor, g_0 [110, 111], a general description of the frequency shift with different input beam waists can be derived as follows: The

local frequency can be estimated by

$$\omega_0(r, z) = \frac{\int_0^\infty \omega A_\omega^2(r, z) d\omega}{\int_0^\infty A_\omega^2(r, z) d\omega}. \quad (6.22)$$

Considering only the diffraction-induced amplitude change (i.e. the spectral amplitude up to the first order, see Eq. 6.14), the local frequency is approximated to

$$\omega_0(r, z) = \omega_0 + \frac{2A'_{\omega_0}(r, z)}{A_{\omega_0}(r, z)} \Delta\omega_{\text{rms}}^2. \quad (6.23)$$

where $\Delta\omega_{\text{rms}}$ is the root-mean-square (RMS) width of the spectral power. Knowing the amplitude of a Gaussian beam from Eq. 6.3

$$A(r, z, \omega) = \frac{w_0(\omega)}{w_\omega(z)} e^{-\frac{r^2}{w_\omega(z)^2}} \quad (6.24)$$

and the first derivative of the amplitude around the center frequency,

$$A'_{\omega_0}(r) = \frac{1}{\omega_0} \frac{A_{\omega_0}(r) \left[1 - \frac{2r^2}{w_{\omega_0}(z)^2} \right]}{1 + \frac{z_{R0}^2}{z^2}}, \quad (6.25)$$

the spatial distribution of the frequency shift in a Gaussian focus can be obtained by combining Eqs. 6.23, 6.24, and 6.25.

$$\frac{\Delta\omega(r, z)}{\omega_0} = \frac{2g_0}{1 + \left(\frac{z}{z_{R0}}\right)^2} - \frac{2r^2}{w_0(z)^2} \left[1 + g_0 \frac{1 - \left(\frac{z}{z_{R0}}\right)^2}{1 + \left(\frac{z}{z_{R0}}\right)^2} \right] \left(\frac{\Delta\omega_{\text{rms}}}{\omega_0} \right)^2. \quad (6.26)$$

The frequency shifts in percentage with different g_0 factors are shown in the last column of panels in Figs. 6.3. The center frequency has red shifts for $g_0 < 0$ and blue shifts for $g_0 \geq 0$ near the focus. The reason is that for $g_0 < 0$, the blue focus is larger than the red focus such that the red spectral component is dominating in the center of the focus.

6.3 Phase-volume Effects in Few-cycle Light-matter Interactions

We have presented the intricate phase distributions of broadband pulses in their foci. In this section, we will discuss and quantify their effect on few-cycle light-matter interactions.

To this end, we introduce an intensity-dependent yield, $Y(I)$, for the event rate of a given process. By substituting the intensity distribution of a laser focus, $I(r, z)$, into the

yield, a spatially-dependent yield, $Y(r, z)$, can be calculated. As a characteristic instance, here we use strong-field ionization of xenon and quantify the phase-volume effect for this process as a baseline. Assuming that (i) the target, i.e., atoms or molecules, has a uniform density and (ii) the probability of strong-field ionization at different intensities can be estimated using the ADK-rate [138], the spatial intensity-dependent yield can be obtained as shown in Fig. 6.4(d).

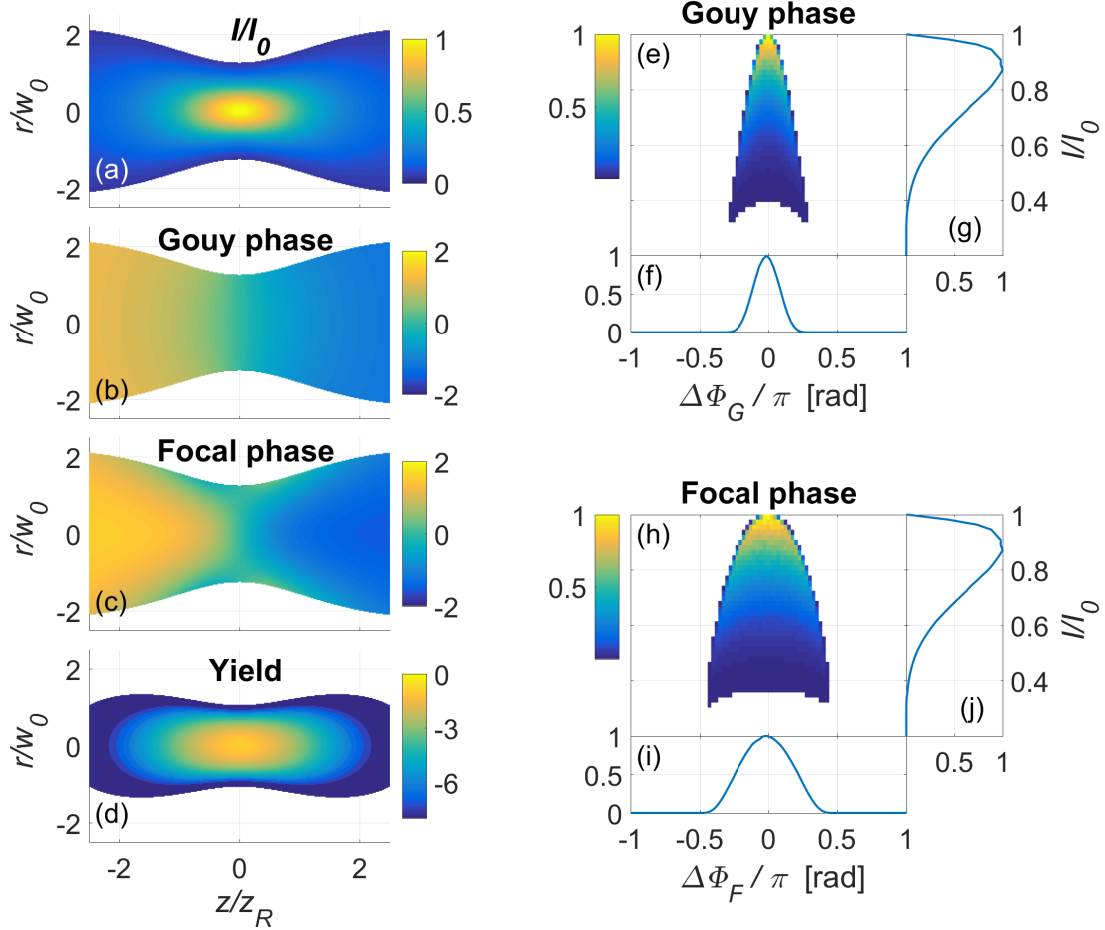


Figure 6.4: (a) Intensity distribution of a focused Gaussian laser beam (linear scale). I_0 is the peak intensity, w_0 is the beam waist, and z_R is the Rayleigh range at center frequency. (b),(c) The spatial distribution of the Gouy phase and the focal phase with a Porras factor $g_0 = -2$. (d) The intensity-dependent ionization yield on a log-scale, estimated by the ADK rate [138]. (e),(h) The normalized phase- and intensity-dependent yield taking into account the Gouy phase and the focal phase. (f), (i) The projection of the yield on the phase axis and (g), (j) on the intensity axis.

With the spatial phase distribution for a given focusing geometry, $\Delta\phi(r, z)$, one can weight and bin the spatially-dependent yield as a function of phase and intensity as

shown in Figs. 6.4(e) and (h). Using this yield, $Y(I, \Delta\phi)$, the focal-volume effect can be quantified. Note that considering an equally-spaced two-dimensional grid in r and z , the yield of measured events for each grid point needs to be adjusted according to the cylindrical symmetry $Y'[I(r, z), \Delta\phi(r, z)] = Y(r, z) \cdot r$.

In the literature, a Gouy phase distribution (in the worst case even a flat distribution) is assumed, when CEP effects are investigated [231]. Here, we compare the approximation with the Gouy phase to the real focal phase. For the latter, we will concentrate on the situation of $g_0 < -1$. In particular, we select $g_0 = -2$ as a characteristic instance. The reasons are: For few-cycle pulses generated by a hollow-core fiber compressor, to first approximation, the diameters of all frequency components are equal at the exit of the fiber. Long wavelengths cause a larger divergence for the propagation in free space after the fiber. Thus, after the collimation mirror, the blue beam diameter is smaller than the red one – which corresponds to the case of $g_0 = -1$. If such a beam is focussed, all frequency components will have the same focal waist. However, various nonlinear effects in the hollow fiber, among them self-phase modulation and self-focusing, result in a larger divergence for the long-wavelength components than predicted by diffraction only. As a consequence, g_0 will assume values in the range from -1.5 to -2.5 . An experimental proof has been presented in Ref. [232], where a Porras factor of -2.1 ± 0.2 has been measured with a similar laser system and focusing geometry to our experimental conditions. Accordingly, we can regard $g_0 = -2$ as a good approximation for the subsequent analysis. In the MIR, where few-cycle pulse compression relies on bulk material, the situation seems to be similar.

For reference, the spatial distribution of the Gouy phase near the focus is shown in Fig. 6.4(b). Fig. 6.4(c) displays the more realistic case for few-cycle pulses, $g_0 = -2$, and reveals a substantially different phase distribution. Using the procedure described above, the phase- and intensity-dependent yield for both phase distributions are obtained in Fig. 6.4(e) and (h). The projection of this yield on each axis highlights two volume effects, namely the “intensity-volume effect” and the “phase-volume effect”.

Figs. 6.4(f) and (i) show the projection of the yield on the phase-axis, which indicate the phase-volume effect. It can be seen that the phase distribution due to the focal phase is much broader than in the Gouy phase case. The decisive conclusion is that CEP averaging is considerably more pronounced for few-cycle pulses than estimated by

assuming the phase distribution of a monochromatic beam.

In order to quantify this statement, the RMS of the distribution is calculated:

$$\Delta\phi_{\text{rms}} = \sqrt{\frac{\int_r \int_z Y(r, z) \cdot [\Delta\phi(r, z) - \phi_{\text{cm}}(r, z)]^2 \cdot 2\pi r \, dr dz}{\int_r \int_z Y(r, z) \cdot 2\pi r \, dr dz}} \quad (6.27)$$

with

$$\phi_{\text{cm}}(r, z) = \frac{\int_r \int_z Y(r, z) \cdot \Delta\phi(r, z) \cdot 2\pi r \, dr dz}{\int_r \int_z Y(r, z) \cdot 2\pi r \, dr dz} \quad (6.28)$$

where $\phi_{\text{cm}}(r, z)$ is the center-of-mass of the projection of the phase distribution. For a monochromatic beam, the RMS of the phase distribution is only 0.09π rad. In contrast, for broadband pulses with $g_0 = -2$, the RMS of the phase distribution increases significantly and varies from 0.20π to 0.27π rad, with the g_0 -factor varying from -1.5 to -2.5 , which corresponds to achievable frequency-dependent beam radii for typical fiber compressor-based few-cycle laser systems. For the $g_0 = -2$ case detailed in this thesis, the corresponding RMS is $\sim 0.25\pi$ rad. This constitutes a roughly 3 times broader phase distribution as compared to the Gouy case and implies a much stronger averaging effect, leading to a significantly reduced contrast of CEP effects.

An analogous analysis can be made for the intensity-volume effect, see Figs. 6.4(g) and (j). The figures reproduce the well-known fact that most of the yield is not produced by the peak intensity I_0 , but comes from regions in the focus, where the intensity is somewhat lower. The larger probability of ionization in the center of the focus cannot counteract the vanishingly small interaction volume. For phenomena with lower nonlinearity, i.e. a less steep intensity dependence, the contributions from regions with even lower intensities will dominate the yield of the concerned event. For the present example of ionization of xenon, the mean value of the intensity distribution is $\sim 0.8I_0$ and the RMS of the intensity distribution is $\sim 0.13I_0$.

6.4 The Phase-volume Effect at 1.8 μm

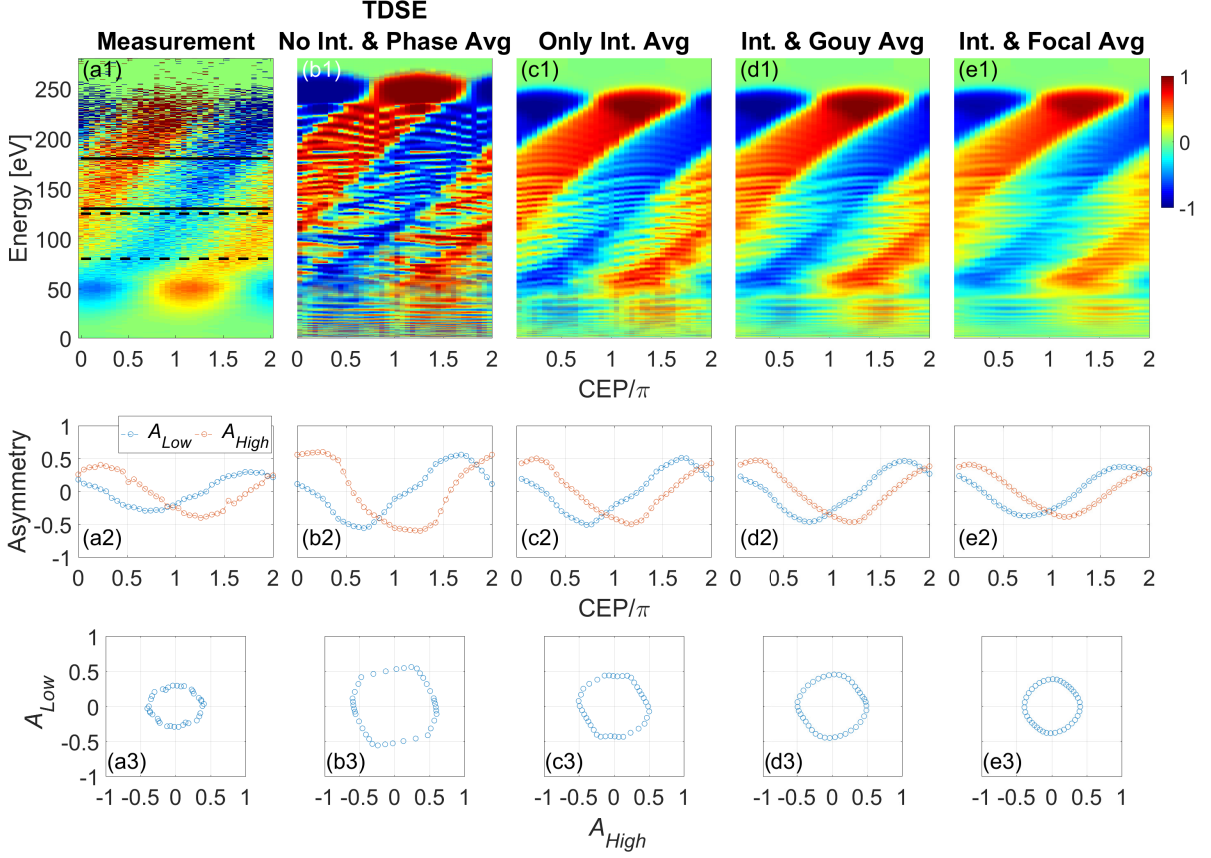


Figure 6.5: Comparison between the measurements and TDSE simulations of strong-field ionization of xenon at 1.8 μm . (a1) Measured asymmetry with $\tau = (11.8 \pm 0.5)$ fs, $I_0 = (0.8 \pm 0.2) \times 10^{14}$ W/cm 2 . (b1) Simulated asymmetry without the intensity- and phase-averaging effect with $\tau = 12$ fs, $I_0 = 0.8 \times 10^{14}$ W/cm 2 . (c1) Simulated asymmetry including only the intensity-volume effect. (d1) Simulated asymmetry including both effects but only considering the Gouy phase. (e1) Simulated asymmetry including both effects with the focal phase distribution for few-cycle pulses with $g_0 = -2$. (a2) - (e2) The corresponding asymmetries $A_{\text{low}}(\phi)$ and $A_{\text{high}}(\phi)$ of the two energy regions indicated in panel (a1). These are used to plot the corresponding PAPs (a3) - (e3).

The intensity- and phase-dependent yield in the laser focus for a given process has been calculated in the previous section. In this section, simulated asymmetry maps obtained from the ATI spectra of xenon including the volume effect will be compared to the measurements. The measurements were performed with ~ 12 -fs, 1.8- μm pulses around a peak intensity of 0.8×10^{14} W/cm 2 . The measured asymmetry map is compared with the simulated asymmetry maps computed by solving the one-dimensional TDSE, see Fig 6.5. The

simulated asymmetry using a single intensity, i.e. considering neither the intensity-volume nor the phase-volume effect, is shown in Fig. 6.5(b1), while the simulated asymmetry considering only the intensity-volume effect but not the phase-volume effect is shown in Fig. 6.5(c1). We can see that the intensity-volume effect smears out fine structures in the asymmetry map to a large extent. The $10U_p$ cutoff is lower and the phase-dependence is also smaller due to averaging the contributions from lower intensities in the focus. Even though, the amplitude of the asymmetry for each energy region is still larger than for the measured asymmetry. The discrepancies can be seen more clearly by plotting the asymmetries for two energy regions [see Figs. 6.5(a2) - (e2)] and the corresponding PAPs [Figs. 6.5(a3) - (e3)].

Next, we further include the phase-volume effect in the simulation. When the Gouy phase is considered, the asymmetry amplitude is indeed reduced, but only to a small extent [see Fig. 6.5(d1)], i.e., the discrepancies with respect to the experiment still remain. In consideration of the results presented in Section 6.3, this is not a surprise. Therefore, finally the focal phase with $g_0 = -2$ is included in the analysis [see Fig. 6.5(e1)]. One can clearly see a further blur in the phase-dependence of the asymmetry map and a significantly smaller PAP, now in a better agreement with the measurements.

We apply this analysis also on the semi-classic simulation results and observe a similar behaviors. Indeed, the simulated results from the semi-classic calculation also show a much better agreement with the measurements as compared to those ignoring the phase-volume effect, see in Fig 6.6.

So far, the PAP has been calculated from experimental data recorded with the high-resolution TOF spectrometer. In this measurement, thousands of laser pulses are required for this instrument to obtain a spectrum with sufficiently low statistical noise. Now we apply the phase-volume effect on the single-shot CEP measurement with a CEP at 1.8 μm .

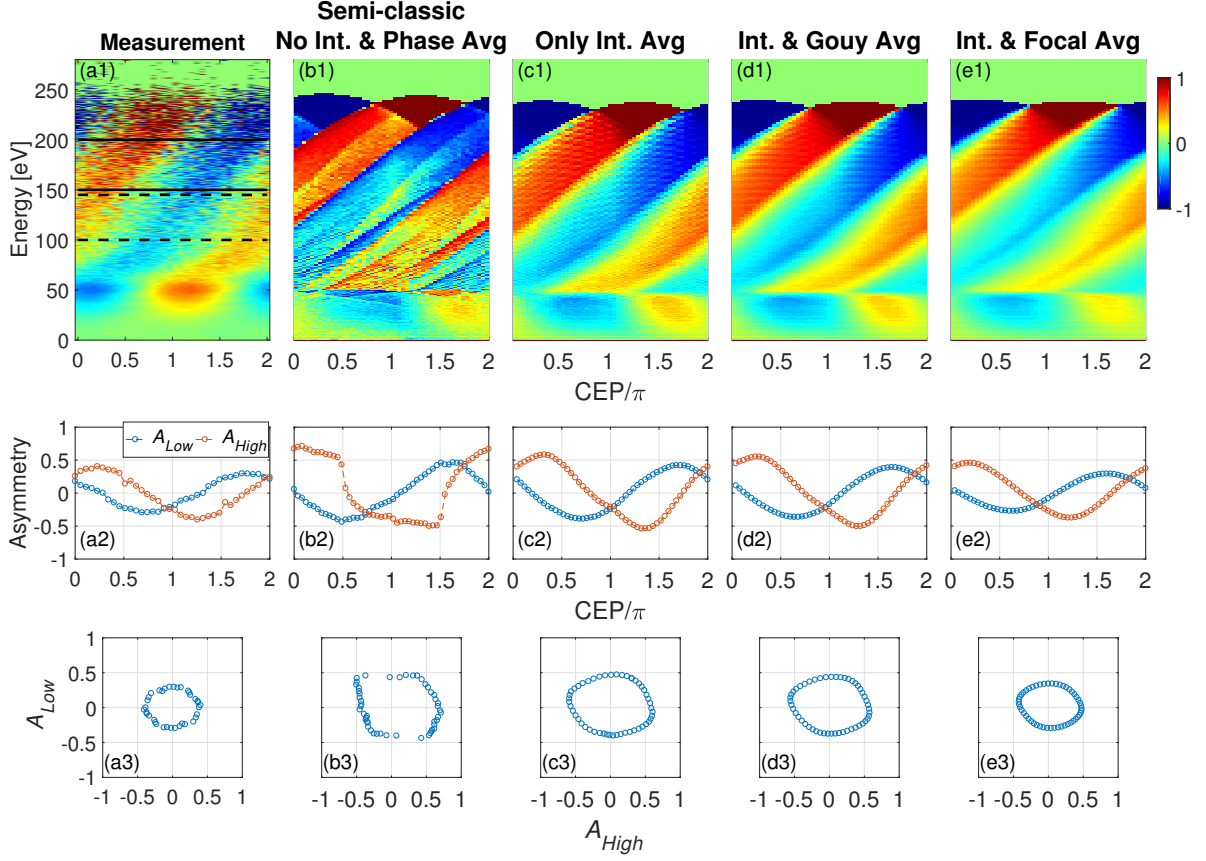


Figure 6.6: Comparison between the measurements and the semi-classic simulations of the strong-field ionization of xenon at 1.8 μm . (a1) Measured asymmetry with $\tau = 11.8 \pm 0.5$ fs, $I_0 = (0.8 \pm 0.2) \times 10^{14}$ W/cm 2 . (b1) Simulated asymmetry excluding the intensity- and phase-averaging effect with $\tau = 12$ fs, $I_0 = 0.8 \times 10^{14}$ W/cm 2 . (c1) Simulated asymmetry including only the intensity-volume effect. (d1) Simulated asymmetry including both effects but only considering the Gouy phase. (e1) Simulated asymmetry including both effects considering the focal phase distribution for few-cycle pulse with $g_0 = -2$. (a2) - (e2) The corresponding asymmetries of two energy regions for plotting the PAP. (a3) - (e3) The PAP using the asymmetries from (a2) - (e2).

The PAP measured with a CEP M using (10.4 ± 0.5) -fs pulses at 1.8 μm is shown in Fig. 6.7(a). The simulated PAPs from both theoretical models are shown in Figs. 6.7(b) and (c). The blue dots (inner PAP) and the red dots (outer PAP) are the simulated traces with and without consideration of the focal phase, respectively. Both traces include the intensity-volume effect. As before, the inclusion of the focal phase in the theoretical model reduces the radius of the PAP due to the more pronounced averaging effect of the CEP.

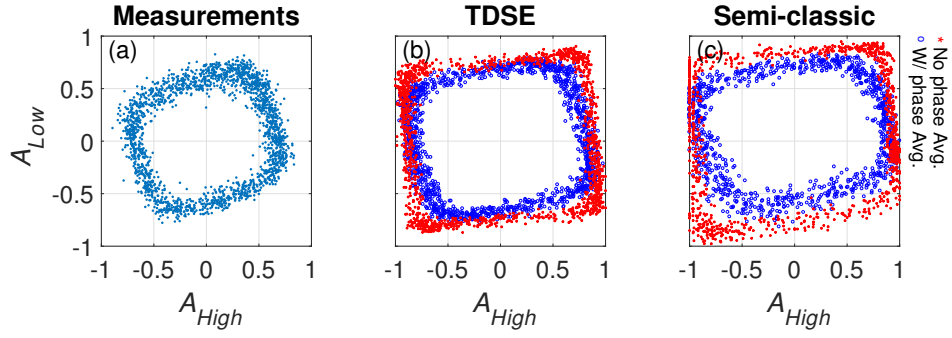


Figure 6.7: (a) Measured PAP by a CEPM with 10.4 ± 0.5 fs pulses at 1.8 μm . (b) Calculated PAPs from a TDSE simulation with $\tau = 10$ fs pulses. The peak intensity is $I_0 = 0.8 \times 10^{14}$ W/cm 2 . The blue circles and red stars represent the case with and without the phase-volume effect, respectively. Two energy regions for plotting the PAP correspond the regions within black dashed lines and black solid lines in Fig. 6.5. (c) Calculated PAPs from the semi-classic simulation with $\tau = 10$ fs pulses. The peak intensity is $I_0 = 0.8 \times 10^{14}$ W/cm 2 .

The significance of the CEP increases with a decrease in pulse length. As already pointed out in Section 4.2, the strength of the CEP-dependence can also serve as a good way for pulse length calibration. However, not taking the phase distribution into account or not properly accounting for the focal phase may lead one to significantly overestimate the pulse duration.

Fig. 6.8 displays respective data obtained with a CEPM under single-shot conditions. For various pulse durations at 1.8 μm , the mean radius of the PAP are shown in Fig. 6.8(a). Unsurprisingly and independent of pulse duration, the simulations excluding the focal phase always predict larger radii than the measurements. Though the radii shrink slightly when the Gouy phase is taken into account in the simulations for both models (green-square dots in Fig. 6.8, large discrepancies still remain compared to the measurements. Only when the focal phase is considered for a more realistic analysis, the radii of the PAPs further shrink [see the red diamond-shape dots in Figs. 6.8(a) and (c)] and match the measurements.

In order to show this effect more concretely, the difference of the mean radius of the PAP between the simulations with and without the focal phase effect is calculated, see Figs. 6.8(b) and (d). With this analysis, a better pulse duration calibration with a CEPM can be realized.

In general, excluding the intensity- and phase-volume will lead one to expect a significantly larger phase-dependence than is measured and inversely, these exclusions will lead one to believe that their pulse is longer and less intense than in reality. This general effect has been measured from different phase experimental apparatus (the high-resolution TOF-spectrometer and the CEP) also validate our experimental treatment and parameters we select in different simulations.

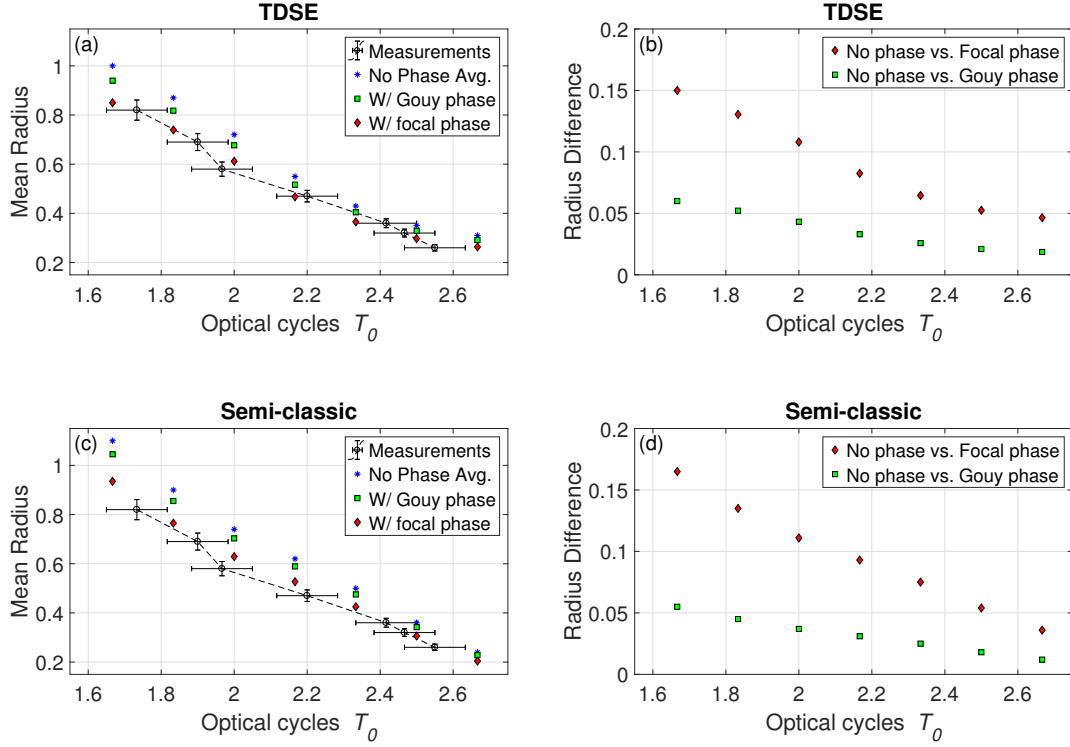


Figure 6.8: (a), (c) Comparison between the radii of the PAPs obtained from a CEP) and simulations from a TDSE calculation and a semi-classic calculation at $1.8\ \mu\text{m}$. The measurements are calibrated with a home-built frequency-resolved optical gating (FROG) device. (b), (d) Difference of the mean radius between only considering the intensity-volume effect and cases with considering the Gouy phase or the focal phase.

6.5 The Phase-volume Effect at 0.8 μm

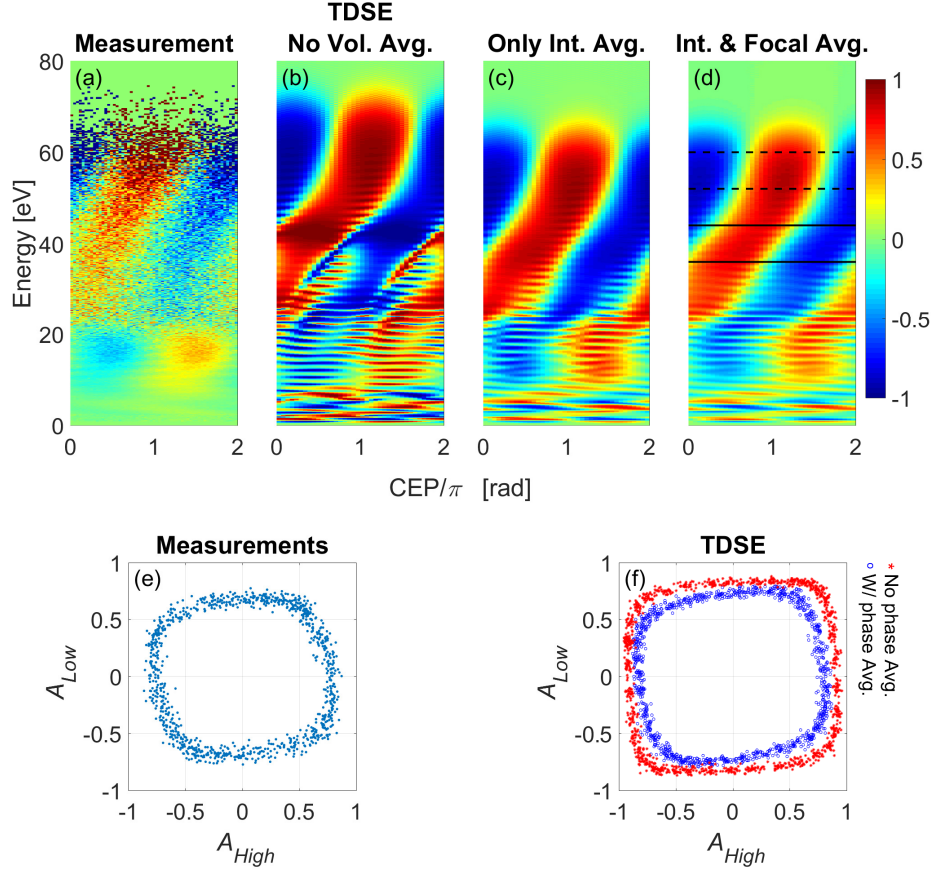


Figure 6.9: Comparison between the measurements and the simulations of strong-field ionization of xenon at 0.8 μm . (a) Measured asymmetry with $\tau = 5 \pm 0.3$ fs, $I_0 = (0.8 \pm 0.2) \times 10^{14}$ W/cm². (b) Simulated asymmetry from the TDSE calculation excluding the intensity- and phase-averaging effect with $\tau = 5$ fs, $I_0 = 0.8 \times 10^{14}$ W/cm². (c) Simulated asymmetry including only the intensity-volume effect. (d) Simulated asymmetry including both intensity-volume and phase-volume effects with $g_0 = -2$. (e) Measured PAP by a CEPm with $\tau = (4 \pm 0.3)$ -fs pulses at 0.8 μm . (f) Simulated PAPs with $\tau = 4$ -fs pulses. The blue and red dots represent the case with and without the phase-volume effect, respectively. Two energy regions within black dashed lines and black solid lines in (d) are selected to obtain the PAPs.

In order to further validate of our conclusions, we go back to the case of 0.8 μm . The pulse length measurements of few-cycle pulses at 0.8 μm [32] with a SPIDER device are compared to the numerical data. This would also confirm that our conclusions are not limited to specific processes or experimental parameters, as implied by the very general analysis in chapter 6. By shifting the wavelength, but keeping the intensity, we actually

change the regime of strong-field ionization from tunnel ionization in direction of multi-photon ionization, as evident by the respective Keldysh parameters [133]. Observing the same significant phase-volume effect at 0.8 μm as at 1.8 μm would be a strong indication of the validity of our analysis.

Fig. 6.9(a) shows the asymmetry obtained from ATI spectra of xenon measured with a TOF spectrometer. The pulse duration was 5 ± 0.3 fs. The corresponding asymmetry calculated from the 1D-TDSE simulations considering neither the intensity-volume nor the phase-volume effect is shown in Fig. 6.9(b). The same considering only the intensity-volume effect and not the phase-volume effect is shown in Fig. 6.9(c). Finally, simulated asymmetry including both effects is shown in Fig. 6.9(d). For computing the phase-volume effect, we still used $g_0 = -2$ as the few-cycle pulses at 0.8 μm are generated from a hollow-core compressor as well. One can see the significant blurring of the phase dependence due to the intensity- and phase-volume effect.

A PAP obtained with a CEP in single-shot operation is shown in Fig. 6.9(e). For comparison, the simulated PAP are presented in Fig. 6.9(f). The blue dots (inner circle) and red dots (outer circle) are the simulated intensity-averaged traces with and without the focal phase, respectively.

The evaluation of pulse duration measurements of few-cycle pulses at 0.8 μm with a CEP are shown in Fig. 6.10. As expected, the simulations without considering the focal phase always predict larger radii, i.e. a larger CEP dependence than the measurements. Though the radii slightly shrink when the Gouy phase is taken into account in the simulation (green-square dots in Fig. 6.10), large discrepancies still remain compared to the measurements. Very similar to the case of 1.8 μm , the simulations are in much better agreement with the measurements when the proper phase distribution in the focus is taken into account.

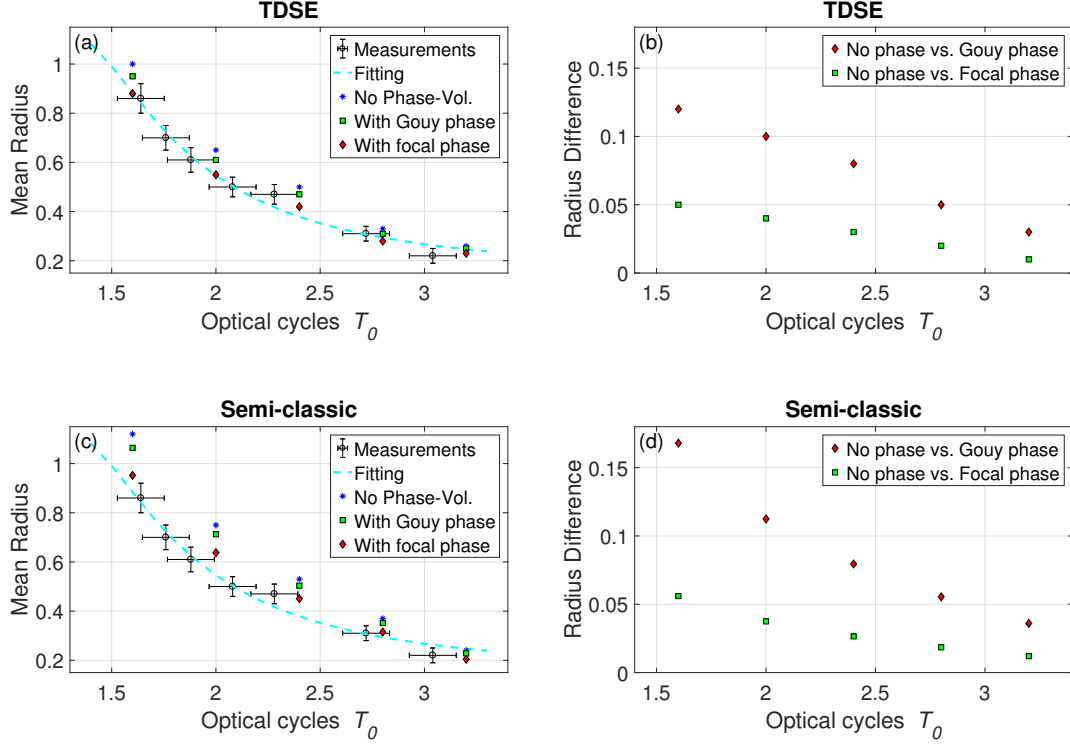


Figure 6.10: (a), (c) Comparison between the radii of the PAPs obtained from a CEPM and simulations from a TDSE calculation and a semi-classic calculation at $0.8 \mu\text{m}$. The measurements are calibrated with a commercial spectral phase interferometry for direct electric-field reconstruction (SPIDER) device. (b), (d) Difference of the mean radius between only considering the intensity-volume effect and cases with considering the Gouy phase or the focal phase.

With this analysis, a new and more accurate CEP measurement has been realized and the pulse length measurement of NIR pulses from a CEPM [32] has been recalibrated.

6.6 Further Discussion

6.6.1 Other Effects on the Phase Distribution

So far, we have presented how the frequency-dependent waist and frequency-dependent divergence of the beam, which are described by g_0 -factor, can change the phase distribution in the laser focus. However, other effects can also contribute to the phase distribution, e.g., the chirp and imaging aberrations. In Ref. [112], based on the results in Eq. 6.20, both phenomena are discussed and an optimized 3D description of the focal phase was

given:

$$\Delta\phi(r, z) = -\arctan\frac{z}{z_R} + \frac{1 - 2\frac{r^2}{w_{\omega_0}^2(z)}}{1 + (\frac{z}{z_R})^2} \times \left[G\left(\frac{z}{z_R}\right) + \Gamma\left(\frac{z}{z_R}\right)^2 \right] + \left[\Gamma + \frac{2C_r}{\tau^2} \right] \frac{r^2}{w_{\omega_0}^2(z)}, \quad (6.29)$$

with

$$G \equiv g_0 - \gamma_a \frac{2C_r}{\tau^2}, \quad (6.30)$$

$$\Gamma \equiv \gamma_a + g_0 \frac{2C_r}{\tau^2}, \quad (6.31)$$

where C_r is the chirp parameter and $\gamma_a = \left. \frac{df(\omega)}{d\omega} \right|_{\omega_0} \frac{\omega_0}{Z_R(\omega_0)}$, a dimensionless parameter similar to g_0 . γ_a quantifies the chromatic aberration based on the analysis of the frequency-dependent focal length $f(\omega)$.

In our experiments, we minimized the chirp by scanning the silica wedges for each measurements. By finding the largest ionization yield and the largest phase dependence, we can determine if the chirp is well compensated. If high-order dispersion plays a role, one may observe more than one maximum of the radius of the PAP, as discussed in Section 4.2. Thus, we assume that higher-order effects, e.g., the chirp is rather small in our case. We also ignored aberrations from the focusing optics because the theoretical treatment of the focal phase using Eq. 6.20 has shown that it is sufficient to bring the theoretical results into agreement with experiments. For specific cases, however, these two parameters may be required to match the experimental conditions. The details of the discussion about the influence of C_r and γ_a on light-matter interactions can be found in Ref. [241, 242].

6.6.2 Confinement of the Interaction Volume

In order to reduce the phase-volume effect, the interaction volume in the experiments is often confined by placing a narrow slit in the electrons' path or by using a beam target which behaves as an effective slit with respect to the Rayleigh range of the laser beam. In the following simulations, we investigate how the size of the slit influences the phase-volume effect. The RMS of the phase distribution for different sizes of the slit and the corresponding radii of the PAPs are shown in Fig. 6.11, where a 10-fs pulse at 1.8 μm has been used as an example. From this figure, we can see a quantitative difference

between the focal phase and the Gouy phase. It shows that a slit would yield only a small advantage for a Gouy phase distribution. This conclusion is consistent with the results presented in previous sections, in particular in Fig. 6.4.

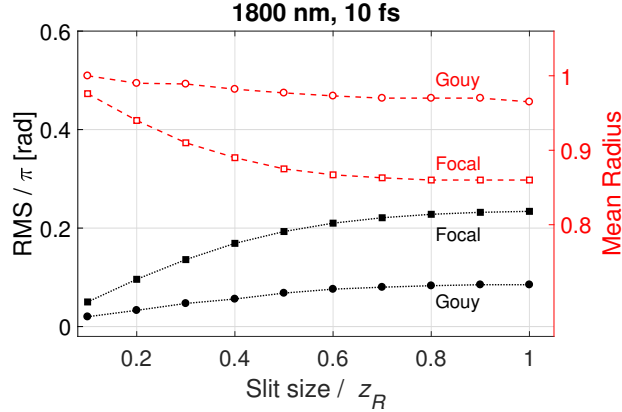


Figure 6.11: RMS of the phase distribution of strong-field ionization in xenon with different slit sizes and the corresponding PAP radii of 10-fs pulses at 1.8 μm .

When the size of the slits is enlarged, the RMS of the phase distribution naturally increases. Thus, the radius of the PAP decreases. When the size of the slit is comparable to one Rayleigh range of the laser beam, the RMS and the radius of the PAP almost remain the same, because the yield at positions far away from the laser focus dramatically drops due to the low intensity. In particular, if the slit size is larger than z_R , it has no significant impact on reducing the phase effect. Even for slit sizes $> 0.5z_R$, the influence is small. If one wants to suppress the phase-volume effect efficiently, the target beam diameter or the slit size should be smaller than $0.5z_R$. Of course, the direct consequence of strongly confining the interaction volume is a dramatic reduction of the ionization yield, e.g., $\sim 30\%$ less in strong-field ionization when the volume is confined to $0.5z_R$. Thus, for experiments with limited pulse energy and thus tight focussing, the focal-volume effect is inevitable.

6.6.3 Phase-volume Effect on Phenomena with Different Non-linearities

So far, we have discussed the phase-volume effect in strong-field ionization, which is a highly nonlinear process, for which the interaction volume is naturally confined by the strongly nonlinear intensity-dependence of the yield. As the phase-volume effect still

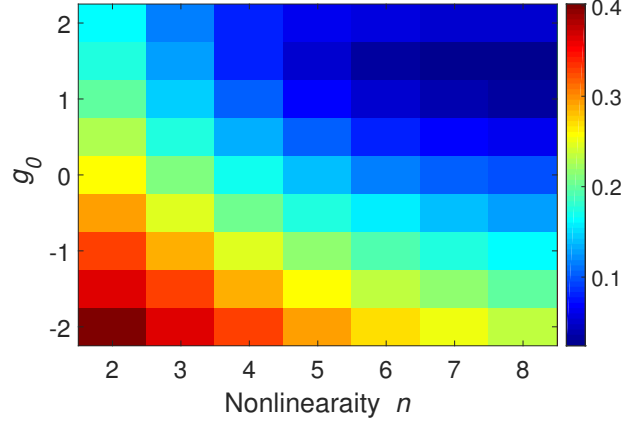


Figure 6.12: RMS of the phase distribution for light-matter interactions with different degrees of nonlinearity, n , with the probability of events, $P \sim I^n$, where I is the laser intensity.

cannot be neglected for such a highly nonlinear process, this situation is expected to be even worse for processes with lower nonlinearities, such as molecular dissociation [243], and multi-photon absorption [244] among others due to the larger effective interaction volume determined by the intensity-dependent yield.

To analyze this situation and estimate the phase-volume effect for a broad range of few-cycle laser-induced dynamics, we assume a power-law intensity dependence for the probability P of events, i.e. $P \sim I^n$, where I is the laser intensity and n can be considered as the degree of nonlinearity. Using this ansatz, we can determine how much the CEP-dependence will be washed out for a given process. For example, the ADK ionization rate for xenon can be approximated as $n = 6$. Scanning over the nonlinear parameter, n , yields an n -dependent RMS of the phase distribution, see Fig. 6.12. As expected, a larger RMS, indicating a stronger phase-volume effect, is predicted for lower-order nonlinear phenomena due to the larger effective interaction volume.

Chapter 7

CEP-dependent Laser-matter Interactions in MIR Range

As pointed out in Chapter 1, increasing the driving laser wavelengths is interesting in many aspects. Nevertheless, relevant experiments performed with MIR few-cycle pulses are still relatively rare, mainly because of the low prevalence of few-cycle MIR laser systems, their limited pulse energy, and their low repetition rates. Due to the principles of strong-field light-matter interactions, specifically the ionization process and low rescattering/recombination cross-section, both pulse energy and repetition rate are badly needed to obtain sufficient statistics for the measurements. Therefore, the new-built MIR laser system at ELI-ALPS (see Section 4.1.2), which can deliver CEP-locked few-cycle pulses with up to 80 μJ pulse energy at 100 kHz repetition rate, is an attractive laser system for our investigations.

In this chapter, we will present our measurements of CEP-dependent ATI spectra of two contrasting atoms, namely xenon (Xe) and caesium (Cs), using 3.2- μm few-cycle pulses. As a benchmark, first CEP-dependent high-resolution ATI spectra of Xe and the corresponding asymmetry will be presented and compared to simulations. Next, we tested a Xe-CEPM to measure the CEP of MIR pulses in order to test the capability of a CEPM operating at this wavelength.

Due to the extremely low yield of rescattered electrons for xenon at long wavelengths, the single-shot CEP measurement with a CEPM based on xenon is expected to be very challenging and will require substantial laser pulse energy. Therefore, we tested an alternative target, an alkali atom, specifically Cs. It could be a potential candidate for

substituting noble gases in the CEPM as it has a much lower ionization potential and a comparable or even larger rescattering cross-section at long wavelengths as compared to noble gases [245]. In the second section of this chapter, the CEP-dependent ATI spectra and the corresponding asymmetry of Cs at 3.2 μm will be presented and compared to the simulations. We will test its potential for measuring the CEP. Doing so, an unusual CEP-dependence in Cs is noticed, in particularly at high intensities. By applying different models, this anomalous CEP effects is investigated.

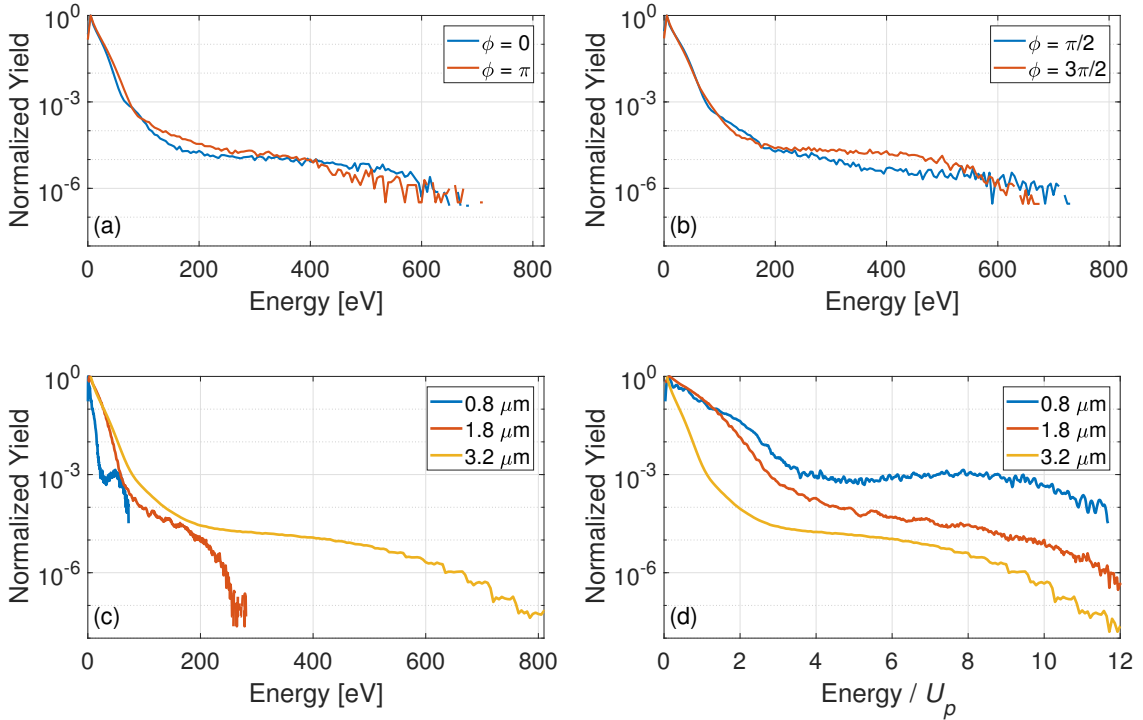


Figure 7.1: ATI spectra of xenon using CEP-stable 3.2- μm , 25-fs pulses. The peak intensity is $0.8 \times 10^{14} \text{ W/cm}^2$. (a), (b) ATI spectra with CEP $\phi = 0$ and $\pi/2$. (c), (d) CEP-averaged ATI spectra of xenon at different wavelengths.

7.1 Strong-Field Ionization of Xe at 3.2 μm

First, we measured the ATI spectrum of xenon at 3.2 μm as a benchmark with a high-resolution TOF spectrometer. The shortest pulse duration we obtained was 25 fs (about 2.5 optical cycles). The measured ATI spectra with different CEPs are shown in Figs. 7.1(a) and (b). In Figs. 7.1(c) and (d), the CEP-averaged ATI-spectra of xenon at different wavelengths, while keeping the peak intensity constant ($\sim 0.8 \times 10^{14} \text{ W/cm}^2$, estimated from the

cutoff position), are compared by plotting the photoelectron yield against an absolute energy axis (eV) and a scaled energy axis (ponderomotive energy U_p). At this peak intensity, as the cutoff energy scales with $U_p \sim I\lambda^2$, the maximum photoelectron energy reaches 800 eV. As discussed in the Section 5.1, the rescattering yield can be assumed to scale as λ^{-4} . Indeed, our measurements show that the total yield of rescattered electrons at 1.8 μm is roughly 10 times larger than that for 3.2 μm , which is compatible with our estimation of the magnitude of the wavelength scaling factor. It is evident that a very high repetition rate of the laser system is extremely helpful for this kind of measurements.

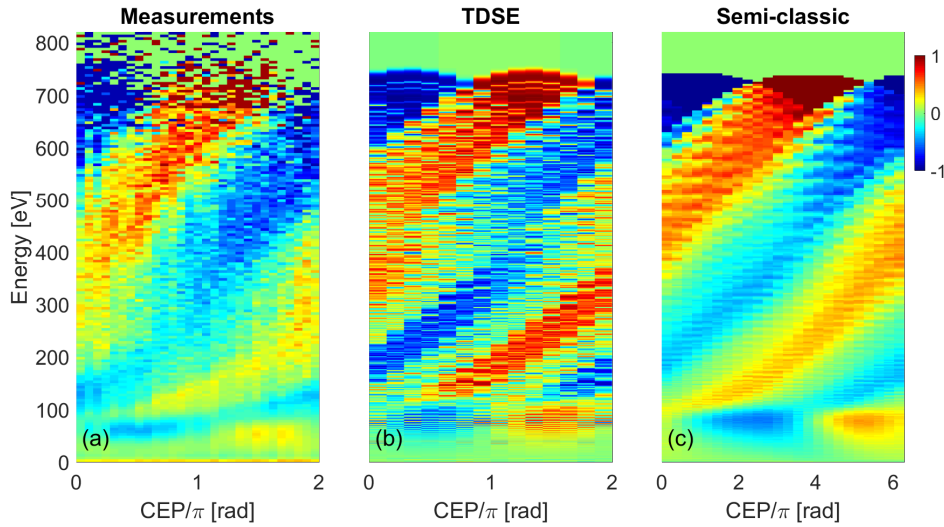


Figure 7.2: (a) The asymmetry map of xenon using CEP-stable 3.2- μm , (25 ± 0.5) -fs pulses. The peak intensity is $(0.8 \pm 0.1) \times 10^{14} \text{ W/cm}^2$. (b), (c) The calculated asymmetry maps from TDSE and semi-classic simulations, respectively, for the same parameters.

From the ATI spectra, the corresponding asymmetry map for xenon at 3.2 μm was obtained, shown in Fig. 7.2(a). Figs. 7.2(b) and (c) present calculated asymmetry maps from the TDSE calculation and the semi-classic simulation, respectively. The measured asymmetry amplitude of up to 0.5 suggests that the ATI spectra of xenon can be used for measuring the CEP. However, if one has a single-shot CEP in mind, one should use a large focus in order to generate a sufficient number of plateau electrons. The pulse energy for MIR pulses would need to be scaled with λ^4 .

The simulations presented above include the intensity-volume effect only since we could not measure the spectral divergence and the spectral waist of MIR few-cycle pulses as we were running out of beam time at ELI ALPS. This does not imply that we would

deem the focal phase effect as non-existing or negligible. As discussed in Section 6.3, due to the nonlinear effects in the spectral broadening process, the divergence of the beam may increase which results in a larger beam diameter for the “red” components than for the “blue” components. This corresponds to a situation where g_0 is smaller than -1 . Furthermore, the bandwidth of the pulse exceeds 600 nm. Thus, we assume that the phase-volume effect is as significant as the case of 0.8 μm and 1.8 μm that we discussed in Chapter 6. We indeed observed that the asymmetry amplitude in the simulations is larger than the measurements, see Fig. 7.2.

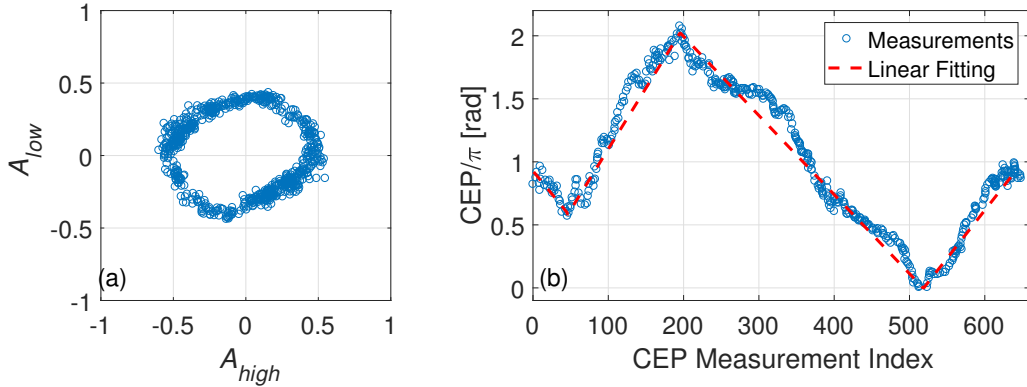


Figure 7.3: The CEP measurement at 3.2 μm . (a) The PAP trace measured with a Xe-CEPM. 500 laser shots were averaged for one CEP measurement. (b) Retrieved CEP over time.

We also tested the operation of a Xe-CEPM for measuring the CEP of the MIR pulse. The CEP of the laser was locked and a phase-control unit in the laser system was applied to scan the CEP by 2π linearly. As expected, due to the extremely low yield of rescattering electrons in the plateau region, single-shot CEP measurements is impossible at 3.2 μm with xenon as target atoms. Specifically, the detector recorded just a few of events (3-6) per laser shot. Therefore, we had to accumulate events for over 500 laser shots for each CEP. In total, around 2 thousand electrons in the plateau region were required to obtain a phase measurement. The corresponding PAP trace is shown in Fig. 7.3(a). Again, this is in agreement with the estimations discussed in Section 5.4.1.

The retrieved CEPs during the scanning of the CEP are shown in Fig. 7.3(b) and the red dashed line is the corresponding linear fit. The CEP stability of the laser system itself is (80 ± 20) mrad and the standard deviation from the measured points to the linear fit is about 100 mrad. The precision of the CEP measurement calculated from the PAP trace is approximately around 165 mrad. The measurements show that despite of the low electron

yield, a precise CEP measurement using a CEP-M can be achieved, even with xenon as the target, if the laser source itself has sufficient pulse energy and CEP stability.

7.2 Strong-field Ionization of Cs at 3.2 μm

In order to find an alternative target for a single-shot CEP-M at MIR wavelengths, we investigated strong-field ionization of alkali atoms. However, alkali atoms are in fact an interesting case on their own right, for at least two reasons. First, cesium as a characteristic instance of an alkali atom, has an ionization energy of just 3.9 eV, much lower than that of Xe (12.12 eV). Thus, much less intensity is required for ionization. As a consequence, a much higher electron yield can be reached in a single laser shot, even for limited pulse energy. Another reason for selecting alkali atoms is that they have only one electron in their valence shell. Ionization thus results in a closed shell. Indeed, the ionization energy for the second electron is very high as compared to the first ionization stage, for example, 25 eV for Cs^+ . Alkali atoms are pretty much the opposite case of rare gases, where one starts with a closed shell that is opened by ionization. One may also argue that the alkalis allow to study strong-field light-matter interaction in systems, where the use of the single-electron approximation is much more justified as for other typically used targets.

Figs. 7.4(c) and (d) show ATI spectra of Cs measured by a high-resolution TOF spectrometer with (31 ± 0.5) -fs pulses at 3.2 μm for different CEPs. Due to specific conditions of the laser system during the beam time, the shortest pulse duration achieved for experiments of Cs was about 30 fs, corresponding to 2.8 cycles. The peak intensity is approximately (1.8 ± 0.2) TW/cm², as estimated from the cutoff of the spectrum. The pulse energy inside the vacuum chamber is about 13 μJ . The corresponding asymmetry map calculated from the measurements is shown in Fig. 7.4(e).

Next, we compare the CEP-averaged ATI spectrum of Cs to the one of Xe for the same Keldysh parameter ($\gamma \approx 1.1$). For this purpose, the ATI spectrum of Cs at 3.2 μm with a peak intensity of 1.8 TW/cm² is compared to the ATI spectrum of Xe measured at 0.8 μm with a peak intensity of 0.8×10^{14} W/cm². Remarkably, the yield of plateau electrons from the Cs atoms measured at 3.2 μm is comparable or even higher than the one for Xe measured at 0.8 μm . At the same time, the peak intensity is 40 times lower

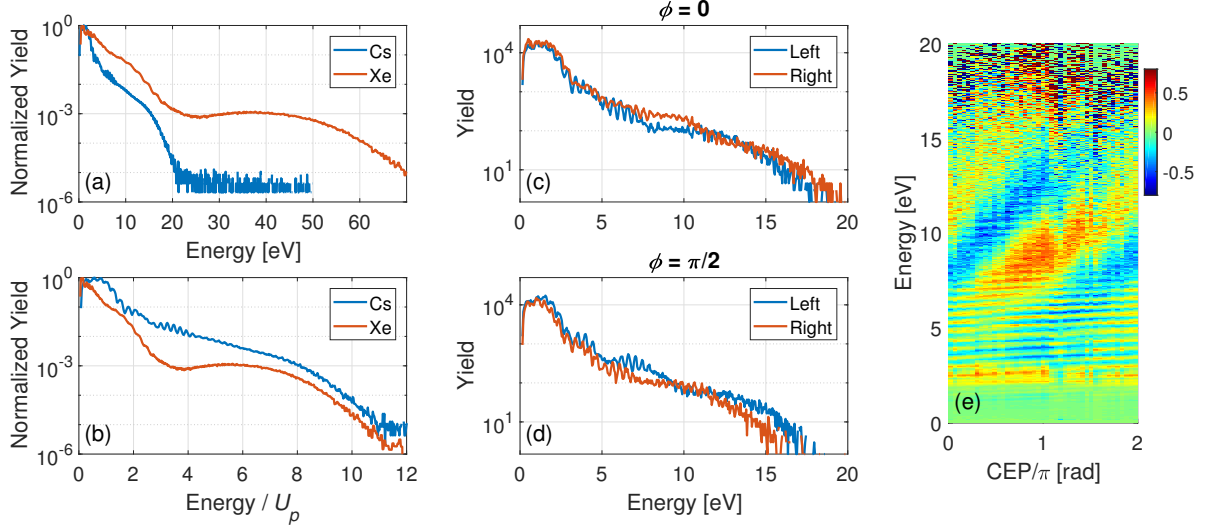


Figure 7.4: The measurements of strong-field ionization of Cs at 3.2 μm . (a),(b) Comparison of normalized CEP-averaged ATI-spectrum between Cs and Xe against the absolute energy (eV) and the ponderomotive energy (U_p) axis, respectively. The ATI-spectrum of Cs is measured by 31 ± 0.5 -fs pulses at 3.2 μm with a peak intensity of $(1.8 \pm 0.1) \times 10^{12}$ W/cm 2 . The ATI-spectrum of Xe is measured by 5-fs pulses at 0.8 μm with a peak intensity of 0.8×10^{14} W/cm 2 . (c),(d) The ATI-spectra of Cs for different CEPs. (e) The corresponding asymmetry map of Cs at 3.2 μm .

than in the case of Xe, which has compensated the loss due to the high-energy electrons scaling with λ^{-4} to a great extent.

Further, we varied the pulse energy to investigate the intensity dependence of strong-field ionization of Cs. The maximum pulse energy we had was about 27 μJ corresponding to a peak intensity of ≈ 4.2 TW/cm 2 as estimated by the cutoff of the spectrum. Due to limited experimental means during the beam time, we had to use a far-field iris to control the beam power. A change of the beam divergence introduced by the iris results in a nonlinear correlation between the pulse energy and the peak intensity. Figs. 7.5(a) and (b) show the measured ATI spectra for different CEPs at the maximum intensity we could achieve. The corresponding asymmetry map is shown in Fig. 7.5(c). A novel and intriguing feature of the asymmetry map is an anomalous energy-dependence and CEP-dependence compared to the now familiar asymmetry maps obtained with rare gases. Specifically, the CEP-dependent asymmetry at a certain energy oscillates faster than the variation of the CEP.

Here, we introduce a periodicity parameter, m_p , to describe the phase dependence.

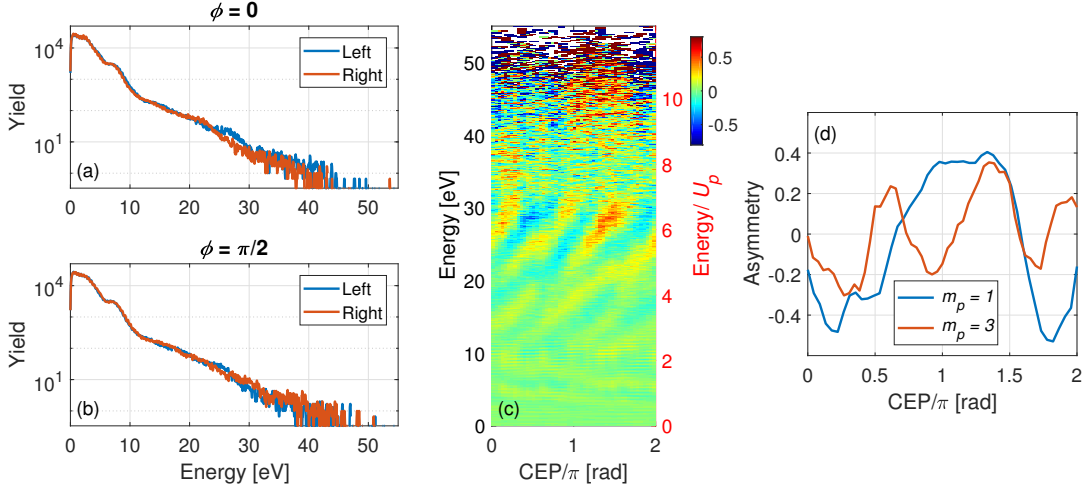


Figure 7.5: (a), (b) Measured ATI-spectra of Cs using 31 ± 0.5 -fs pulses at $3.2 \mu\text{m}$ with a peak intensity of $(4.2 \pm 0.2) \text{ TW}/\text{cm}^2$ for different CEPs. (c) The corresponding asymmetry map obtained from the measurements of (a) and (b). (d) The high-order ($m_p = 3$) CEP-dependence around 30 eV from the measurements is compared to the conventional $m_p = 1$ CEP-dependence near the cutoff (~ 45 eV). m_p is the periodicity parameter.

$m_p = 1$ corresponds to the familiar case where the asymmetry at an energy, E , varies with the same periodicity as the CEP. The general case then is

$$A(E) = A_0 \cos\left(\frac{\phi}{m_p} + \phi_0\right). \quad (7.1)$$

It is known that certain strong-field CEP-dependent phenomena, e.g. the photon yields for HHG [246, 247], total yields of double ionization [15, 212], or fragmentation [248] exhibit a periodicity of π with $m_p = 2$. This is no surprise as such total yields are mainly modulated by the instantaneous intensity, i.e., they do not depend on the direction of the field. In contrast, CEP effects with higher periodicity, i.e., $m_p > 2$ are rarely observed.

In Fig. 7.5(c), we observe quite a few unusual structures in the asymmetry map of Cs. These range from 10 eV ($\gtrsim 2 U_p$) to 40 eV ($\sim 10 U_p$), i.e., they lie in the ATI plateau region. One example at $E \approx 30$ eV is shown in Fig. 7.5(d). There the asymmetry oscillates with a periodicity of $\frac{2}{3}\pi$, resulting in a CEP-dependence with $m_p = 3$. We refer to this effect as a “high-order CEP-effect” [249]. In contrast, the same asymmetry map displays the regular CEP-dependence ($m_p = 1$) in the cutoff region around 45 eV, see Fig. 7.5(d).

Another observation is that the high-order CEP effect is only observed at high intensities, i.e., above $2 \text{ TW}/\text{cm}^2$. To address this issue, the asymmetry maps of Cs were

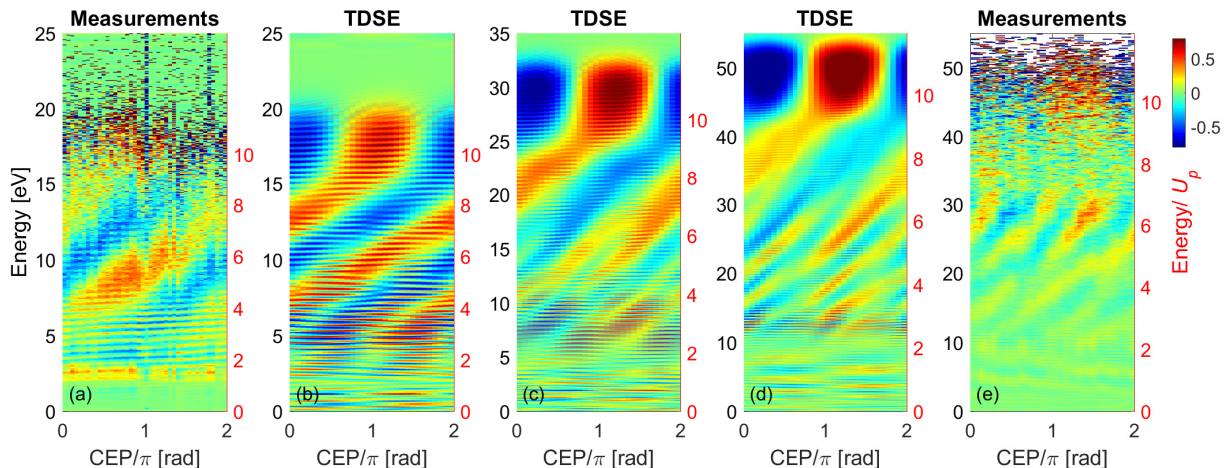


Figure 7.6: Comparison between the measurements and the TDSE results. (a) Measured asymmetry map of Cs using 31 ± 0.5 -fs pulses at $3.2 \mu\text{m}$ with a peak intensity of $(1.8 \pm 0.1) \text{ TW}/\text{cm}^2$. (b), (c) and (d) Calculated asymmetry maps of Cs with 30-fs pulses at $3.2 \mu\text{m}$ with peak intensities of $1.8 \text{ TW}/\text{cm}^2$, $3.0 \text{ TW}/\text{cm}^2$ and $4.4 \text{ TW}/\text{cm}^2$, respectively. (e) Measured asymmetry map of Cs using 31 ± 0.5 -fs pulses at $3.2 \mu\text{m}$ with a peak intensity of $(4.2 \pm 0.2) \text{ TW}/\text{cm}^2$.

computed by solving the TDSE for different intensities and compared to the measurements. The simulations also allow to follow the intensity-dependence in more details than possibilities in the experiments due to limited beamtime. In Fig. 7.6, panels (a) and (e) show the asymmetry maps of Cs measured at intensities of $1.8 \text{ TW}/\text{cm}^2$ and $4.2 \text{ TW}/\text{cm}^2$, respectively, and panels (b), (c), and (d) show the calculated asymmetry maps of Cs at intensities of $1.8 \text{ TW}/\text{cm}^2$, $3 \text{ TW}/\text{cm}^2$, and $4.4 \text{ TW}/\text{cm}^2$, respectively.

The numerical solutions of the TDSE verify two things: i) the very existence of the high-order CEP effect for Cs and ii) the fact that the anomalous effect only appears at high intensities. For further insight, we analyzed the intensity dependence of the ATI yield per laser shot and compared to the Perelomov-Popov-Terent'ev (PPT) ionization rate [136], see Fig. 7.7(b). Both, the measured intensity-dependent yield and the calculated ionization rate predicted by the PPT model, show the occurrence of saturation in the electron yield when the intensities exceed $2 \text{ TW}/\text{cm}^2$. Moreover, in Ref. [249], based on analyzing the survival probability of the atomic ground state of Cs obtained using solutions of the three-dimensional TDSE, the saturation effect is also estimated to become noticeable around $2 \text{ TW}/\text{cm}^2$. The hypothesis thus is that the high-order CEP-dependence exists in the saturation regime only. Further, we hypothesized that interference of electron

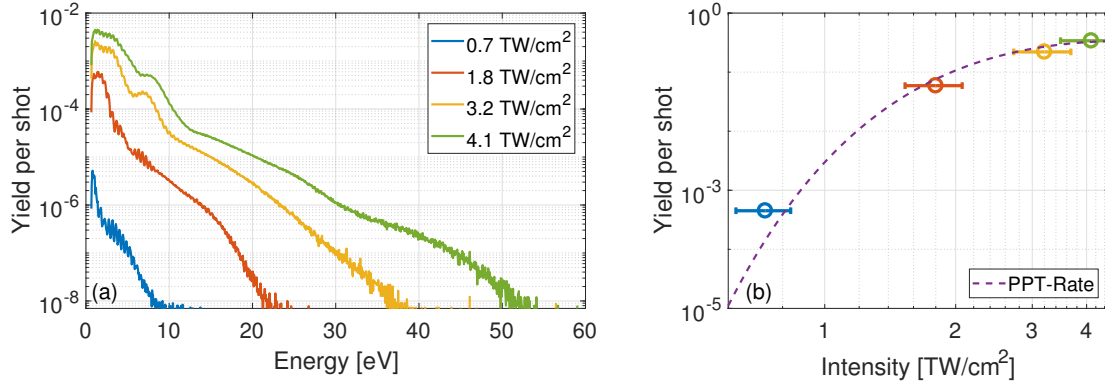


Figure 7.7: Intensity-dependent ATI spectra of Cs at 3.2 μm . (a) CEP-averaged ATI spectra of Cs measured at different laser intensities. (b) For each intensity in (a), the average number of electrons detected per laser shot is compared to the PPT-tunneling rate [136]. The peak intensity in the experiments is estimated by the $10U_p$ -cutoff in the ATI spectrum with an approximate 15% uncertainty.

trajectories may be at work.

In order to test these presumptions, a saddle-point analysis [12, 64, 250] was performed by the group of D. B. Milošević, University of Sarajevo. The saddle-point method delivers an approximation to the probability amplitude, M_p , for the transition of electrons from the initial state, $\psi_0(t')$, (i.e. the state before the laser arrives) to the final state, $\psi_p(t)$, of a continuum electron with drift momentum p :

$$M_p = \lim_{t \rightarrow \infty, t' \rightarrow -\infty} \langle \psi_p(t) | U_r(t, t') | \psi_0(t') \rangle, \quad (7.2)$$

where $U_r(t, t')$ is the time-evolution operator of the Hamiltonian, $H(t) = -\frac{1}{2m}\nabla^2 - e\mathbf{r}E(t) + V(\mathbf{r})$. After the transition to the continuum, the electron is only affected by the laser field, which is similar to the description by the three-step model. The eigenstates of the Schrödinger equation with a Hamiltonian without the atomic potential but with the laser field are known as Volkov states [64]:

$$| \psi_p^V(t) \rangle = | \mathbf{p} - e\mathbf{A}(t) \rangle e^{-iS_p(t)}, \quad (7.3)$$

with the classic action $S_p(t) = \frac{1}{2m} \int^t [\mathbf{p} - e\mathbf{A}(\tau)]^2 d\tau$, which represents the phase accumulated by the electron moving in the laser field.

The decisive step is to find the stationary conditions for the action, i.e., finding the saddle points: $\frac{\partial S_p(t)}{\partial t} = 0$. The discrete solutions of stationary phases correspond to the

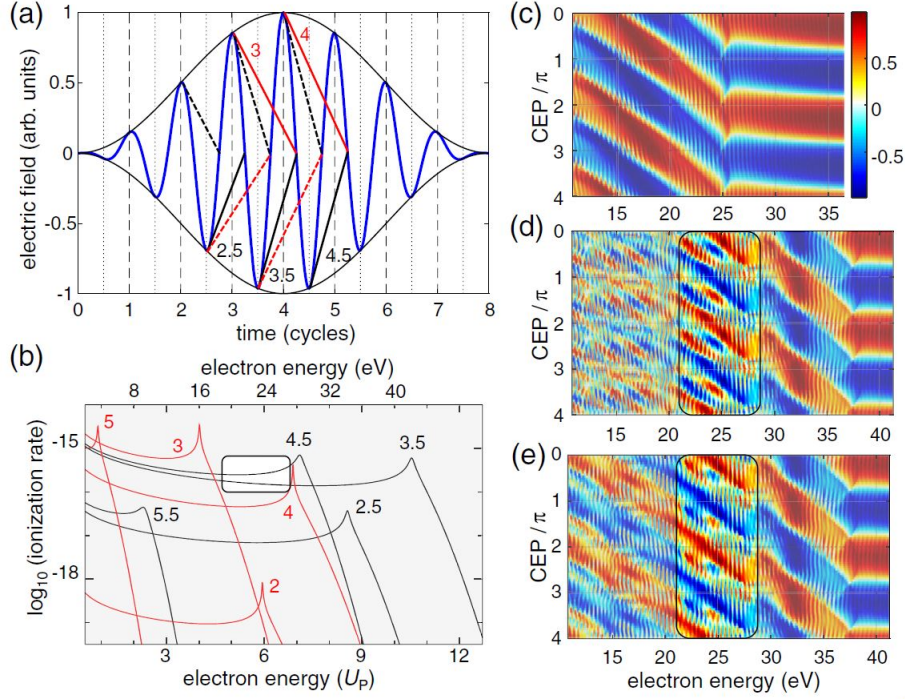


Figure 7.8: Quantum orbit analysis based on the saddle-point method [249]. (a) The laser field of a cosine-like pulse with CEP = 0 is plotted along with the most relevant quantum orbits where the emission time, t_0 , is connected with the recollision time, t_r . The solid and dashed lines correspond to quantum orbits with electron emission in positive and negative direction, respectively. Red integer values and black half-integer values correspond to long and short orbits, respectively that lead to positive drift momenta. (b) The electron yield is plotted as a function of electron kinetic energy for each quantum orbit. For the intensity of $4 \text{ TW}/\text{cm}^2$, the resulting CEP-dependent asymmetry map is plotted for (c) long orbits only, (d) short orbits only, and (e) all orbits. The black box mark the region with the most obvious high-order CEP effect.

so-called quantum orbits which can be understood as the quantum counterparts of the classical trajectories. The details of this method can be found in the supplementary material of Ref. [249].

Using the saddle-point method, quantum orbits with wave packets created at the maxima of each half-cycle of the electric field are obtained. The most important orbits (straight lines) are plotted into the electric field waveform of a few-cycle pulse with a CEP, $\phi = 0$, in Fig. 7.8(a). We distinguish short orbits for which rescattering takes place at the first return (with a travel time $\tau_{tr} = t_r - t_i$ less than one optical cycle) and long orbits where rescattering takes place at the second return (with travel time longer than one optical cycle). Orbits with even longer travel times are not considered. In Fig. 7.8(a),

the quantum orbits with electron emission in positive and negative direction are presented in solid and dashed lines, respectively. Red integer values and black half-integer values correspond to long and short orbits, respectively. For instance, the black solid line 3.5 represents the electrons that are ionized at a negative peak of the electric field, rescatter at the first return and are eventually emitted to the positive direction. Contrariwise, the red dashed line 3.5 represents electrons that are ionized at the same peak, but rescatter at the second return and escape to the negative direction.

Now we look at the contribution from each of the main quantum orbits to find out the reason for the high-order CEP dependence in the asymmetry. The electron yield for each orbit is plotted on the ponderomotive energy axis in Fig. 7.8(b). The most obvious high-order CEP-dependence we observed is around $6 - 7U_p$, where the short orbits 3.5 and 4.5 dominate with comparable yields.

For the intensity of 4 TW/cm^2 , asymmetry maps for long orbits only, short orbits only, and combination of both are plotted in Figs. 7.8(c), (d), and (e), respectively. The absence of high-order oscillations in the asymmetry map for long orbits only indicates that the $m_p = 3$ CEP-dependence is due to the contributions from the short orbits only, and *not* an effect of interference between long and short trajectories. On the other hand, in the asymmetry map only for short orbits, the high-order oscillation dominates almost the entire energy region of rescattering, except for the region near the cutoff. With combining both asymmetry maps [see Fig. 7.8(e)], it can be seen that the fast oscillations still remain on top of the normal $m_p = 1$ oscillation.

In general, from the quantum orbit theory, the $m_p = 3$ CEP-dependence can be interpreted as the interference between two quantum orbits from adjacent cycles. In our case for instance, the most obvious high-order CEP-effect around $6 - 7U_p$ is a consequence of interference between the orbits 3.5 and 4.5. Normally, interference of electron emission from adjacent optical cycles results in the well-known series of ATI peaks. The situation here is different due to the fact that the amplitude of adjacent cycles varies noticeable for few-cycle pulses, e.g., 2.8 cycles in our case. On the other hand, the pulses are not so short that the emission of the strongest cycle dominates such that the interference contrast is lost. This interpretation will further be supported by Fig. 7.10 in the next section.

7.3 Discussions

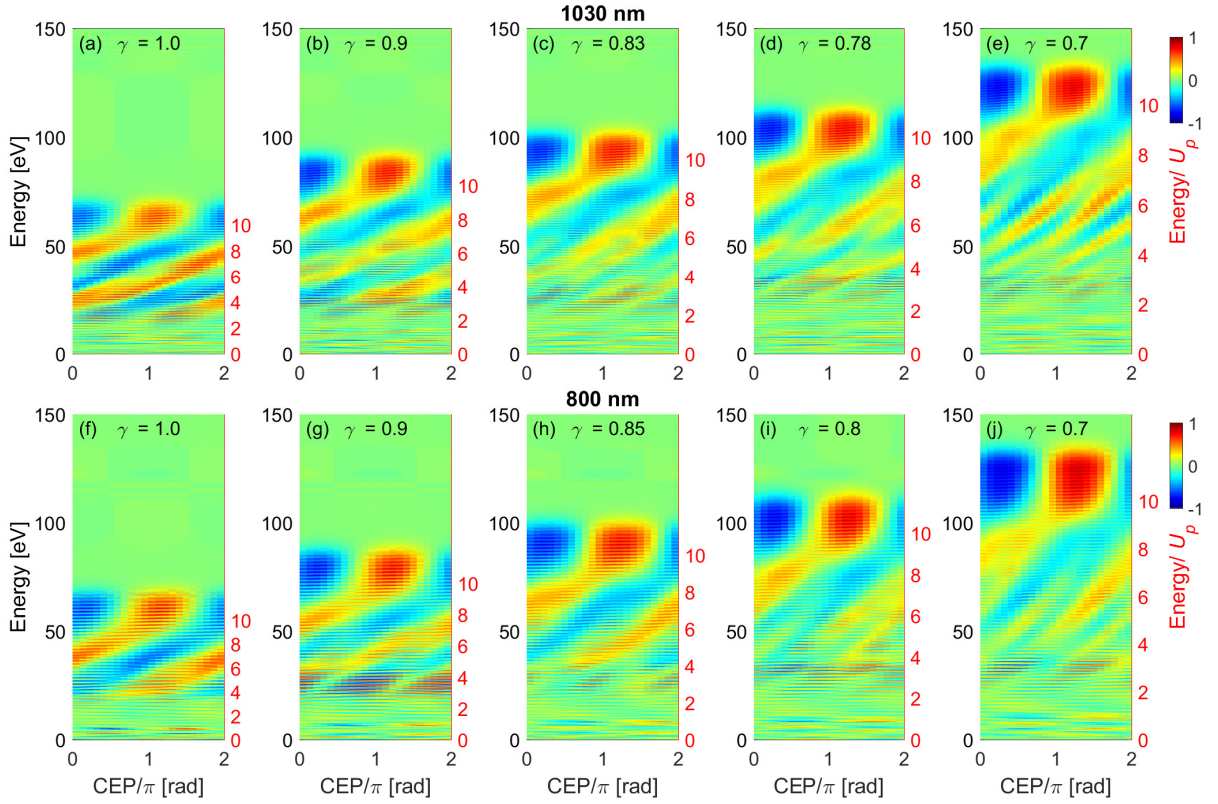


Figure 7.9: Series of computed asymmetry maps of Xe for 800 nm and 1030 nm while the number of optical cycles of the pulses is kept constant. (a) - (e) Asymmetry maps of Xe for 1030 nm. The pulse length is 10 fs (~ 3 cycles). The peak intensities are 0.6, 0.76, 0.9, 1.0, and 1.25×10^{14} W/cm², respectively. (f) - (j) Asymmetry maps of Xe for 800 nm. The pulse length is 8 fs (~ 3 cycles). The peak intensities are 1.0, 1.25, 1.4, 1.6, and 2.0×10^{14} W/cm², respectively.

Since the high-order asymmetries can be interpreted as interference between two quantum orbits within two adjacent cycles, the question remains why high-order asymmetries have not been observed in previous experiments. As already noticed, a simple but important aspect is that the intensity in previous experiments was not high enough. The intensity at which we observed the high-order effects in Cs is two times the intensity where the saturation occurs. We have also presented evidence that interference of photoelectron emission from subsequent optical cycles is at work. Here, we present further data corroborating this explanation and add the aspect that saturation enhances the contrast of the interference patterns because saturation leads to comparable yields for the two orbits. To this end, we solve the TDSE to calculate ATI spectra of Xe at different wavelengths with

different intensities.

Solving the TDSE for MIR wavelength can be quite tedious even on modern computers. However, in Ref. [251], an improved 1D-TDSE was derived to exploit the scaling freedom of the laser field strength and the ionization energy. The result demonstrates a direct estimation that if i) the field strength to ionization energy ratio and ii) the ionization energy to photon energy ratio are the same, the light-matter interactions are predicted to have the same outcomes. The photon energy of 3.2 μm is approximately 0.39 eV and the ionization energy for the ground state electron of Cs about 3.89 eV. Thus, the corresponding ionization energy to photon energy ratio is roughly about 10. This matches the combination of 1030 nm (photon energy: 1.2 eV) and Xe in the ground state (ionization energy: 12.13 eV). To end up at 1030 nm is advantageous as this is the typical wavelength of Yb-lasers, i.e. our theoretical treatment can easily be verified experimentally in the future.

The calculated asymmetry maps of Xe at 1030 nm are presented in Figs. 7.9(a) - (e). We can see that the $m_p = 3$ CEP-dependence appears at intensities higher than $0.85 \times 10^{14} \text{ W/cm}^2$ with $\gamma < 0.85$, which is in good agreement with the case of Cs. At intensities below $0.8 \times 10^{14} \text{ W/cm}^2$ ($\gamma \gtrsim 0.9$), only the $m_p = 1$ CEP dependence is observed.

Moreover, we present the asymmetry map of Xe at 800 nm with different intensities in Fig. 7.9(f) - (j), where the ionization energy to photon energy ratio is changed. Nevertheless, the high-order CEP-effect is still predicted by the simulation at high intensities. This proves that this anomalous high-order CEP-dependence in the plateau region of the ATI spectrum is a universal effect, the principle existence of which neither depends on the type of atom nor on the wavelength of the field. In addition, with combining the analysis of all results from Cs and Xe at different wavelengths, we found that the $m_p = 3$ CEP-dependence generally emerges for $\gamma \lesssim 0.85$ and vanishes for $\gamma \gtrsim 0.9$.

With respect to our conjecture on the dependence on pulse duration, we also performed respective simulations. In Fig. 7.10, the asymmetry maps of Cs calculated by solving the TDSE with 3.2- μm pulses at an intensity of 4.4 TW/cm^2 for different pulse lengths are compared. It can be seen that the high-order CEP-effect fades away at 20 fs (~ 2 optical cycles) and vanishes at 15 fs (~ 1.5 optical cycles). Accordingly, this effect becomes visible and more obvious when the pulse length is longer than 2 optical cycles. On the other

hand, of course, in order to observe a CEP-dependence at all, the pulse duration cannot be too long, i.e., not longer than 4 optical cycles.

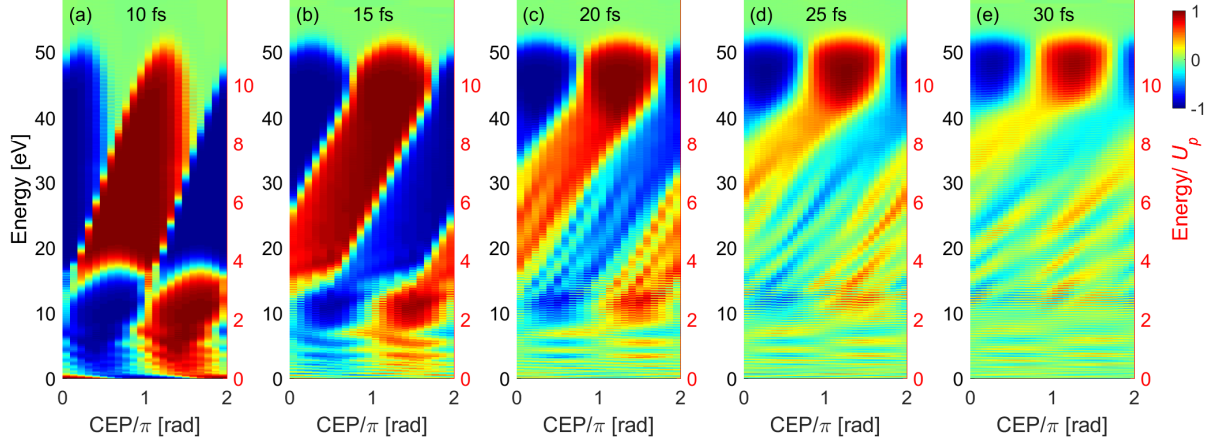


Figure 7.10: Pulse length-dependent asymmetry map of Cs obtained by the TDSE calculation. The center wavelength is $3.2\ \mu\text{m}$ and the peak intensity is $4.4\ \text{TW}/\text{cm}^2$. One optical cycle at $3.2\ \mu\text{m}$ is around 11 fs. (a) - (e) Asymmetry maps with $\sim 0.9, 1.4, 1.9, 2.3$ and 2.8 optical cycles, respectively.

Chapter 8

Summary and Outlook

In this thesis, we investigated carrier-envelope phase (CEP)-dependent strong-field ionization phenomena in atomic systems from the near-infrared (NIR) to the short-wave infrared (SWIR) and further to the mid-infrared (MIR) regime. The main results are: i) Single-shot CEP measurement with a carrier-envelope phasemeter (CEPM) at SWIR wavelength, ii) The analysis of the phase-volume effect of broadband pulses in CEP-dependent light-matter interactions and iii) The observation of high-order CEP-dependent effects in strong-field experiments with alkali atoms in the MIR range.

Specifically, the CEP of 1.8- μm laser pulses was characterized for every individual laser shot at 1 kHz pulse repetition rate. A precision of the CEP measurement of 120 mrad was achieved. As a distinctive advantage of the CEPM, the pulse lengths of 1.8 μm few-cycle pulses were simultaneously characterized by analyzing the amplitude of the spectral asymmetry in the direction of photoelectron emission. The capability of single-shot phase measurement was confirmed and exploited by implementing so-called phase-tagging experiments, where the CEP-dependence of strong-field effects could be measured despite the randomly varying CEP of the laser pulses. This was achieved by correlating the events of the respective experiments (here a high-resolution photoelectron spectrometer) with the output of a CEPM. Simulation results from two models, a semi-classic three-step model and the numerical solution of the time-dependent Schrödinger equation, were compared to the experimental results. The agreement between both validates our measurements and theoretical treatments. Further analysis, has yielded a quantitative criterion for achieving single-shot CEP measurement with a CEPM.

The comparison of experimental and theoretical results led to the finding of a system-

atic deviation that originates in neglecting or underestimating the spatial phase distribution of a focused broadband pulse. The direct consequence of the inevitable averaging over the phase distribution is that the contrast of the CEP-dependence will be partially averaged out.

By considering the phase distribution in addition to the intensity-dependent yield averaged across the focus, the quantitative differences between the Gouy phase and the focal phase in light-matter interactions are analyzed. We noticed that considering the Gouy phase only is insufficient to precisely describe the CEP-dependence. Only when the theoretical analysis includes the more realistic phase distribution in the focus, a better agreement with the measurements can be obtained. This finding has direct consequences for measuring the pulse duration with a CEPM. If calibrated against insufficiently detailed simulations, the CEPM would predict longer pulses than actually present. The same effect can be observed at, e.g., 800 nm.

It should be noticed that our experiments have concentrated on the highly nonlinear physical processes typical for strong-field ionization of, e.g., xenon. As long as saturation does not play a strong role, the high nonlinearity actually limits the averaging effects because the yield from the regions in the focus with the highest intensity will dominate. This can be quite different for processes with lower nonlinearities such as molecular dissociation or multiphoton absorption. There, the larger effective interaction volume can increase the averaging effect thus washing out the CEP dependence. We therefore generalized and quantified this effect for a broad range of few-cycle light-matter interaction scenarios. In this way, the question if, when, and how much one should be concerned about the focal phase can be answered.

Following the spirit of extending the regime towards longer wavelengths, we discussed CEP-dependent strong-field phenomena in the MIR range (3.2 μm). First, as a benchmark measurement, the CEP-dependence of ATI spectra of xenon was measured. Next, by averaging over 500 laser shots, the CEP of MIR few-cycle pulses was measured with a Xe-based CEPM with a precision of 165 mrad. The results prove our understanding of the scaling of strong-field ionization with wavelength for single-shot CEP measurements with a CEPM. If one wants to measure the CEP with a Xe-CEPM in single-shot operation, a pulse energy of tens of mJ is required in the MIR to compensate the lower yield of rescattered electrons that follows from basic principles the ATI plateau.

The desire of a more promising target atom for a MIR-CEPM and scientific curiosity provoked the investigation of the CEP-dependence of above-threshold ionization of caesium. Surprisingly, a high-order CEP-dependence was observed, i.e., a variation of the asymmetry three times as fast as the variation of the CEP. An analysis based on quantum orbit theory shows that this high-order CEP-dependence can be understood as the interference of two backscattering quantum orbits from adjacent optical cycles. In particular, this effect only takes place at very high intensities, which can be interpreted as the impact from the saturation of the ionization, where the yields from two orbits are comparable leading to an enhancement of the interference. We also found that the effect can only be observed for pulses that are not too short and not too long: On the one hand, the emission from both cycles need to be comparable to afford sufficient interference contrast. On the other hand, the amplitude of both cycles should differ sufficiently, otherwise the CEP-dependence would disappear and the interferences degenerate into a regular ATI spectrum.

In the future, more studies regarding the issues discussed in this thesis can and should be performed. First, the phase-volume effect in the MIR range has not been analyzed. The much bigger amplitude in the asymmetry map in our simulations already gives a strong hint that the phase-averaging effect is quite significant due to the extreme broad spectral bandwidth in MIR range and the spectral divergence caused by the post-compression techniques often used for this kind of laser systems.

We have demonstrated that the yield of plateau electrons generated from Cs at MIR wavelengths is comparable or even larger than in the case of Xe in the NIR range. Thus, the door for implementing a single-shot CEPM for long wavelengths based on the measurement of stereo-ATI from alkali atoms is open and eventually should lead to a respective instrument. The high-order CEP effect is not a showstopper because it only occurs at high intensities, while the electron yield at lower intensities is still sufficient for single-shot CEP measurement. The development of high-power, CEP-stable, few-cycle MIR laser systems quite likely will lead to the discovery of many new effects. I hope that this thesis has made and will make a useful contribution to this development.

Reference

- [1] T. Brabec and F. Krausz. Intense few-cycle laser fields: Frontiers of nonlinear optics. *Reviews of Modern Physics*, **72**(2):545, 2000.
- [2] A. de Bohan, P. Antoine, D. B. Milošević, and B. Piraux. Phase-dependent harmonic emission with ultrashort laser pulses. *Physical review letters*, **81**(9):1837, 1998.
- [3] M. Nisoli, G. Sansone, S. Stagira, S. De Silvestri, C. Vozzi, M. Pascolini, L. Poletto, P. Villoresi, and G. Tondello. Effects of carrier-envelope phase differences of few-optical-cycle light pulses in single-shot high-order-harmonic spectra. *Physical review letters*, **91**(21):213905, 2003.
- [4] N. Ishii, K. Kaneshima, K. Kitano, T. Kanai, S. Watanabe, and J. Itatani. Carrier-envelope phase-dependent high harmonic generation in the water window using few-cycle infrared pulses. *Nature Communications*, **5**(1):1–6, 2014.
- [5] M. Kreß, T. Löffler, M. D. Thomson, R. Dörner, H. Gimpel, K. Zrost, T. Ergler, R. Moshhammer, U. Morgner, J. Ullrich, et al. Determination of the carrier-envelope phase of few-cycle laser pulses with terahertz-emission spectroscopy. *Nature physics*, **2**(5):327–331, 2006.
- [6] H.-C. Wu, J. Meyer-ter Vehn, and Z.-M. Sheng. Phase-sensitive terahertz emission from gas targets irradiated by few-cycle laser pulses. *New Journal of Physics*, **10**(4):043001, 2008.
- [7] Y. Bai, L. Song, R. Xu, C. Li, P. Liu, Z. Zeng, Z. Zhang, H. Lu, R. Li, and Z. Xu. Waveform-controlled terahertz radiation from the air filament produced by few-cycle laser pulses. *Physical review letters*, **108**(25):255004, 2012.
- [8] G. Sansone, E. Benedetti, F. Calegari, C. Vozzi, L. Avaldi, R. Flammini, L. Poletto, P. Villoresi, C. Altucci, R. Velotta, et al. Isolated single-cycle attosecond pulses. *Science*, **314**(5798):443–446, 2006.
- [9] F. Ferrari, F. Calegari, M. Lucchini, C. Vozzi, S. Stagira, G. Sansone, and M. Nisoli. High-energy isolated attosecond pulses generated by above-saturation few-cycle fields. *Nature Photonics*, **4**(12):875–879, 2010.
- [10] M. Chini, K. Zhao, and Z. Chang. The generation, characterization and applications of broadband isolated attosecond pulses. *Nature Photonics*, **8**(3):178–186, 2014.
- [11] G. Paulus, F. Grasbon, H. Walther, P. Villoresi, M. Nisoli, S. Stagira, E. Priori, and S. De Silvestri. Absolute-phase phenomena in photoionization with few-cycle laser pulses. *Nature*, **414**(6860):182–184, 2001.
- [12] D. Milošević, G. Paulus, D. Bauer, and W. Becker. Above-threshold ionization by few-cycle pulses. *Journal of Physics B: Atomic, Molecular and Optical Physics*, **39**(14):R203, 2006.
- [13] X. Liu, H. Rottke, E. Eremina, W. Sandner, E. Goulielmakis, K. O. Keeffe, M. Lezius, F. Krausz, F. Lindner, M. G. Schätzel, et al. Nonsequential double ionization at the single-optical-cycle limit. *Physical review letters*, **93**(26):263001, 2004.
- [14] X. Tong, K. Hino, and N. Toshima. Phase-dependent atomic ionization in few-cycle intense laser fields. *Physical Review A*, **74**(3):031405, 2006.
- [15] N. G. Johnson, O. Herrwerth, A. Wirth, S. De, I. Ben-Itzhak, M. Lezius, B. Bergues, M. F. Kling, A. Senftleben, C. D. Schröter, et al. Single-shot carrier-envelope-phase-tagged ion-momentum imaging of nonsequential double ionization of argon in intense 4-fs laser fields. *Physical Review A*, **83**(1):013412, 2011.

- [16] W. Becker, X. Liu, P. J. Ho, and J. H. Eberly. Theories of photoelectron correlation in laser-driven multiple atomic ionization. *Reviews of Modern Physics*, **84**(3):1011, 2012.
- [17] D. Zille, D. Adolph, M. Möller, A. Sayler, and G. Paulus. Chirp and carrier-envelope-phase effects in the multiphoton regime: measurements and analytical modeling of strong-field ionization of sodium. *New Journal of Physics*, **20**(6):063018, 2018.
- [18] M. Kling, C. Siedschlag, A. J. Verhoef, J. Khan, M. Schultze, T. Uphues, Y. Ni, M. Uiberacker, M. Drescher, F. Krausz, et al. Control of electron localization in molecular dissociation. *Science*, **312**(5771):246–248, 2006.
- [19] X. Tong and C. Lin. Dynamics of light-field control of molecular dissociation at the few-cycle limit. *Physical review letters*, **98**(12):123002, 2007.
- [20] J. McKenna, A. Sayler, F. Anis, B. Gaire, N. G. Johnson, E. Parke, J. Hua, H. Mashiko, C. Nakamura, E. Moon, et al. Enhancing high-order above-threshold dissociation of $h\ 2+$ beams with few-cycle laser pulses. *Physical review letters*, **100**(13):133001, 2008.
- [21] M. Kremer, B. Fischer, B. Feuerstein, V. L. de Jesus, V. Sharma, C. Hofrichter, A. Rudenko, U. Thumm, C. D. Schröter, R. Moshhammer, et al. Electron localization in molecular fragmentation of $h\ 2$ by carrier-envelope phase stabilized laser pulses. *Physical review letters*, **103**(21):213003, 2009.
- [22] B. Bergues, M. Kübel, N. G. Johnson, B. Fischer, N. Camus, K. J. Betsch, O. Herrwerth, A. Sentsleben, A. M. Sayler, T. Rathje, et al. Attosecond tracing of correlated electron-emission in non-sequential double ionization. *Nature communications*, **3**(1):1–6, 2012.
- [23] N. G. Kling, K. Betsch, M. Zohrabi, S. Zeng, F. Anis, U. Ablikim, B. Jochim, Z. Wang, M. Kübel, M. F. Kling, et al. Carrier-envelope phase control over pathway interference in strong-field dissociation of $h\ 2+$. *Physical review letters*, **111**(16):163004, 2013.
- [24] M. Kübel, R. Siemering, C. Burger, N. G. Kling, H. Li, A. Alnaser, B. Bergues, S. Zhrebtsov, A. Azzeer, I. Ben-Itzhak, et al. Steering proton migration in hydrocarbons using intense few-cycle laser fields. *Physical Review Letters*, **116**(19):193001, 2016.
- [25] T. Fortier, P. Roos, D. Jones, S. T. Cundiff, R. Bhat, and J. Sipe. Carrier-envelope phase-controlled quantum interference of injected photocurrents in semiconductors. *Physical review letters*, **92**(14):147403, 2004.
- [26] O. Schubert, M. Hohenleutner, F. Langer, B. Urbanek, C. Lange, U. Huttner, D. Golde, T. Meier, M. Kira, S. W. Koch, et al. Sub-cycle control of terahertz high-harmonic generation by dynamical bloch oscillations. *Nature Photonics*, **8**(2):119–123, 2014.
- [27] Y. S. You, M. Wu, Y. Yin, A. Chew, X. Ren, S. Gholam-Mirzaei, D. A. Browne, M. Chini, Z. Chang, K. J. Schafer, et al. Laser waveform control of extreme ultraviolet high harmonics from solids. *Optics letters*, **42**(9):1816–1819, 2017.
- [28] M. Garg, H.-Y. Kim, and E. Goulielmakis. Ultimate waveform reproducibility of extreme-ultraviolet pulses by high-harmonic generation in quartz. *Nature Photonics*, **12**(5):291–296, 2018.
- [29] G. Paulus, W. Nicklich, H. Xu, P. Lambropoulos, and H. Walther. Plateau in above threshold ionization spectra. *Physical review letters*, **72**(18):2851, 1994.
- [30] T. Wittmann, B. Horvath, W. Helml, M. G. Schätzkel, X. Gu, A. L. Cavalieri, G. Paulus, and R. Kienberger. Single-shot carrier-envelope phase measurement of few-cycle laser pulses. *Nature Physics*, **5**(5):357–362, 2009.
- [31] A. Sayler, T. Rathje, W. Müller, K. Rühle, R. Kienberger, and G. Paulus. Precise, real-time, every-single-shot, carrier-envelope phase measurement of ultrashort laser pulses. *Optics letters*, **36**(1):1–3, 2011.
- [32] A. Sayler, T. Rathje, W. Müller, C. Kürbis, K. Rühle, G. Stibenz, and G. Paulus. Real-time pulse length measurement of few-cycle laser pulses using above-threshold ionization. *Optics express*, **19**(5):4464–4471, 2011.

- [33] T. Rathje, N. G. Johnson, M. Möller, F. Süßmann, D. Adolph, M. Kübel, R. Kienberger, M. F. Kling, G. Paulus, and A. Sayler. Review of attosecond resolved measurement and control via carrier-envelope phase tagging with above-threshold ionization. *Journal of Physics B: Atomic, Molecular and Optical Physics*, **45**(7):074003, 2012.
- [34] T. Popmintchev, M.-C. Chen, A. Bahabad, M. Gerrity, P. Sidorenko, O. Cohen, I. P. Christov, M. M. Murnane, and H. C. Kapteyn. Phase matching of high harmonic generation in the soft and hard x-ray regions of the spectrum. *Proceedings of the National Academy of Sciences*, **106**(26):10516–10521, 2009.
- [35] B. E. Schmidt, A. D. Shiner, M. Giguère, P. Lassonde, C. A. Trallero-Herrero, J. Kieffer, P. Corkum, D. Villeneuve, and F. Légaré. High harmonic generation with long-wavelength few-cycle laser pulses. *Journal of Physics B: Atomic, Molecular and Optical Physics*, **45**(7):074008, 2012.
- [36] T. Popmintchev, M.-C. Chen, D. Popmintchev, P. Arpin, S. Brown, S. Ališauskas, G. Andriukaitis, T. Balčiunas, O. D. Mücke, A. Pugzlys, et al. Bright coherent ultrahigh harmonics in the kev x-ray regime from mid-infrared femtosecond lasers. *science*, **336**(6086):1287–1291, 2012.
- [37] G. J. Stein, P. D. Keathley, P. Krogen, H. Liang, J. P. Siqueira, C.-L. Chang, C.-J. Lai, K.-H. Hong, G. M. Laurent, and F. X. Kärtner. Water-window soft x-ray high-harmonic generation up to the nitrogen k-edge driven by a khz, 2.1 μm opepa source. *Journal of Physics B: Atomic, Molecular and Optical Physics*, **49**(15):155601, 2016.
- [38] A. S. Johnson, D. R. Austin, D. A. Wood, C. Brahms, A. Gregory, K. B. Holzner, S. Jarosch, E. W. Larsen, S. Parker, C. S. Strüber, et al. High-flux soft x-ray harmonic generation from ionization-shaped few-cycle laser pulses. *Science Advances*, **4**(5):eaar3761, 2018.
- [39] X. Ren, J. Li, Y. Yin, K. Zhao, A. Chew, Y. Wang, S. Hu, Y. Cheng, E. Cunningham, Y. Wu, et al. Attosecond light sources in the water window. *Journal of Optics*, **20**(2):023001, 2018.
- [40] M.-C. Chen, C. Mancuso, C. Hernández-García, F. Dollar, B. Galloway, D. Popmintchev, P.-C. Huang, B. Walker, L. Plaja, A. A. Jaroń-Becker, et al. Generation of bright isolated attosecond soft x-ray pulses driven by multicycle midinfrared lasers. *Proceedings of the National Academy of Sciences*, **111**(23):E2361–E2367, 2014.
- [41] T. Gaumnitz, A. Jain, Y. Pertot, M. Huppert, I. Jordan, F. Ardana-Lamas, and H. J. Wörner. Streaking of 43-attosecond soft-x-ray pulses generated by a passively cep-stable mid-infrared driver. *Optics express*, **25**(22):27506–27518, 2017.
- [42] C. Blaga, F. Catoire, P. Colosimo, G. Paulus, H. Muller, P. Agostini, and L. DiMauro. Strong-field photoionization revisited. *Nature Physics*, **5**(5):335–338, 2009.
- [43] W. Quan, Z. Lin, M. Wu, H. Kang, H. Liu, X. Liu, J. Chen, J. Liu, X. He, S. Chen, et al. Classical aspects in above-threshold ionization with a midinfrared strong laser field. *Physical review letters*, **103**(9):093001, 2009.
- [44] T.-M. Yan, S. Popruzhenko, M. Vrakking, and D. Bauer. Low-energy structures in strong field ionization revealed by quantum orbits. *Physical review letters*, **105**(25):253002, 2010.
- [45] M. Möller, F. Meyer, A. Sayler, G. Paulus, M. F. Kling, B. Schmidt, W. Becker, and D. Milošević. Off-axis low-energy structures in above-threshold ionization. *Physical Review A*, **90**(2):023412, 2014.
- [46] B. Wolter, C. Lemell, M. Baudisch, M. G. Pullen, X.-M. Tong, M. Hemmer, A. Senftleben, C. D. Schröter, J. Ullrich, R. Moshhammer, et al. Formation of very-low-energy states crossing the ionization threshold of argon atoms in strong mid-infrared fields. *Physical Review A*, **90**(6):063424, 2014.
- [47] Q. Xia, D. Ye, L. Fu, X. Han, and J. Liu. Momentum distribution of near-zero-energy photoelectrons in the strong-field tunneling ionization in the long wavelength limit. *Scientific reports*, **5**:11473, 2015.
- [48] P. Colosimo, G. Doumy, C. Blaga, J. Wheeler, C. Hauri, F. Catoire, J. Tate, R. Chirila, A. March, G. Paulus, et al. Scaling strong-field interactions towards the classical limit. *Nature Physics*, **4**(5):386–389, 2008.

- [49] C. I. Blaga, J. Xu, A. D. DiChiara, E. Sistrunk, K. Zhang, P. Agostini, T. A. Miller, L. F. DiMauro, and C. Lin. Imaging ultrafast molecular dynamics with laser-induced electron diffraction. *Nature*, **483**(7388):194–197, 2012.
- [50] H. Ibrahim, C. Lefebvre, A. D. Bandrauk, A. Staudte, and F. Légaré. H₂: the benchmark molecule for ultrafast science and technologies. *Journal of Physics B: Atomic, Molecular and Optical Physics*, **51**(4):042002, 2018.
- [51] S. Backus, C. G. Durfee III, M. M. Murnane, and H. C. Kapteyn. High power ultrafast lasers. *Review of scientific instruments*, **69**(3):1207–1223, 1998.
- [52] U. Keller. Ultrafast solid-state laser oscillators: a success story for the last 20 years with no end in sight. *Applied Physics B*, **100**(1):15–28, 2010.
- [53] D. J. Richardson, J. Nilsson, and W. A. Clarkson. High power fiber lasers: current status and future perspectives. *JOSA B*, **27**(11):B63–B92, 2010.
- [54] H. Fattahi, H. G. Barros, M. Gorjan, T. Nubbemeyer, B. Alsaif, C. Y. Teisset, M. Schultze, S. Prinz, M. Haefner, M. Ueffing, et al. Third-generation femtosecond technology. *Optica*, **1**(1):45–63, 2014.
- [55] M. N. Zervas and C. A. Codemard. High power fiber lasers: a review. *IEEE Journal of selected topics in Quantum Electronics*, **20**(5):219–241, 2014.
- [56] B. W. Tilma, M. Mangold, C. A. Zaugg, S. M. Link, D. Waldburger, A. Klenner, A. S. Mayer, E. Gini, M. Golling, and U. Keller. Recent advances in ultrafast semiconductor disk lasers. *Light: Science & Applications*, **4**(7):e310–e310, 2015.
- [57] M. E. Fermann, A. Galvanauskas, and G. Sucha. *Ultrafast lasers: technology and applications*, volume 80. CRC Press, 2002.
- [58] F. Dausinger and F. Lichtner. *Femtosecond technology for technical and medical applications*, volume 96. Springer Science & Business Media, 2004.
- [59] J.-C. Diels and W. Rudolph. *Ultrashort laser pulse phenomena*. Elsevier, 2006.
- [60] M. Malinauskas, A. Žukauskas, S. Hasegawa, Y. Hayasaki, V. Mizeikis, R. Buividas, and S. Juodkazis. Ultrafast laser processing of materials: from science to industry. *Light: Science & Applications*, **5**(8):e16133–e16133, 2016.
- [61] P. Agostini, F. Fabre, G. Mainfray, G. Petite, and N. K. Rahman. Free-free transitions following six-photon ionization of xenon atoms. *Physical Review Letters*, **42**(17):1127, 1979.
- [62] R. Freeman, P. Bucksbaum, H. Milchberg, S. Darack, D. Schumacher, and M. Geusic. Above-threshold ionization with subpicosecond laser pulses. *Physical review letters*, **59**(10):1092, 1987.
- [63] P. Corkum, N. Burnett, and F. Brunel. Above-threshold ionization in the long-wavelength limit. *Physical review letters*, **62**(11):1259, 1989.
- [64] W. Becker, F. Grasbon, R. Kopold, D. Milošević, G. Paulus, and H. Walther. Above-threshold ionization: From classical features to quantum effects. *AAMOP*, **48**:35–98, 2002.
- [65] A. McPherson, G. Gibson, H. Jara, U. Johann, T. S. Luk, I. McIntyre, K. Boyer, and C. K. Rhodes. Studies of multiphoton production of vacuum-ultraviolet radiation in the rare gases. *JOSA B*, **4**(4):595–601, 1987.
- [66] J. L. Krause, K. J. Schafer, and K. C. Kulander. High-order harmonic generation from atoms and ions in the high intensity regime. *Physical Review Letters*, **68**(24):3535, 1992.
- [67] A. L’Huillier and P. Balcou. High-order harmonic generation in rare gases with a 1-ps 1053-nm laser. *Physical Review Letters*, **70**(6):774, 1993.
- [68] F. Krausz and M. Ivanov. Attosecond physics. *Rev. Mod. Phys.*, **81**:163–234, Feb 2009.
- [69] P. Antoine, A. L’huillier, and M. Lewenstein. Attosecond pulse trains using high-order harmonics. *Physical Review Letters*, **77**(7):1234, 1996.
- [70] P. á. Corkum and F. Krausz. Attosecond science. *Nature physics*, **3**(6):381–387, 2007.
- [71] A. l’Huillier, L. Lompre, G. Mainfray, and C. Manus. Multiply charged ions induced by multiphoton absorption in rare gases at 0.53 μm . *Physical Review A*, **27**(5):2503, 1983.

- [72] D. N. Fittinghoff, P. R. Bolton, B. Chang, and K. C. Kulander. Observation of nonsequential double ionization of helium with optical tunneling. *Physical review letters*, **69**(18):2642, 1992.
- [73] J. Watson, A. Sanpera, D. Lappas, P. Knight, and K. Burnett. Nonsequential double ionization of helium. *Physical review letters*, **78**(10):1884, 1997.
- [74] A. Buck, M. Nicolai, K. Schmid, C. M. Sears, A. Sävert, J. M. Mikhailova, F. Krausz, M. C. Kaluza, and L. Veisz. Real-time observation of laser-driven electron acceleration. *Nature Physics*, **7**(7):543–548, 2011.
- [75] A. J. Lind, A. Kowligy, H. Timmers, F. C. Cruz, N. Nader, M. C. Silfies, T. K. Allison, and S. A. Diddams. Mid-infrared frequency comb generation and spectroscopy with few-cycle pulses and χ (2) nonlinear optics. *Physical Review Letters*, **124**(13):133904, 2020.
- [76] J. J. Carrera and S.-I. Chu. Extension of high-order harmonic generation cutoff via coherent control of intense few-cycle chirped laser pulses. *Physical Review A*, **75**(3):033807, 2007.
- [77] M. Frolov, N. Manakov, A. Popov, O. Tikhonova, E. Volkova, A. Silaev, N. Vvedenskii, and A. F. Starace. Analytic theory of high-order-harmonic generation by an intense few-cycle laser pulse. *Physical Review A*, **85**(3):033416, 2012.
- [78] Y. Wu and X. Yang. Carrier-envelope phase-dependent atomic coherence and quantum beats. *Physical Review A*, **76**(1):013832, 2007.
- [79] V. Roudnev, B. Esry, and I. Ben-Itzhak. Controlling h d+ and h 2+ dissociation with the carrier-envelope phase difference of an intense ultrashort laser pulse. *Physical review letters*, **93**(16):163601, 2004.
- [80] R. Atanasov, A. Haché, J. Hughes, H. Van Driel, and J. Sipe. Coherent control of photocurrent generation in bulk semiconductors. *Physical review letters*, **76**(10):1703, 1996.
- [81] A. Haché, Y. Kostoulas, R. Atanasov, J. Hughes, J. Sipe, and H. Van Driel. Observation of coherently controlled photocurrent in unbiased, bulk gaas. *Physical Review Letters*, **78**(2):306, 1997.
- [82] M. Korbman, S. Y. Kruchinin, and V. S. Yakovlev. Quantum beats in the polarization response of a dielectric to intense few-cycle laser pulses. *New Journal of Physics*, **15**(1):013006, 2013.
- [83] T. Paasch-Colberg, S. Y. Kruchinin, Ö. Sağlam, S. Kapser, S. Cabrini, S. Muehlbrandt, J. Reichert, J. V. Barth, R. Ernstorfer, R. Kienberger, et al. Sub-cycle optical control of current in a semiconductor: from the multiphoton to the tunneling regime. *Optica*, **3**(12):1358–1361, 2016.
- [84] M. Möller, A. Sayler, T. Rathje, M. Chini, Z. Chang, and G. Paulus. Precise, real-time, single-shot carrier-envelope phase measurement in the multi-cycle regime. *Applied Physics Letters*, **99**(12):121108, 2011.
- [85] Y. Zhang, P. Kellner, D. Adolph, D. Zille, P. Wustelt, D. Würzler, S. Skruszewicz, M. Möller, A. M. Sayler, and G. G. Paulus. Single-shot, real-time carrier-envelope phase measurement and tagging based on stereographic above-threshold ionization at short-wave infrared wavelengths. *Optics Letters*, **42**(24):5150–5153, 2017.
- [86] H. R. Telle, G. Steinmeyer, A. E. Dunlop, J. Stenger, D. H. Sutter, and U. Keller. Carrier-envelope offset phase control: A novel concept for absolute optical frequency measurement and ultrashort pulse generation. *Applied Physics B*, **69**(4):327–332, 1999.
- [87] D. J. Jones, S. A. Diddams, J. K. Ranka, A. Stentz, R. S. Windeler, J. L. Hall, and S. T. Cundiff. Carrier-envelope phase control of femtosecond mode-locked lasers and direct optical frequency synthesis. *Science*, **288**(5466):635–639, 2000.
- [88] A. Baltuska, M. Uiberacker, E. Goulielmakis, R. Kienberger, V. S. Yakovlev, T. Udem, T. W. Hansch, and F. Krausz. Phase-controlled amplification of few-cycle laser pulses. *IEEE Journal of Selected Topics in Quantum Electronics*, **9**(4):972–989, 2003.
- [89] Z. Chang. Carrier-envelope phase shift caused by grating-based stretchers and compressors. *Applied optics*, **45**(32):8350–8353, 2006.
- [90] C. Li, E. Moon, and Z. Chang. Carrier-envelope phase shift caused by variation of grating separation. *Optics letters*, **31**(21):3113–3115, 2006.

- [91] A. Baltuška, T. Fuji, and T. Kobayashi. Controlling the carrier-envelope phase of ultrashort light pulses with optical parametric amplifiers. *Physical review letters*, **88**(13):133901, 2002.
- [92] E. Gagnon, I. Thomann, A. Paul, A. L. Lytle, S. Backus, M. M. Murnane, H. C. Kapteyn, and A. S. Sandhu. Long-term carrier-envelope phase stability from a grating-based, chirped pulse amplifier. *Optics letters*, **31**(12):1866–1868, 2006.
- [93] S. Koke, C. Grebing, H. Frei, A. Anderson, A. Assion, and G. Steinmeyer. Direct frequency comb synthesis with arbitrary offset and shot-noise-limited phase noise. *Nature Photonics*, **4**(7):462–465, 2010.
- [94] D. Adolph, A. Sayler, T. Rathje, K. Rühle, and G. Paulus. Improved carrier-envelope phase locking of intense few-cycle laser pulses using above-threshold ionization. *Optics letters*, **36**(18):3639–3641, 2011.
- [95] G. Cerullo, A. Baltuška, O. D. Muecke, and C. Vozzi. Few-optical-cycle light pulses with passive carrier-envelope phase stabilization. *Laser & Photonics Reviews*, **5**(3):323–351, 2011.
- [96] F. Lücking, V. Crozatier, N. Forget, A. Assion, and F. Krausz. Approaching the limits of carrier-envelope phase stability in a millijoule-class amplifier. *Optics letters*, **39**(13):3884–3887, 2014.
- [97] B. Langdon, J. Garlick, X. Ren, D. J. Wilson, A. M. Summers, S. Zigo, M. F. Kling, S. Lei, C. G. Elles, E. Wells, et al. Carrier-envelope-phase stabilized terawatt class laser at 1 khz with a wavelength tunable option. *Optics express*, **23**(4):4563–4572, 2015.
- [98] D. Hoff, F. J. Furch, T. Witting, K. Rühle, D. Adolph, A. M. Sayler, M. J. Vrakking, G. G. Paulus, and C. P. Schulz. Continuous every-single-shot carrier-envelope phase measurement and control at 100 khz. *Optics letters*, **43**(16):3850–3853, 2018.
- [99] P. F. Moulton. Spectroscopic and laser characteristics of ti: Al₂O₃. *JOSA B*, **3**(1):125–133, 1986.
- [100] M. Lewenstein, P. Balcou, M. Y. Ivanov, A. L’huillier, and P. B. Corkum. Theory of high-harmonic generation by low-frequency laser fields. *Physical Review A*, **49**(3):2117, 1994.
- [101] B. Shan and Z. Chang. Dramatic extension of the high-order harmonic cutoff by using a long-wavelength driving field. *Physical Review A*, **65**(1):011804, 2001.
- [102] B. Sheehy, J. Martin, L. DiMauro, P. Agostini, K. Schafer, M. Gaarde, and K. Kulander. High harmonic generation at long wavelengths. *Physical Review Letters*, **83**(25):5270, 1999.
- [103] Z. Liu and P. B. Davies. Infrared laser absorption spectroscopy of rotational and vibration rotational transitions of heh⁺ up to the dissociation threshold. *The Journal of chemical physics*, **107**(2):337–341, 1997.
- [104] K. Liu, W. Hong, Q. Zhang, and P. Lu. Wavelength dependence of electron localization in the laser-driven dissociation of h₂⁺. *Optics express*, **19**(27):26359–26369, 2011.
- [105] K. Liu, Q. Zhang, and P. Lu. Enhancing electron localization in molecular dissociation by two-color mid-and near-infrared laser fields. *Physical Review A*, **86**(3):033410, 2012.
- [106] B. E. Schmidt, A. D. Shiner, P. Lassonde, J.-C. Kieffer, P. B. Corkum, D. M. Villeneuve, and F. Légaré. Cep stable 1.6 cycle laser pulses at 1.8 μm . *Optics express*, **19**(7):6858–6864, 2011.
- [107] Y. Deng, A. Schwarz, H. Fattahi, M. Ueffing, X. Gu, M. Ossiander, T. Metzger, V. Pervak, H. Ishizuki, T. Taira, et al. Carrier-envelope-phase-stable, 1.2 mj, 1.5 cycle laser pulses at 2.1 μm . *Optics letters*, **37**(23):4973–4975, 2012.
- [108] D. Sanchez, M. Hemmer, M. Baudisch, S. Cousin, K. Zawilski, P. Schunemann, O. Chalus, C. Simon-Boisson, and J. Biegert. 7 μm , ultrafast, sub-millijoule-level mid-infrared optical parametric chirped pulse amplifier pumped at 2 μm . *Optica*, **3**(2):147–150, 2016.
- [109] V. Shumakova, P. Malevich, S. Ališauskas, A. Voronin, A. Zheltikov, D. Faccio, D. Kartashov, A. Baltuška, and A. Pugžlys. Multi-millijoule few-cycle mid-infrared pulses through nonlinear self-compression in bulk. *Nature communications*, **7**(1):1–6, 2016.
- [110] M. A. Porras. Diffraction effects in few-cycle optical pulses. *Physical Review E*, **65**(2):026606, 2002.
- [111] M. A. Porras. Characterization of the electric field of focused pulsed gaussian beams for phase-sensitive interactions with matter. *Optics letters*, **34**(10):1546–1548, 2009.

- [112] M. A. Porras, Z. L. Horváth, and B. Major. Three-dimensional carrier-envelope-phase map of focused few-cycle pulsed gaussian beams. *Physical Review A*, **98**(6):063819, 2018.
- [113] A. Einstein. Über ein die erzeugung und verwandlung des liches betreffenden heuristischen gesichtspunkt. *Annalen der physik*, **4**, 1905.
- [114] G. N. Lewis. The conservation of photons. *Nature*, **118**(2981):874–875, 1926.
- [115] M. Göppert-Mayer. Über elementarakte mit zwei quantensprüngen. *Annalen der Physik*, **401**(3):273–294, 1931.
- [116] P. Franken, A. E. Hill, C. e. Peters, and G. Weinreich. Generation of optical harmonics. *Physical Review Letters*, **7**(4):118, 1961.
- [117] W. Kaiser and C. Garrett. Two-photon excitation in ca f 2: Eu 2+. *Physical review letters*, **7**(6):229, 1961.
- [118] A. L. Schawlow and C. H. Townes. Infrared and optical masers. *Physical Review*, **112**(6):1940, 1958.
- [119] T. H. Maiman et al. Stimulated optical radiation in ruby. 1960.
- [120] H. B. Bebb and A. Gold. Multiphoton ionization of hydrogen and rare-gas atoms. *Physical Review*, **143**(1):1, 1966.
- [121] G. Mainfray and G. Manus. Multiphoton ionization of atoms. *Reports on progress in physics*, **54**(10):1333, 1991.
- [122] V. S. Popov. Tunnel and multiphoton ionization of atoms and ions in a strong laser field (keldysh theory). *Physics-Uspekhi*, **47**(9):855, 2004.
- [123] S. L. Chin. *Multiphoton Ionization of Atoms*. Elsevier, 2012.
- [124] D. Strickland and G. Mourou. Compression of amplified chirped optical pulses. *Optics communications*, **56**(3):219–221, 1985.
- [125] V. Yanovsky, V. Chvykov, G. Kalinchenko, P. Rousseau, T. Planchon, T. Matsuoka, A. Maksimchuk, J. Nees, G. Cheriaux, G. Mourou, et al. Ultra-high intensity-300-tw laser at 0.1 hz repetition rate. *Optics Express*, **16**(3):2109–2114, 2008.
- [126] T. J. Yu, S. K. Lee, J. H. Sung, J. W. Yoon, T. M. Jeong, and J. Lee. Generation of high-contrast, 30 fs, 1.5 pw laser pulses from chirped-pulse amplification ti: sapphire laser. *Optics express*, **20**(10):10807–10815, 2012.
- [127] J. H. Sung, H. W. Lee, J. Y. Yoo, J. W. Yoon, C. W. Lee, J. M. Yang, Y. J. Son, Y. H. Jang, S. K. Lee, and C. H. Nam. 4.2 pw, 20 fs ti: sapphire laser at 0.1 hz. *Optics letters*, **42**(11):2058–2061, 2017.
- [128] G. Petite, P. Agostini, and H. Muller. Intensity dependence of non-perturbative above-threshold ionisation spectra: experimental study. *Journal of Physics B: Atomic, Molecular and Optical Physics*, **21**(24):4097, 1988.
- [129] H. Muller, A. Tip, and M. Van der Wiel. Ponderomotive force and ac stark shift in multiphoton ionisation. *Journal of Physics B: Atomic and Molecular Physics*, **16**(22):L679, 1983.
- [130] N. B. Delone and V. P. Krainov. Ac stark shift of atomic energy levels. *Physics-Uspekhi*, **42**(7):669, 1999.
- [131] T. Gallagher. Above-threshold ionization in low-frequency limit. *Physical review letters*, **61**(20):2304, 1988.
- [132] J. H. Eberly, J. Javanainen, and K. Rzażewski. Above-threshold ionization. *Physics reports*, **204**(5):331–383, 1991.
- [133] L. Keldysh et al. Ionization in the field of a strong electromagnetic wave. *Sov. Phys. JETP*, **20**(5):1307–1314, 1965.
- [134] G. Gibson, T. Luk, and C. Rhodes. Tunneling ionization in the multiphoton regime. *Physical Review A*, **41**(9):5049, 1990.

- [135] E. Mevel, P. Breger, R. Trainham, G. Petite, P. Agostini, A. Migus, J.-P. Chambaret, and A. Antonetti. Atoms in strong optical fields: evolution from multiphoton to tunnel ionization. *Physical review letters*, **70**(4):406, 1993.
- [136] A. Perelomov, V. Popov, and M. Terent'ev. Ionization of atoms in an alternating electric field. *Sov. Phys. JETP*, **23**(5):924–934, 1966.
- [137] A. Perelomov, V. Popov, and M. Terent'ev. Ionization of atoms in an alternating electric field: II. *Sov. Phys. JETP*, **24**(1):207–217, 1967.
- [138] M. Ammosov, N. Delone, V. Krainov, A. Perelomov, V. Popov, M. Terent'ev, G. L. Yudin, and M. Y. Ivanov. Tunnel ionization of complex atoms and of atomic ions in an alternating electric field. *Sov. Phys. JETP*, **64**(1191):26, 1986.
- [139] X. Tong and C. Lin. Empirical formula for static field ionization rates of atoms and molecules by lasers in the barrier-suppression regime. *Journal of Physics B: Atomic, Molecular and Optical Physics*, **38**(15):2593, 2005.
- [140] A. A. Radzig and B. M. Smirnov. *Reference data on atoms, molecules, and ions*, volume 31. Springer Science & Business Media, 2012.
- [141] T. K. Kjeldsen and L. B. Madsen. Strong-field ionization of diatomic molecules and companion atoms: Strong-field approximation and tunneling theory including nuclear motion. *Physical Review A*, **71**(2):023411, 2005.
- [142] X.-M. Tong, Z. Zhao, and C.-D. Lin. Theory of molecular tunneling ionization. *Physical Review A*, **66**(3):033402, 2002.
- [143] G. L. Yudin and M. Y. Ivanov. Nonadiabatic tunnel ionization: Looking inside a laser cycle. *Physical Review A*, **64**(1):013409, 2001.
- [144] D. Bauer and P. Mulser. Exact field ionization rates in the barrier-suppression regime from numerical time-dependent schrödinger-equation calculations. *Physical Review A*, **59**(1):569, 1999.
- [145] P. B. Corkum. Plasma perspective on strong field multiphoton ionization. *Physical review letters*, **71**(13):1994, 1993.
- [146] G. Paulus, W. Becker, and H. Walther. Classical rescattering effects in two-color above-threshold ionization. *Physical Review A*, **52**(5):4043, 1995.
- [147] W. Becker, S. Goreslavski, D. Milošević, and G. Paulus. Low-energy electron rescattering in laser-induced ionization. *Journal of Physics B: Atomic, Molecular and Optical Physics*, **47**(20):204022, 2014.
- [148] E. Hasović, M. Busuladžić, A. Gazibegović-Busuladžić, D. Milošević, and W. Becker. Simulation of above-threshold ionization experiments using the strong-field approximation. *Laser physics*, **17**(4):376–389, 2007.
- [149] G. G. Paulus, W. Becker, W. Nicklich, and H. Walther. Rescattering effects in above-threshold ionization: a classical model. *Journal of Physics B: Atomic, Molecular and Optical Physics*, **27**(21):L703, 1994.
- [150] M. Busuladžić, A. Gazibegović-Busuladžić, and D. Milošević. High-order above-threshold ionization in a laser field: Influence of the ionization potential on the high-energy cutoff. *Laser physics*, **16**(2):289–293, 2006.
- [151] D. W. Chandler and P. L. Houston. Two-dimensional imaging of state-selected photodissociation products detected by multiphoton ionization. *The Journal of chemical physics*, **87**(2):1445–1447, 1987.
- [152] A. T. Eppink and D. H. Parker. Velocity map imaging of ions and electrons using electrostatic lenses: Application in photoelectron and photofragment ion imaging of molecular oxygen. *Review of Scientific Instruments*, **68**(9):3477–3484, 1997.
- [153] S. Skruszewicz, J. Passig, A. Przystawik, N. Truong, M. Köther, J. Tiggesbäumker, and K.-H. Meiwes-Broer. A new design for imaging of fast energetic electrons. *International Journal of Mass Spectrometry*, **365**:338–342, 2014.

- [154] C. Bartels, C. Hock, J. Huwer, R. Kuhnen, J. Schwöbel, and B. Von Issendorff. Probing the angular momentum character of the valence orbitals of free sodium nanoclusters. *Science*, **323**(5919):1323–1327, 2009.
- [155] T. Suzuki, L. Wang, and H. Kohguchi. Femtosecond time-resolved photoelectron imaging on ultra-fast electronic dephasing in an isolated molecule. *The Journal of chemical physics*, **111**(11):4859–4861, 1999.
- [156] Y. Huismans, A. Rouzée, A. Gijsbertsen, J. Jungmann, A. Smolkowska, P. Logman, F. Lepine, C. Cauchy, S. Zamith, T. Marchenko, et al. Time-resolved holography with photoelectrons. *Science*, **331**(6013):61–64, 2011.
- [157] X.-B. Bian, Y. Huismans, O. Smirnova, K.-J. Yuan, M. Vrakking, and A. D. Bandrauk. Subcycle interference dynamics of time-resolved photoelectron holography with midinfrared laser pulses. *Physical Review A*, **84**(4):043420, 2011.
- [158] D. D. Hickstein, P. Ranitovic, S. Witte, X.-M. Tong, Y. Huismans, P. Arpin, X. Zhou, K. E. Keister, C. W. Hogle, B. Zhang, et al. Direct visualization of laser-driven electron multiple scattering and tunneling distance in strong-field ionization. *Physical review letters*, **109**(7):073004, 2012.
- [159] M. Meckel, D. Comtois, D. Zeidler, A. Staudte, D. Pavičić, H. Bandulet, H. Pépin, J. Kieffer, R. Dörner, D. Villeneuve, et al. Laser-induced electron tunneling and diffraction. *Science*, **320**(5882):1478–1482, 2008.
- [160] Z. Chen, A.-T. Le, T. Morishita, and C. Lin. Quantitative rescattering theory for laser-induced high-energy plateau photoelectron spectra. *Physical Review A*, **79**(3):033409, 2009.
- [161] J. Xu, C. I. Blaga, K. Zhang, Y. H. Lai, C. Lin, T. A. Miller, P. Agostini, and L. F. DiMauro. Diffraction using laser-driven broadband electron wave packets. *Nature communications*, **5**(1):1–6, 2014.
- [162] M. G. Pullen, B. Wolter, A.-T. Le, M. Baudisch, M. Hemmer, A. Senftleben, C. D. Schröter, J. Ullrich, R. Moshhammer, C.-D. Lin, et al. Imaging an aligned polyatomic molecule with laser-induced electron diffraction. *Nature Communications*, **6**(1):1–6, 2015.
- [163] A. E. Green, D. Sellin, and A. Zachor. Analytic independent-particle model for atoms. *Physical Review*, **184**(1):1, 1969.
- [164] H. Muller. Numerical simulation of high-order above-threshold-ionization enhancement in argon. *Physical Review A*, **60**(2):1341, 1999.
- [165] K. Kulander and T. Rescigno. Effective potentials for time-dependent calculations of multiphoton processes in atoms. *Computer physics communications*, **63**(1-3):523–528, 1991.
- [166] S. Popruzhenko, G. G. Paulus, and D. Bauer. Coulomb-corrected quantum trajectories in strong-field ionization. *Physical Review A*, **77**(5):053409, 2008.
- [167] M. Milošević and N. Simonović. Calculations of rates for strong-field ionization of alkali-metal atoms in the quasistatic regime. *Physical Review A*, **91**(2):023424, 2015.
- [168] Z. Chen, T. Morishita, A.-T. Le, M. Wickenhauser, X. Tong, and C. Lin. Analysis of two-dimensional photoelectron momentum spectra and the effect of the long-range coulomb potential in single ionization of atoms by intense lasers. *Physical Review A*, **74**(5):053405, 2006.
- [169] D. Ray, B. Ulrich, I. Bocharova, C. Maharjan, P. Ranitovic, B. Gramkow, M. Magrakvelidze, S. De, I. Litvinyuk, A.-T. Le, et al. Large-angle electron diffraction structure in laser-induced rescattering from rare gases. *Physical review letters*, **100**(14):143002, 2008.
- [170] D. Milošević, W. Becker, M. Okunishi, G. Prümper, K. Shimada, and K. Ueda. Strong-field electron spectra of rare-gas atoms in the rescattering regime: enhanced spectral regions and a simulation of the experiment. *Journal of Physics B: Atomic, Molecular and Optical Physics*, **43**(1):015401, 2009.
- [171] X.-M. Tong and S.-I. Chu. Density-functional theory with optimized effective potential and self-interaction correction for ground states and autoionizing resonances. *Physical Review A*, **55**(5):3406, 1997.

- [172] M. Okunishi, T. Morishita, G. Prümper, K. Shimada, C. Lin, S. Watanabe, and K. Ueda. Experimental retrieval of target structure information from laser-induced rescattered photoelectron momentum distributions. *Physical review letters*, **100**(14):143001, 2008.
- [173] S. Skruszewicz, J. Tiggesbäumker, K.-H. Meiwes-Broer, M. Arbeiter, T. Fennel, and D. Bauer. Two-color strong-field photoelectron spectroscopy and the phase of the phase. *Physical review letters*, **115**(4):043001, 2015.
- [174] M. Möller. *Probing strong-field photoionization of atoms and diatomic molecules with short-wave infrared radiation*. PhD thesis, 2017.
- [175] M. Y. Ivanov, M. Spanner, and O. Smirnova. Anatomy of strong field ionization. *Journal of Modern Optics*, **52**(2-3):165–184, 2005.
- [176] L. Arissian, C. Smeenk, F. Turner, C. Trallero, A. Sokolov, D. Villeneuve, A. Staudte, and P. Corkum. Direct test of laser tunneling with electron momentum imaging. *Physical review letters*, **105**(13):133002, 2010.
- [177] M. Möller, Y. Cheng, S. D. Khan, B. Zhao, K. Zhao, M. Chini, G. G. Paulus, and Z. Chang. Dependence of high-order-harmonic-generation yield on driving-laser ellipticity. *Physical Review A*, **86**(1):011401, 2012.
- [178] Q. Su and J. Eberly. Model atom for multiphoton physics. *Physical Review A*, **44**(9):5997, 1991.
- [179] Y. I. Salamin, S. Hu, K. Z. Hatsagortsyan, and C. H. Keitel. Relativistic high-power laser–matter interactions. *Physics Reports*, **427**(2-3):41–155, 2006.
- [180] S. Majorosi, M. G. Benedict, and A. Czirják. Improved one-dimensional model potentials for strong-field simulations. *Physical Review A*, **98**(2):023401, 2018.
- [181] H. Chomet, D. Sarkar, and C. F. de Morisson Faria. Quantum bridges in phase space: interference and nonclassicality in strong-field enhanced ionisation. *New Journal of Physics*, **21**(12):123004, 2019.
- [182] S. Majorosi, M. G. Benedict, F. Bogár, G. Paragi, and A. Czirják. Density-based one-dimensional model potentials for strong-field simulations in he, h 2+, and h 2. *Physical Review A*, **101**(2):023405, 2020.
- [183] C. Peltz, C. Varin, T. Brabec, and T. Fennel. Computational strong-field quantum dynamics, 2017.
- [184] H. Muller. An efficient propagation scheme for the time-dependent schrödinger equation in the velocity gauge. *LASER PHYSICS-LAWRENCE-*, **9**:138–148, 1999.
- [185] K. Schafer and K. Kulander. Energy analysis of time-dependent wave functions: Application to above-threshold ionization. *Physical Review A*, **42**(9):5794, 1990.
- [186] D. Bauer and P. Koval. Qprop: A schrödinger-solver for intense laser–atom interaction. *Computer physics communications*, **174**(5):396–421, 2006.
- [187] V. Mosert and D. Bauer. Photoelectron spectra with qprop and t-surff. *Computer Physics Communications*, **207**:452–463, 2016.
- [188] C. Barty, G. Korn, F. Raksi, C. Rose-Petruck, J. Squier, A.-C. Tien, K. Wilson, V. Yakovlev, and K. Yamakawa. Regenerative pulse shaping and amplification of ultrabroadband optical pulses. *Optics letters*, **21**(3):219–221, 1996.
- [189] R. Szipöcs, K. Ferencz, C. Spielmann, and F. Krausz. Chirped multilayer coatings for broadband dispersion control in femtosecond lasers. *Optics letters*, **19**(3):201–203, 1994.
- [190] V. Pervak, I. Ahmad, M. Trubetskov, A. Tikhonravov, and F. Krausz. Double-angle multilayer mirrors with smooth dispersion characteristics. *Optics express*, **17**(10):7943–7951, 2009.
- [191] M. Nisoli, S. De Silvestri, and O. Svelto. Generation of high energy 10 fs pulses by a new pulse compression technique. *Applied Physics Letters*, **68**(20):2793–2795, 1996.
- [192] V. Cardin, N. Thiré, S. Beaulieu, V. Wanie, F. Légaré, and B. E. Schmidt. 0.42 tw 2-cycle pulses at 1.8 μ m via hollow-core fiber compression. *Applied Physics Letters*, **107**(18):181101, 2015.

- [193] T. Nagy, P. Simon, and L. Veisz. High-energy few-cycle pulses: post-compression techniques. *Advances in Physics: X*, **6**(1):1845795, 2021.
- [194] C. Iaconis and I. A. Walmsley. Spectral phase interferometry for direct electric-field reconstruction of ultrashort optical pulses. *Optics letters*, **23**(10):792–794, 1998.
- [195] C. Iaconis and I. A. Walmsley. Self-referencing spectral interferometry for measuring ultrashort optical pulses. *IEEE Journal of quantum electronics*, **35**(4):501–509, 1999.
- [196] L. Gallmann, D. Sutter, N. Matuschek, G. Steinmeyer, U. Keller, C. Iaconis, and I. Walmsley. Characterization of sub-6-fs optical pulses with spectral phase interferometry for direct electric-field reconstruction. *Optics letters*, **24**(18):1314–1316, 1999.
- [197] D. J. Kane and R. Trebino. Characterization of arbitrary femtosecond pulses using frequency-resolved optical gating. *IEEE Journal of Quantum Electronics*, **29**(2):571–579, 1993.
- [198] R. Trebino and D. J. Kane. Using phase retrieval to measure the intensity and phase of ultrashort pulses: frequency-resolved optical gating. *JOSA A*, **10**(5):1101–1111, 1993.
- [199] D. J. Kane and R. Trebino. Single-shot measurement of the intensity and phase of an arbitrary ultrashort pulse by using frequency-resolved optical gating. *Optics letters*, **18**(10):823–825, 1993.
- [200] S. Kühn, M. Dumergue, S. Kahaly, S. Mondal, M. Füle, T. Csizmadia, B. Farkas, B. Major, Z. Várallyay, E. Cormier, et al. The eli-alps facility: the next generation of attosecond sources. *Journal of Physics B: Atomic, Molecular and Optical Physics*, **50**(13):132002, 2017.
- [201] N. Thiré, R. Maksimenka, B. Kiss, C. Ferchaud, P. Bizouard, E. Cormier, K. Osvay, and N. Forget. 4-w, 100-khz, few-cycle mid-infrared source with sub-100-mrad carrier-envelope phase noise. *Optics express*, **25**(2):1505–1514, 2017.
- [202] N. Thiré, R. Maksimenka, B. Kiss, C. Ferchaud, G. Gitzinger, T. Pinoteau, H. Josselin, S. Jarosch, P. Bizouard, V. Di Pietro, et al. Highly stable, 15 w, few-cycle, 65 mrad cep-noise mid-ir opcpa for statistical physics. *Optics express*, **26**(21):26907–26915, 2018.
- [203] N. Garejev, G. Tamošauskas, and A. Dubietis. Comparative study of multioctave supercontinuum generation in fused silica, yag, and lif in the range of anomalous group velocity dispersion. *JOSA B*, **34**(1):88–94, 2017.
- [204] R. Flender, M. Kurucz, T. Grosz, A. Borzsonyi, U. Gimzevskis, A. Samalius, D. Hoff, and B. Kiss. Dispersive mirror characterization and application for mid-infrared post-compression. *Journal of Optics*, **23**(6):065501, 2021.
- [205] B. Kiss, R. Flender, M. Kurucz, T. Somoskői, and E. Cormier. Non-linear materials for efficient mid-ir few cycle pulse compression. In *Laser-Induced Damage in Optical Materials 2021*, volume 11910, page 1191009. SPIE, 2021.
- [206] G. G. Paulus, F. Lindner, H. Walther, A. Baltuška, E. Goulielmakis, M. Lezius, and F. Krausz. Measurement of the phase of few-cycle laser pulses. *Physical review letters*, **91**(25):253004, 2003.
- [207] B. Wolter, M. G. Pullen, A.-T. Le, M. Baudisch, K. Doblhoff-Dier, A. Senftleben, M. Hemmer, C. D. Schröter, J. Ullrich, T. Pfeifer, et al. Ultrafast electron diffraction imaging of bond breaking in di-ionized acetylene. *Science*, **354**(6310):308–312, 2016.
- [208] P. Wustelt, F. Oppermann, L. Yue, M. Möller, T. Stöhlker, M. Lein, S. Gräfe, G. G. Paulus, and A. M. Sayler. Heteronuclear limit of strong-field ionization: Fragmentation of heh+ by intense ultrashort laser pulses. *Physical review letters*, **121**(7):073203, 2018.
- [209] P. Wustelt, F. Oppermann, S. Mhatre, M. Kübel, A. M. Sayler, M. Lein, S. Gräfe, and G. G. Paulus. Laser-driven anharmonic oscillator: Ground-state dissociation of the helium hydride molecular ion by midinfrared pulses. *Physical Review Letters*, **127**(4):043202, 2021.
- [210] J. Tate, T. Augustine, H. Muller, P. Salières, P. Agostini, and L. DiMauro. Scaling of wave-packet dynamics in an intense midinfrared field. *Physical Review Letters*, **98**(1):013901, 2007.
- [211] M. Kübel, M. Arbeiter, C. Burger, N. G. Kling, T. Pischke, R. Moshhammer, T. Fennel, M. F. Kling, and B. Bergues. Phase-and intensity-resolved measurements of above threshold ionization by few-cycle pulses. *Journal of Physics B: Atomic, Molecular and Optical Physics*, **51**(13):134007, 2018.

- [212] M. Kübel, K. Betsch, N. G. Johnson, U. Kleineberg, R. Moshhammer, J. Ullrich, G. Paulus, M. F. Kling, and B. Bergues. Carrier-envelope-phase tagging in measurements with long acquisition times. *New Journal of Physics*, **14**(9):093027, 2012.
- [213] A. Sayler, P. Wang, K. Carnes, and I. Ben-Itzhak. Determining intensity dependence of ultrashort laser processes through focus z-scanning intensity-difference spectra: application to laser-induced dissociation of H^+ . *Journal of Physics B: Atomic, Molecular and Optical Physics*, **40**(22):4367, 2007.
- [214] M. Lax, W. H. Louisell, and W. B. McKnight. From maxwell to paraxial wave optics. *Physical Review A*, **11**(4):1365, 1975.
- [215] L. G. Gouy. *Sur une propriété nouvelle des ondes lumineuses*. Gauthier-Villars, 1890.
- [216] M. Born and E. Wolf. *Principles of Optics*. Cambridge University Press, 1989.
- [217] R. W. Boyd. Intuitive explanation of the phase anomaly of focused light beams. *JOSA*, **70**(7):877–880, 1980.
- [218] S. Feng and H. G. Winful. Physical origin of the gouy phase shift. *Optics letters*, **26**(8):485–487, 2001.
- [219] A. E. Siegman. Lasers university science books. *Mill Valley, CA*, **37**(208):169, 1986.
- [220] T. Ackemann, W. Grosse-Nobis, and G. Lippi. The gouy phase shift, the average phase lag of fourier components of hermite-gaussian modes and their application to resonance conditions in optical cavities. *Optics communications*, **189**(1-3):5–14, 2001.
- [221] H. Kelkar, D. Wang, D. Martín-Cano, B. Hoffmann, S. Christiansen, S. Götzinger, and V. Sandoghdar. Sensing nanoparticles with a cantilever-based scannable optical cavity of low finesse and sub- λ 3 volume. *Physical Review Applied*, **4**(5):054010, 2015.
- [222] M. Lewenstein, P. Salieres, and A. L’huillier. Phase of the atomic polarization in high-order harmonic generation. *Physical Review A*, **52**(6):4747, 1995.
- [223] F. Lindner, W. Stremme, M. G. Schätzel, F. Grasbon, G. G. Paulus, H. Walther, R. Hartmann, and L. Strüder. High-order harmonic generation at a repetition rate of 100 khz. *Physical Review A*, **68**(1):013814, 2003.
- [224] T. Auguste, B. Carré, and P. Salières. Quasi-phase-matching of high-order harmonics using a modulated atomic density. *Physical Review A*, **76**(1):011802, 2007.
- [225] R. Ganeev, M. Suzuki, and H. Kuroda. Quasi-phase-matching of high-order harmonics in multiple plasma jets. *Physical Review A*, **89**(3):033821, 2014.
- [226] H. He and X.-C. Zhang. Analysis of gouy phase shift for optimizing terahertz air-biased-coherent-detection. *Applied Physics Letters*, **100**(6):061105, 2012.
- [227] A. Ruffin, J. Whitaker, S. Feng, H. Winful, and J. Rudd. Direct observation of the gouy phase shift with single-cycle terahertz pulses. In *Technical Digest. Summaries of papers presented at the Conference on Lasers and Electro-Optics. Postconference Edition. CLEO’99. Conference on Lasers and Electro-Optics (IEEE Cat. No. 99CH37013)*, pages 396–397. IEEE, 1999.
- [228] R. McGowan, R. Cheville, and D. Grischkowsky. Direct observation of the gouy phase shift in thz impulse ranging. *Applied Physics Letters*, **76**(6):670–672, 2000.
- [229] J. L. Johnson, T. D. Dorney, and D. M. Middleman. Enhanced depth resolution in terahertz imaging using phase-shift interferometry. *Applied Physics Letters*, **78**(6):835–837, 2001.
- [230] M. Kim, A. Naqavi, T. Scharf, K. Weible, R. Völkel, C. Rockstuhl, and H. Herzig. Experimental and theoretical study of the gouy phase anomaly of light in the focus of microlenses. *Journal of Optics*, **15**(10):105708, 2013.
- [231] F. Lindner, G. G. Paulus, H. Walther, A. Baltuška, E. Goulielmakis, M. Lezius, and F. Krausz. Gouy phase shift for few-cycle laser pulses. *Physical review letters*, **92**(11):113001, 2004.
- [232] D. Hoff, M. Krüger, L. Maisenbacher, A. Sayler, G. G. Paulus, and P. Hommelhoff. Tracing the phase of focused broadband laser pulses. *Nature Physics*, **13**(10):947–951, 2017.

- [233] M. A. Porrás. Ultrashort pulsed gaussian light beams. *Physical Review E*, **58**(1):1086, 1998.
- [234] M. A. Porrás. Pulse correction to monochromatic light-beam propagation. *Optics letters*, **26**(1):44–46, 2001.
- [235] R. Peng and D. Fan. Comparison between complex amplitude envelope representation and complex analytic signal representation in studying pulsed gaussian beam. *Optics communications*, **246**(4-6):241–248, 2005.
- [236] M. A. Porrás and P. Dombi. Freezing the carrier-envelope phase of few-cycle light pulses about a focus. *Optics express*, **17**(22):19424–19434, 2009.
- [237] Z. Horváth, J. Vinkó, Z. Bor, and D. Von der Linde. Acceleration of femtosecond pulses to superluminal velocities by gouy phase shift. *Applied Physics B*, **63**(5):481–484, 1996.
- [238] A. Kaplan. Diffraction-induced transformation of near-cycle and subcycle pulses. *JOSA B*, **15**(3):951–956, 1998.
- [239] T. Tritschler, K. Hof, M. Klein, and M. Wegener. Variation of the carrier-envelope phase of few-cycle laser pulses owing to the gouy phase: a solid-state-based measurement. *Optics letters*, **30**(7):753–755, 2005.
- [240] Q. Lin, J. Zheng, and W. Becker. Subcycle pulsed focused vector beams. *Physical review letters*, **97**(25):253902, 2006.
- [241] M. A. Porrás, B. Major, and Z. L. Horvath. Carrier-envelope phase shift of few-cycle pulses along the focus of lenses and mirrors beyond the nonreshaping pulse approximation: the effect of pulse chirp. *JOSA B*, **29**(12):3271–3276, 2012.
- [242] D. Hoff, M. Krüger, L. Maisenbacher, G. G. Paulus, P. Hommelhoff, and A. Sayler. Using the focal phase to control attosecond processes. *Journal of Optics*, **19**(12):124007, 2017.
- [243] G. Jolicard and O. Atabek. Above-threshold-dissociation dynamics of h 2+ with short intense laser pulses. *Physical Review A*, **46**(9):5845, 1992.
- [244] G. Agarwal. Field-correlation effects in multiphoton absorption processes. *Physical Review A*, **1**(5):1445, 1970.
- [245] D. Zille. *Scaling Ultrashort Light-Matter-Interaction to the Short-Wave Infrared Regime and Beyond*. PhD thesis, Friedrich-Schiller-Universität Jena, 2018.
- [246] A. Baltuška, T. Udem, M. Uiberacker, M. Hentschel, E. Goulielmakis, C. Gohle, R. Holzwarth, V. S. Yakovlev, A. Scrinzi, T. W. Hänsch, et al. Attosecond control of electronic processes by intense light fields. *Nature*, **421**(6923):611–615, 2003.
- [247] R. Hollinger, D. Hoff, P. Wustelt, S. Skruszewicz, Y. Zhang, H. Kang, D. Würzler, T. Jungnickel, M. Dumergue, A. Nayak, et al. Carrier-envelope-phase measurement of few-cycle mid-infrared laser pulses using high harmonic generation in zno. *Optics Express*, **28**(5):7314–7322, 2020.
- [248] X. Xie, K. Doblhoff-Dier, S. Roither, M. S. Schöffler, D. Kartashov, H. Xu, T. Rathje, G. G. Paulus, A. Baltuška, S. Gräfe, et al. Attosecond-recollision-controlled selective fragmentation of polyatomic molecules. *Physical review letters*, **109**(24):243001, 2012.
- [249] M. Kübel, P. Wustelt, Y. Zhang, S. Skruszewicz, D. Hoff, D. Würzler, H. Kang, D. Zille, D. Adolph, G. Paulus, et al. High-order phase-dependent asymmetry in the above-threshold ionization plateau. *Physical Review Letters*, **126**(11):113201, 2021.
- [250] D. B. Milošević. Vii strong-field approximation and quantum orbits. *Computational Strong-Field Quantum Dynamics: Intense Light-Matter Interactions*, page 203, 2017.
- [251] J. Eberly. Scale variation in a one-dimensional model of an atom interacting with a strong laser field. *Physical Review A*, **42**(9):5750, 1990.

Publications

1. **Y. Zhang**, D. Zille, D. Hoff, P. Wustelt, D. Würzler, M. Möller, A. M. Sayler, G. G. Paulus. Observing the importance of the phase-volume effect for few-cycle light-matter interactions. *Physical Review Letters*, **124**(13):p133202, 2020
2. **Y. Zhang**, P. Kellner, D. Adolph, D. Zille, P. Wustelt, D. Würzler, S. Skruszewicz, M. Möller, A. M. Sayler, G. G. Paulus. Single-shot, real-time carrier-envelope phase measurement and tagging based on stereographic above-threshold ionization at short-wave infrared wavelengths. *Optics Letters*, **42**(24):p5150, 2017
3. M. Kübel, P. Wustelt, **Y. Zhang**, S. Skruszewicz, D. Hoff, D. Würzler, H. Kang, D. Zille, D. Adolph, G. G. Paulus, A. M. Sayler, M. Dumergue, A. Nayak, R. Flender, L. Haizer, M. Kurucz, B. Kiss, S. Kühn, B. Fetić and D. B. Milošević. High-order phase-dependent asymmetry in the above-threshold ionization plateau. *Physical Review Letters*, **126**(11):p113201, 2021
4. L. Stoyanov, **Y. Zhang**, A. Dreischuh and G. G. Paulus. Long-range quasi-non-diffracting Gauss-Bessel beams in a few-cycle laser field. *Optics Express*, **29**(7):10997, 2021
5. N. Dimitrov, M. Zhekova, **Y. Zhang**, G. G. Paulus and A. Dreischuh. Background-free femtosecond autocorrelation in collinearly-aligned inverted field geometry using optical vortices. *Optics Communications*, **504**:p127493, 2021
6. R. Hollinger, D. Hoff, P. Wustelt, S. Skruszewicz, **Y. Zhang**, H. Kang, D. Würzler, T. Jungnickel, M. Dumergue, A. Nayak, R. Flender, L. Haizer, M. Kurucz, B. Kiss, S. Kühn, Eric Cormier, C. Spielmann, G. G. Paulus, P. Tzallas and M. Kübel. Carrier-envelope-phase measurement of few-cycle mid-infrared laser pulses using high harmonic generation in ZnO. *Optics Express*, **28**(5):p7313, 2020
7. D. Würzler, S. Skruszewicz, A. M. Sayler, D. Zille, M. Möller, P. Wustelt, **Y. Zhang**, J. Tiggesbäumker, G. G. Paulus. Accurate retrieval of ionization times by means of the phase-of-the-phase spectroscopy, and its limits. *Physical Review A*, **101**(3):p033416, 2020

Acknowledgement

I would like to thank everyone who helped me from all aspects in the past few years.

Firstly, I would like to express my warmest gratitude to my primary supervisor, Prof. Gerhard G. Paulus who guided me in academy and supported me in life throughout my whole master and doctoral periods. Under his guidance, I had many opportunities to work on different research topics, e.g., pulse compressions, coherent combination of few-cycle pulses, CEP-dependent light-matter interactions, imaging of plasma waves, generating Bessel beams and birefringent effect in vacuum. He imparted me countless knowledge and taught me many skills, e.g., how to write a high-quality scientific article, how to make an impressive presentation and communication skills. He motivated me when I was down or making mistakes. He is a very supportive supervisor and provides me large extent of freedom in both academy and life. I feel lucky that I can meet such a wonderful supervisor.

I would like to thank Dr. Philipp Wustelt, an excellent supervisor, a superb colleague to work with and a good friend. Since I joined the Nonlinear group in the second semester of my master period, we had worked together over 7 years. I learned plenty of knowledge and skills from him. I admire his way of working and his attitude about life. With his great support, I feel not alone and my life in Germany becomes much easier.

Dr. Max Möller, another top supervisor, colleague and friend. He was my tutor of nonlinear optics lecture. He was one of the main reason that I joined the group. I am impressed by his talent and his personality. He provided me many support in researches. I enjoyed working with him. He brought me into the field of strong-field physics from the initial topic about laser technologies, which led to the begin of the story of this thesis.

Dr. Matthias Kübel, an outstanding scientist, joined our group later in my PhD period and became a very important person to me. With his broad knowledge, great passion, and perfect organisations, my researches had big progress and he helped me draw a great ending of my PhD career.

I would like to thank Prof. A. Max Sayler who gave me tremendous support in physics theory, simulations and English. He is a talented scientist and an amazing writer. I am very impressed by his capabilities both in science and language. I wish someday I can write a scientific article as good as him even if in Chinese.

I would like to thank Dr. Dominik Hoff for his discussions about the focal phase and his great supports on the previous experimental results. I also would like to acknowledge Dr. Danilo Zille for his discussions and supports on the simulation works. Their supports and efforts are important to this thesis.

Thomas Weber is our omnipotent technician! With him, we never need to worry about the laser systems and the mechanics. If you have an idea, he makes it feasible. If you don't have a clue, he provides smart designs. His great support make our experiments much easier.

I would like to thank my colleagues, Dr. Daniel Würzler, Daniel Adolph, Falk Ron-

neberger, Dr. Slawomir Skruszewicz, Philipp Kellner and people from the XCT branch: Dr. Silvio Fuchs, Dr. Martin Wünsche, Julius Reinhard, Johann Jakob Abel and Felix Wiesner and all other members in the NLO group. It is my great pleasure to work with them.

I would like to acknowledge Prof. Malte C. Kaluza about the project of imaging of low electron density plasma waves and I would like to thank Dr. Alexander Sävert and Carola Zepter for their supports and valuable discussions on this project.

I also want to thank Prof. Alexander Dreischuh, Dr. Lyubomir Stoyanov, and Nikolay Dimitrov for the project of generation and applications of Gaussian-Bessel beams. I learned a lot from them in this area. It is my honour to work with them.

At last, I would like to thank my beloved wife, Shiqi Jiang, also with an upcoming doctoral degree in physics. Her help to me is all-around, in life, in academy and in spirit. She is a wisdom person and she helps me upgrade my perspectives to people and the world. She makes me a better man. She is my life mentor. Having a PhD together with her in Germany is an extremely precious experience to me. I appreciate every bit of happiness she brings to me. In addition, I would like to thank my parents, Dr. Jinming Zhang and Assoc. Prof. Kang Shao. Without their love and support regardless of any cost, it would be impossible to become today's me.

Ehrenwörtliche Erklärung

Ich erkläre hiermit ehrenwörtlich, dass ich die vorliegende Arbeit selbständig, ohne unzulässige Hilfe Dritter und ohne Benutzung andere als der angegebenen Hilfsmittel und Literatur angefertigt habe. Die aus anderen Quellen direkt oder indirekt übernommenen Daten und Konzepte sind unter Angabe der Quelle gekennzeichnet.

Die in dieser Arbeit beschriebene Forschungsarbeit und Auswahl der Schwerpunkte fand in enger Zusammenarbeit mit meinem betreuenden Hochschullehrer Prof. Dr. Gerhard. G. Paulus statt.

Bei der Auswahl und Auswertung folgenden Materials haben mir die nachstehend aufgeführten Personen in der jeweils beschriebenen Weise unentgeltlich geholfen:

1. Dr. Danilo Zille stellte numerische berechnete differenzielle Wirkungsquerschnitte von Xenon zur Verfügung, die in den semiklassischen Simulationen in Kapitel 5 dieser Arbeit verwendet wurden.

2. Dr. Domink Hoff stellte die experimentellen Daten der CEP-Messung bei 800 nm in Kapitel 6.

Weitere Personen waren an der inhaltlich-materiellen Erstellung der vorliegenden Arbeit nicht beteiligt. Insbesondere habe ich hierfür nicht die entgeltliche Hilfe von Vermittlungs- bzw. Beratungsdiensten (Promotionsberater oder andere Personen) in Anspruch genommen. Niemand hat von mir unmittelbar oder mittelbar geldwerte Leistungen für Arbeiten erhalten, die im Zusammenhang mit dem Inhalt der vorgelegten Dissertation stehen.

Die Arbeit wurde bisher weder im In- noch im Ausland in gleicher oder ähnlicher Form einer anderen Prüfungsbehörde vorgelegt.

Die geltende Promotionsordnung der Physikalisch-Astronomischen Fakultät ist mir bekannt.

Ich versichere ehrenwörtlich, dass ich nach bestem Wissen und Gewissen die reine Wahrheit gesagt und nichts verschwiegen habe.